



UNIVERSIDAD DE SEVILLA
DEPARTAMENTO DE FÍSICA APLICADA I

^{41}Ca measurement with Low Energy Accelerator Mass Spectrometry (LEAMS) at the Centro Nacional de Aceleradores

A thesis submitted for the degree of
DOCTOR IN PHYSICAL SCIENCES AND TECHNOLOGIES

PRESENTED BY
CARLOS VIVO VILCHES

SUPERVISORS
Dr. José María López Gutiérrez
Dr. Christof Vockenhuber

2018

José María López Gutiérrez, Profesor Titular del Departamento de Física Aplicada I de la Universidad de Sevilla;

y

Christof Vockenhuber, Científico Titular del Laboratorio de Física de Haces de Iones de la Escuela Politécnica Federal de Zúrich

CERTIFICAN: Que la presente memoria “⁴¹Ca measurement with Low Energy Accelerator Mass Spectrometry (LEAMS) at the Centro Nacional de Aceleradores” ha sido realiza bajo su dirección conjunta en el Centro Nacional de Aceleradores por **Carlos Vivo Vilches** para optar al grado de Doctor en Ciencias y Tecnologías Físicas.

Para que así conste, y en cumplimiento con la legislación vigente, firman el presente documento.

Sevilla, a X de junio de 2018

José María López Gutiérrez

Christof Vockenhuber

A mi familia, con todo mi amor

In this age of specialization men who thoroughly know one field are often incompetent to discuss another. The great problems of the relations between one and another aspect of human activity have for this reason been discussed less and less in public. When we look at the past great debates on these subjects we feel jealous of those times, for we should have liked the excitement of such argument. The old problems, such as the relation of science and religion, are still with us, and I believe present as difficult dilemmas as ever, but they are not often publicly discussed because of the limitations of specialization.

Richard Feynman

Agradecimientos

Danksagung

Ringraziamenti

¿Qué queda por decir, además de *alea iacta est*? Pues falta agradecer a toda la gente que me ha acompañado durante este doctorado, que no es poca. Voy a intentar ir *dejando* los distintos agradecimientos en el orden más estándar, ya que en esto de los agradecimientos de tesis ya hay cierta jurisprudencia. Über diese Teile dass ich auf Deutsch schreibe, muss ich sache entschuldigung, weil ich mein Deutsch vergessen habe, und vielleicht etwas is nicht völlig richtig. Aunque en el título también añadido la palabra *ringraziamenti*, no me atreveré a escribir más cosas en italiano que algún *grazie* suelto. Suficiente italiano inventado han soportado los destinatarios durante estos años.

Y como sigo un orden estándar, empezaré estos agradecimientos por mis directores. Agradecer a José María su constante supervisión, su disponibilidad y su buen rollo. Si alguien se merece el reconocimiento principal por la dirección de esta tesis y decir el día de mañana "a ese chico le dirigí yo la tesis", es sin duda él. Ich muss also mein co-Betreuer, Christof, danken. Obwohl er noch nicht mein Betreuer während meines 4-Monate Besuch nach ETH Zurich war, hat er wie mein Betreuer mit mir benommen. Seine Erfahrung in ^{41}Ca AMS und in der berichtigen der Kaliuminterferenz waren notwendig für die Messunge in Seville. Y debo también dar las gracias a Manolo, quien me dio esta oportunidad y ha estado siempre atento a todos los problemas burocráticos a pesar de estar siempre hasta arriba de trabajo. Que alguien con tanto *jaleo* esté siempre que puede disponible es muy de agradecer, y es una pena que al final no conste como mi director.

También tengo que agradecer al resto del grupo de AMS del CNA, porque creo que es difícil encontrar un grupo con el mismo buen rollo, e imposible con mejor: a Javi, por sus tardes de juegos y su sentido del humor; a Elena, porque su inigualable conocimiento de SARA ha sido una ayuda constante, amable y a menudo requerida durante estos cuatro años; a Juan

Ignacio, que me ayudó enormemente en mis primeros *pinitos* en el mundo de la Química; a Juan, por cuidar de SARA y aclararme miles de aspectos técnicos; a Grazia, a la que espero que las tierras flamencas la estén tratando bien; y a Mercedes, que más que compañera de trabajo o amiga, ya la considero como una hermana pequeña; también a Victoria, que desde que entró al laboratorio se ha vuelto indispensable; y, aunque no haya trabajado con ellas, a Isa, Lidia y Aurora, por tantos momentos juntos en comidas y cenas.

Ich mochte also die Leute aus der ETH Gruppe für Ionentrahlphysik danken. Während meines Besuch, habe ich als ein anderer Mitarbeiter gefeilt. Vielen Dank, Arno, für das Tor der Gruppe öffnen; Marcus, Noldi, und Sascha, für ihre Hilfe mit TANDY wann Christof nicht helfen konnte; Rudi, für mein Computer vorbereiten; Anita, für ihre Freude und deine Hilfe mit die Presse; andere Studenten der Gruppe, als Chrissie, Laura, Adam, Daniele, Olivia, Klaus-Ulrich..., für das bestes Klima in ETH und aus; thanks a lot to the visitors from other parts at the group (Stefano, Lina, Giulia...), for adding more international mood to my stay; muchas gracias a María por su simpatía, por aportar el ingrediente latino; moltes gràcies a la Núria, por transmitir su energía y por estar pendiente de mí los primeros días; y finalmente, eskerrik asko a Maxi, que sin duda aportó grandes dosis de humor durante esos meses, y por ser paciente enseñándonos a Chrissie y a mí a escalar. Entschuldigung wenn ich jemand vergesse: gab es viele Leute!

Gracias a Ana Calleja por las medidas de ICP-MS, y a Inés Ortega por las medidas de PIXE, especialmente por interesarse ambas por que conociese lo que hay detrás de los resultados. También quería reconocer el trabajo del personal de ENRESA, especialmente de José Luis Leganés, que siempre me ha facilitado la información necesaria para optimizar las medidas de los hormigones de José Cabrera. Ich muss also Thomas Walczyk danken, für zulassen, dass ich die Proben für die Vergleichexperiment benutzen.

Debo todo mi cariño a todos mis amigos aquí en Sevilla, muchos de ellos compañeros del CNA, con los que he pasado gran tiempo de estos 4 años por Alameda, la Feria, de tapas, de barbacoa en la Rinconada, por Córdoba... y ese gran fin de semana comiendo gorrino como susodichos en la casa rural de Aracena: primero, a todos los que ya conocía del máster¹, Joaquín, Marius, Migue, Yorch, Mercedes (aunque ya la haya mencionado) y, ya que cuenta también como del máster, mi tocayo Charles Silver, tanto por los buenos momentos durante esas semanas all around Spain como por estos años en Zebiya; al reggimento de italianos (y galos cisalpinos) que están, o han pasado, por el CNA y por la Facultad: Grazia, también ya mencionada, Cristina, Laura, Stefano, Anna (bueno, 50% italiana, 50% manchega) y Alessandro, he de decirles *grazie molte, mongolfiere fino alla victoria* y dejarles claro que la car-

¹Me refiero aquí, por supuesto, al Máster Interuniversitario en Física Nuclear, o "Nucleares por España". En ningún momento me refiero al Máster en Derecho Autonómico de la Universidad Rey Juan Carlos.

bonara buena lleva nata; a Elena y Leti, aunque se las vea sólo de vez en cuando; a las maestras, tanto de profesión como de la juerga, Alba y Manoli, porque las amistades que han unido los bares, que nos las separe ni Dios, ni el hombre; al ingeniero Andrés (también conocido como *Luigi*) y al biólogo Jose, porque a las ciencias menores y las ingenierías hay que quererlas igual; y a las jóvenes promesas del mongolfierismo sevillano, Damián, Tere y Llanlle, que espero que cuiden bien de nuestro legado cuando vayamos dejando la ciudad.

También tendrán siempre un hueco en mi memoria los otros compañeros de despacho que he tenido en el CNA: Lucía, Gema, todos los Migueles, Diana y, especialmente, a Mauri por las tertulias geopolíticas del desayuno. Ya sé que este párrafo se queda algo corto, pero muchos otros que cabrían en él ya han sido nombrados.

Debo también dar gracias a los dioses por no haberme alejado todavía demasiado de mis grandes amigos de la Facultad, la mayoría ahora en la capital del Reino: Ana, Rafa, Teleco, Portillo, Trino y , sobre todo, a Jonathan, que siempre ha tenido una cama lista para mí. Cámbiese Pedro Antonio por Malasaña o por Argüelles, la Facultad por la empresa que sea, institutos, u hospitales... ya estéis en Madrid, Bilbao o Alicante, si cuando recuerdo Granada se ilumina mi alma, es porque vosotros estáis en esos recuerdos. Infinitas gracias por seguir ahí, y por seguir expandiendo el Buenrollismo por el mundo.

Y como el orden estándar requiere, el último párrafo se debe dedicar a las personas más importantes de tu vida: a la familia. Se lo dedico a mi hermano Jose, porque todo es más fácil yendo toda mi vida a tu rebufa, y porque este período en Sevilla ha sido el período más largo que no hemos vivido bajo el mismo techo, y uno no termina de acostumbrarse (excepto a llegar a casa y que no huela a tabaco). Se lo dedico también a mi cuñada, Rocío, por tu simpatía, tu buen humor, y porque nuestras dos familias han casado a la perfección, como piezas diseñadas para ello. Y, por supuesto, he de dedicar ya no estas palabras, sino toda esta tesis y cualquier logro de mi vida, a mis padres, pues dichos logros son todos 100% vuestros. Ya que no me disteis sólo la vida, sino mis principios, mis ganas de esforzarme, si el día de mañana seré doctor, es por vosotros; y lo que es más importante, si a día de hoy me puedo considerar una buena persona, se debe todo a vosotros. Os quiero un huevo.

Contents

Agradecimientos / Danksagung / Ringraziamenti	I
List of Figures	IX
List of Tables	XIII
Acronyms	XV
Abstract	XVII
Resumen	XIX
1 Introduction	1
1.1 ^{41}Ca basic data and general applications	1
1.2 Accelerator Mass Spectrometry (AMS): finding a needle in a haystack	4
1.2.1 ^{41}Ca AMS	6
1.3 AMS at low energies	8
1.4 Motivation and outline	9
2 Comparative description of the experimental systems	13
2.1 General overview of the systems	13
2.1.1 The 1 MV AMS system at CNA Seville: SARA	14
2.1.2 The 600 kV AMS system at ETH Zurich: TANDY	15

2.2	Cs sputtering ion sources	16
2.2.1	The SO-110B ion source at SARA	17
2.2.2	The modified MC-SNICS ion source at TANDY	18
2.3	Tandem accelerators	20
2.3.1	The 1 MV tandetron at SARA	24
2.3.2	The 600 kV pelletron at TANDY	26
2.4	Electromagnetic kinematic filters	27
2.4.1	The optical properties of the HE side at SARA	33
2.4.2	The optical properties of the HE side at TANDY	34
2.5	Gas ionization chambers	35
2.5.1	The compact gas ionization chamber at SARA	38
2.5.2	The retractable gas ionization chamber at TANDY	39
3	⁴¹Ca AMS at low energies	41
3.1	The ⁴¹ K interference	41
3.2	Studies of the sources of the ⁴¹ K interference	45
3.3	Time evolution of the ⁴¹ K interference	48
3.4	Data analysis for ⁴¹ Ca AMS at TANDY and SARA	51
3.4.1	AMS measurement	52
3.4.2	Calculation of the experimental ⁴¹ K/ ³⁹ K ratio (K-correction factor)	54
3.4.3	Application of the K-correction and sample average	54
3.4.4	Blank and standard correction	56
3.4.5	Common selection criteria used at SARA and TANDY	57
4	Setup of the 1 MV AMS system at CNA for ⁴¹Ca measurements	61
4.1	Optimization of the ion source extraction	62
4.2	He stripper performance	64
4.2.1	2+ state	64

4.2.2	3+ state	66
4.2.3	Charge state distribution	67
4.3	^{40}Ca current measurement with the FC3 and ^{41}Ca detection with the compact GIC	68
4.4	K-correction and ^{41}Ca background	72
4.4.1	Tests with blank urine samples: radiochemical method	74
4.5	Measurement of the HE side optical transmission with standard samples . . .	77
4.6	Comparison measurements with TANDY	78
4.6.1	Performance parameters	78
4.6.2	Measurement of ETH in-house standards	78
4.6.3	Intercomparison with biomedical samples	79
5	^{41}Ca measurement in concrete samples from the bioshield of a nuclear power plant	89
5.1	Production of ^{41}Ca in the concrete bioshield of nuclear reactors	89
5.2	Radiochemical treatment of concrete samples for ^{41}Ca AMS measurements . .	92
5.3	Measurements of ^{41}Ca in the bioshield of the José Cabrera Nuclear Power Plant	95
5.3.1	The José Cabrera Power Plant: description of the samples	95
5.3.2	Depth profiles	98
5.3.3	Results from the lateral samples	101
6	Summary and conclusions	103
A	GICOSY files	107
A.1	SARA HE spectrometer	107
A.2	TANDY HE spectrometer	109
B	Unfeasibility of matrices different from CaH_2 for the production of $(\text{CaH}_3)^-$ ions	111
B.1	Alternatives to calcium hydride in the bibliography	111

B.2	The experiment at SARA	112
C	FORTRAN programs for ⁴¹Ca measurement analysis	115
C.1	Input file	115
C.2	Output files	117
C.2.1	out-K-correction	117
C.2.2	out-runs	118
C.2.3	out-blank	118
C.2.4	out-stds	118
C.2.5	out-final-ratios	119
	Bibliography	121
	Curriculum Vitae	137

List of Figures

1.1	Basic scheme of the stripping process.	5
1.2	Basic scheme of an AMS system.	5
1.3	Layout of several AMS facilities.	8
2.1	Picture and schematic view of the 1 MV AMS system at CNA Seville.	14
2.2	Picture and schematic view of the 600 kV AMS system at ETH.	15
2.3	Scheme of a high-current sputtering ion source.	16
2.4	Simulation of ions passing through an Einzel lens on SIMION®.	17
2.5	Piston taking a target out of the SARA sample <i>carousel</i>	18
2.6	SIMION® simulation of the SO-110B ion source.	18
2.7	Target wheel used by the MC-SNICS ion source.	19
2.8	SIMION® simulation of the ion source from TANDY.	19
2.9	Basic operation principle of the systems used by the 2 different types of particle accelerator to get the high terminal voltage.	22
2.10	Mean charge state of uranium ions as a function of the ion energy for different stripper materials.	24
2.12	SIMION® view of an electrostatic quadrupole.	26
2.13	Pellet chain used to transport the charge in the pelletron from TANDY.	27
2.14	Focusing in the X axis of magnetic dipoles depending on the inclination of the borders.	29

2.15 Focusing in the Y axis of magnetic dipoles depending on the inclination of the borders.	30
2.16 Scheme of an ESA with spherical geometry.	31
2.17 Behaviour of different ions with the same mass but different energy in an achromatic system.	32
2.18 GICOSY simulation of $^{41}\text{Ca}^{2+}$ ions in the HE side of SARA.	33
2.19 Faraday cups used in AMS measurements with SARA.	34
2.20 GICOSY simulation of $^{41}\text{Ca}^{2+}$ ions in the HE side of TANDY.	34
2.21 Scheme of the operation principle of a GIC.	35
2.22 Stopping power of ^{41}Ca and ^{41}K ions with an energy of 26.5 MeV in butane according to SRIM.	36
2.23 Detector signals in a ^{41}Ca measurement with the 5 MV AMS system at SUERC, Glasgow.	37
2.24 Scheme of the compact GIC at SARA.	38
2.25 Comparison between the old HVE GIC, and the new compact GIC.	38
2.26 Picture and scheme of the retractable GIC used in the ^{41}Ca measurements with TANDY.	39
3.1 SRIM simulation of the trajectories of several ^{41}Ca ions at two different energies in a GIC detector.	42
3.2 Spectra simulation with SRIM of an equal number of counts of ^{41}Ca and ^{41}K at different energies.	42
3.3 Evolution of $^{39}\text{K}/^{40}\text{Ca}$ ratios from blank and standard samples in target holders from different materials.	47
3.4 Time evolution of the $^{40}\text{Ca}^{2+}$ current, the $^{41}\text{M}^{2+}$ and $^{39}\text{K}^{2+}$ rates, and the $^{39}\text{K}/^{40}\text{Ca}$, $^{41}\text{M}/^{40}\text{Ca}$ and $^{41}\text{M}/^{39}\text{K}$ ratios for a blank sample (blank 1) during a measurement at SARA.	49
3.5 Time evolution of the $^{40}\text{Ca}^{2+}$ current, the $^{41}\text{M}^{2+}$ and $^{39}\text{K}^{2+}$ rates, and the $^{39}\text{K}/^{40}\text{Ca}$, $^{41}\text{M}/^{40}\text{Ca}$ and $^{41}\text{M}/^{39}\text{K}$ ratios for another blank sample (blank 2) during a measurement at SARA.	50

3.6	Typical scheme of a ^{41}Ca measurement with a compact AMS system implementing the K-correction.	53
4.1	$(^{40}\text{CaF}_3)^-$ current output from the SO-110B ion source at SARA for different blank targets mixed with silver or niobium at different weight ratios.	63
4.2	$(^{40}\text{CaF}_3)^-$ current from 2 different blank samples over a long time range.	64
4.3	$^{40}\text{Ca}^{2+}$ transmission and $^{41}\text{M}/^{40}\text{Ca}$ background as functions of the He stripper pressure at SARA.	65
4.4	$^{40}\text{Ca}^{3+}$ transmission as a function of the He stripper pressure at SARA.	67
4.5	Charge state distribution for the $(^{40}\text{CaF}_3)^- \rightarrow ^{40}\text{Ca}^q$ stripping process in He at 225 keV and 400 keV.	68
4.6	Relative position of the FC3 depending on the isotope whose current is measured and the radionuclide which is tuned to cross to the ESA.	69
4.7	Experimental and simulated spectra for $^{41}\text{Ca}^{2+}$ ions reaching the compact GIC at SARA.	70
4.8	Experimental spectra for $^{41}\text{Ca}^{3+}$ and $^{39}\text{K}^{3+}$ ions reaching the compact GIC at SARA.	71
4.9	Relationship between the ^{41}M rate reaching the compact GIC and the detector efficiency.	72
4.10	Linear correlation between the $^{41}\text{M}/^{40}\text{Ca}$ and $^{39}\text{K}/^{40}\text{Ca}$ ratios in blank samples at SARA.	73
4.11	Scheme of the calcium isolation method for urine samples.	75
4.12	Comparison of the $^{41}\text{Ca}/^{40}\text{Ca}$ ratios from the biomedical samples at TANDY and SARA.	81
4.13	Temporal evolution of the urinary $^{41}\text{Ca}/^{40}\text{Ca}$ ratio in subject 4, including measurements at TANDY and SARA.	82
4.14	Temporal evolution of the urinary $^{41}\text{Ca}/^{40}\text{Ca}$ ratio in subject 5, including measurements at TANDY and SARA.	83
4.15	Temporal evolution of the urinary $^{41}\text{Ca}/^{40}\text{Ca}$ ratio in subject 6, including measurements at TANDY and SARA.	84

4.16	Temporal evolution of the urinary $^{41}\text{Ca}/^{40}\text{Ca}$ ratio in subject 7, including measurements at TANDY and SARA.	85
4.17	Temporal evolution of the urinary $^{41}\text{Ca}/^{40}\text{Ca}$ ratio in subject 8, including measurements at TANDY and SARA.	86
4.18	Temporal evolution of the urinary $^{41}\text{Ca}/^{40}\text{Ca}$ ratio in subject 9, including measurements at TANDY and SARA.	87
4.19	Temporal evolution of the urinary $^{41}\text{Ca}/^{40}\text{Ca}$ ratio in subject 10, including measurements at TANDY and SARA.	88
5.1	^{40}Ca neutron capture cross section and thermal neutron energy distribution.	90
5.2	Scheme of the calcium isolation process for concrete samples.	93
5.3	Effect of the acid digestion of concrete sample depending on the presence of aggregates.	94
5.4	Scheme of the segmentation of the bioshield of José Cabrera and 3D picture of the shape from each block.	96
5.5	Schematic view of the position of the drill cores.	97
5.6	Position of the samples taken by scrapping the lateral surface of the sub-blocks.	98
5.7	$^{41}\text{Ca}/^{40}\text{Ca}$ results from the drill core samples and correspondence with thermal neutron fluence.	99
5.8	Cross section of the José Cabrera reactor vessel and bioshield when the plant was operative at the height of maximum neutron fluence.	100
5.9	$^{41}\text{Ca}/^{40}\text{Ca}$ results from the lateral samples.	102

List of Tables

1.1	Common radionuclides measured by AMS.	6
1.2	^{41}Ca performance parameters from different AMS facilities.	7
3.1	Energy loss straggling and average energy difference with ^{41}K ions of 3.4 MeV ^{41}Ca ions after a silicon nitride window as a function of the foil thickness.	43
3.2	Rates from different ions in an aluminum dummy and a blank sample during the experiment with the 600 kV AMS system at ETH.	46
4.1	Voltages at the accelerator terminal and the ESA in order to select different ions with the HE spectrometer at SARA.	73
4.2	Blank corrected $^{41}\text{Ca}/^{40}\text{Ca}$ ratios of the standard samples used in one of the ^{41}Ca measurements at SARA using the 2+ state.	77
4.3	Comparison of the ^{41}Ca performance parameters at SARA and TANDY.	78
4.4	Measurement of the ETH in-house ^{41}Ca standards B10 and B8 at SARA.	79

Acronyms

AMS Accelerator Mass Spectrometry

CNA Centro Nacional de Aceleradores

ESA Electrostatic Analyzer

ETH LIP ETH Laboratory of Ion Beam Physics

FC Faraday Cup

GIC Gas Ionization Chamber

HE High Energy

HEM High Energy Side Magnet

HVE High Voltage Engineering Europa B.V.

LE Low Energy

LEM Low Energy Side Magnet

LSC Liquid Scintillation Counting

NEC National Electrostatics Corp.

NPP Nuclear Power Plant

NUS National University of Singapore

PWR Pressurized Water Reactor

Abstract

The accelerator mass spectrometry (AMS) technique, developed 40 years ago for ^{14}C dating, was soon used to measure other long-lived radionuclides. One of the radionuclides measured by AMS since these early years is ^{41}Ca and for a variety of applications. Some of these applications are: the calculation of the terrestrial age of meteorites, the study of nuclear reactions of astrophysical interest, the understanding of the calcium metabolism, and the characterization of low-level nuclear waste.

The main challenge in ^{41}Ca AMS is dealing with the interference caused by its stable isobar, ^{41}K . This interference is reduced by using calcium fluoride (CaF_2) samples and the extraction of the $(\text{CaF}_3)^-$ ion. At large AMS facilities, besides, ^{41}K ions can be discriminated from ^{41}Ca ions using different detection techniques based on the energy loss dependence on the atomic number. The ^{41}Ca measurement with low energy AMS systems, like the 1 MV system at the Centro Nacional de Aceleradores (CNA), is quite challenging, since this discrimination is not possible. Nevertheless, the ^{41}K contribution can be estimated and, therefore, corrected, thanks to the sequential detection of the other stable isotope of potassium, ^{39}K (K-correction). Although the sensitivity achieved in ^{41}Ca AMS at low energies is 3-4 orders of magnitude lower than those achieved at larger facilities, it allows the competitive measurements for biomedical applications, and the characterization of concrete samples from nuclear reactor bioshields.

Since ^{41}Ca AMS at low energies is limited to the estimation of ^{41}K interference, it is advisable to study the different ways toward the production of this interference. Some factors related to it have been studied in different experiments performed with the 1 MV AMS system at CNA (SARA) and the 600 kV AMS system at the ETH Laboratory of Ion Beam Physics in Zurich (TANDY). For instance, we could demonstrate that ^{41}K can be injected also as the $(^{41}\text{K}^{57}\text{Fe})^-$ molecular ion. As a consequence, ^{41}K interference is dependent on the materials used during the sample pressing. We also proved that, even when both $^{41}\text{K}/^{40}\text{Ca}$ and $^{39}\text{K}/^{40}\text{Ca}$ ratios change over time, the relation between both, $^{41}\text{K}/^{39}\text{K}$ remains constant. Therefore, the K-correction is a robust method to estimate the ^{41}K interference.

The information provided from these experiments has contributed to the setting up and optimization of the ^{41}Ca measurements with the SARA system at CNA, which was the main goal of this thesis. The results are not only useful for measurements at our system, but also for other very similar HVE 1 MV AMS systems. Several tests have been performed during these years to study and optimize all the performance parameters of ^{41}Ca measurements with this system: ionization efficiency, transmission and destruction of the molecular background in the stripper, ion optical transport, detection efficiency, and final sensitivity.

Mixing the CaF_2 samples with silver powder, our ion source produces stable $(^{40}\text{CaF}_3)^-$ currents between 50 and 150 nA. In comparison with the TANDY system at ETH, the slightly lower transmission for the 2+ state through the helium stripper (40% at SARA, 50% at TANDY) is compensated by the better optical transmission in the high energy sector (90-100% at SARA, 80-85% at TANDY). This is due to the quadrupole triplet which refocus the beam at the exit of our accelerator. The capabilities of both systems for ^{41}Ca AMS are equivalent.

$^{41}\text{Ca}/^{40}\text{Ca}$ backgrounds found in the system, in the 10^{-12} range, allow, among other applications, the characterization of the ^{41}Ca content in the bioshield from nuclear reactors. Within the collaboration between the Spanish radioactive waste management agency (ENRESA) and the AMS Research group at CNA, a detailed study of the ^{41}Ca spatial distribution in the bioshield of the José Cabrera nuclear power plant has been performed. A radiochemical method for concrete samples have been developed in order to deal with the relatively large number of samples involved in this study. The measured $^{41}\text{Ca}/^{40}\text{Ca}$ ratios in the areas of maximum neutron fluence were on the 10^{-6} range, while they get down to the 10^{-10} range in regions far from the reactor cavity. While the $^{41}\text{Ca}/^{40}\text{Ca}$ attenuation profile follows an ideal behavior in some areas, it does not in other parts where the influence of diffused thermal neutrons is higher.

Resumen

La técnica de espectrometría de masas con aceleradores (AMS, por sus siglas en inglés), desarrollada hace 40 años para la datación por ^{14}C , fue pronto utilizada para medir otros radionucleidos de largo período de semidesintegración. Uno de los radionucleidos medidos mediante AMS desde esos primeros años es el ^{41}Ca , y con una gran variedad de aplicaciones. Algunas de éstas son: el cálculo de la edad terrestre de meteoritos, el estudio de reacciones nucleares de interés astrofísico, el estudio del metabolismo del calcio, y la caracterización de residuos nucleares de baja actividad.

El principal reto en las medidas de ^{41}Ca mediante AMS es la interferencia causada por su isóbaro estable, el ^{41}K . Esta interferencia se reduce al usar muestras de fluoruro de calcio (CaF_2) y la extracción del ion (CaF_3^+). En sistemas de AMS de alta energía, además, los iones de ^{41}K pueden ser discriminados frente a los de ^{41}Ca usando distintas técnicas basadas en la dependencia de la pérdida de energía con el número atómico. La medida de ^{41}Ca con sistemas de AMS a baja energía, como el sistema de 1 MV del Centro Nacional de Aceleradores (CNA), es un reto algo mayor, ya que dicha discriminación no es posible. No obstante, la contribución del ^{41}K se puede estimar y, por tanto, corregir, gracias a la detección secuencial del otro isótopo estable del potasio, el ^{39}K (corrección de potasio). Aunque las sensibilidades alcanzadas en las medidas de ^{41}Ca mediante AMS a baja energía están entre 3 y 4 órdenes de magnitud por debajo de aquellas alcanzadas en sistemas de mayor energía, éstas permiten realizar medidas totalmente competitivas para aplicaciones biomédicas, y de caracterización de muestras de hormigón procedentes de blindajes biológicos de reactores nucleares.

Como las medidas de ^{41}Ca mediante AMS a baja energía se ven limitadas a la estimación de la interferencia de ^{41}K , es aconsejable el estudio de las diferentes vías por las que esta interferencia se puede producir. Algunos factores asociados a la misma han sido estudiados mediante distintos experimentos realizados con el sistema de AMS de 1 MV del CNA (SARA) y el sistema de AMS de 600 kV del Laboratorio de Física de Haces de Iones de la ETH de Zúrich (TANDY). Por ejemplo, pudimos demostrar que el ^{41}K también puede ser inyectado como el ion molecular ($^{41}\text{K}^{57}\text{Fe}$). Debido a esto, la interferencia de ^{41}K depende de los materiales

usados durante el prensado de las muestras. También probamos que, incluso siendo ambas relaciones isotópicas, $^{41}\text{K}/^{40}\text{Ca}$ y $^{39}\text{K}/^{40}\text{Ca}$, variables en el tiempo, la relación entre ambas, $^{41}\text{K}/^{39}\text{K}$, permanece constante. Por tanto, se comprueba que la corrección de potasio es un método robusto para la estimación de la interferencia de ^{41}K .

La información obtenida de estos experimentos ha contribuido a la caracterización y optimización de las condiciones de medida de ^{41}Ca con el sistema SARA del CNA, que era el principal objetivo de esta tesis. Los resultados no son sólo útiles para las medidas en nuestro sistema, sino también para otros sistemas de AMS de 1 MV de HVE muy similares. A lo largo de esta tesis se han realizado varias pruebas relacionadas con el estudio y optimización de las condiciones de medida de ^{41}Ca con este sistema: la eficiencia de ionización, la transmisión y la destrucción del fondo molecular en el stripper, el transporte óptico de los iones, la eficiencia de detección, y la sensibilidad final.

Mezclando las muestras de CaF_2 con plata en polvo, nuestra fuente de iones produce corrientes estables de $(^{40}\text{CaF}_3)^-$ entre 50 y 150 nA. En comparación con el sistema TANDY de la ETH, la transmisión ligeramente menor para el estado 2+ en el stripper de helio (40% en SARA, frente a 50% en TANDY) se ve compensada por la mejor transmisión óptica en el sector de alta energía (90-100% en SARA, frente a 80-85% en TANDY). Esto se debe al triplete cuadrupolar que refocaliza el haz a la salida de nuestro acelerador. Las capacidades de ambos sistemas para medidas de ^{41}Ca son equivalentes.

Los fondos de $^{41}\text{Ca}/^{40}\text{Ca}$ en nuestro sistema, del orden de 10^{-12} , permiten, entre otras aplicaciones, la caracterización del contenido de ^{41}Ca en el blindaje biológico de reactores nucleares. Dentro de la colaboración entre la Empresa Nacional de Residuos Radiactivos (ENRESA) y el grupo de investigación en AMS del CNA, se ha llevado a cabo un estudio detallado de la distribución espacial del ^{41}Ca en el blindaje biológico de la central nuclear José Cabrera. Se ha desarrollado un método radioquímico para tratar el número relativamente grande de muestras implicadas en este estudio. Las relaciones $^{41}\text{Ca}/^{40}\text{Ca}$ medidas en las áreas de máxima fluencia neutrónica fueron del orden de 10^{-6} , mientras que estas relaciones bajan hasta el orden de 10^{-10} para aquellas regiones más alejadas de la cavidad del reactor. Mientras que el perfil de atenuación de la relación $^{41}\text{Ca}/^{40}\text{Ca}$ sigue un comportamiento ideal en algunas áreas, este comportamiento no se cumple en otras zonas donde la influencia de la difusión de neutrones térmicos es mayor.

Chapter 1

Introduction

1.1 ^{41}Ca basic data and general applications

^{41}Ca is a radionuclide which decays to ^{41}K by electron capture. The most recent and precise measurement of the half-life of this decay is $(9.94 \pm 0.15) \times 10^4$ years [Jörg et al., 2012]. The electron capture produces the emission of Auger electrons with an energy of 3.97 keV in a 76.6% of the cases, and X-rays from the K-shell of potassium (with energies of 3.3 keV or 3.59 keV) in a 12.47% of the cases [National Nuclear Data Center, n.d.]. The measurement of ^{41}Ca in a sample by radiometric techniques presents two main challenges:

- 1: The detection of these low energy X-rays or electrons is typically difficult because of the possible interferences in the detector from X-ray or β emitters [Hou and Roos, 2008].
- 2: Because of its long half-life, it requires huge amounts of ^{41}Ca atoms or very long measuring times in order to be able to detect a significant decay events.

The main radiometric technique used to measure ^{41}Ca is the detection of its Auger electrons by liquid scintillation counting (LSC). LSC has a higher counting efficiency than X-ray spectrometry and, as it was said, Auger electrons from ^{41}Ca are more abundant than X-rays. Detection limits down to 0.1 Bq have been reported for LSC, while that one for X-ray counting is 8 Bq [Hou, 2005].

However, this detection limit of 0.1 Bq only enables the application of ^{41}Ca measurements to the characterization of nuclear waste. The most common application of ^{41}Ca LSC is the characterization of concrete samples coming from the most activated areas of the bioshield of nuclear power plants. The most important reaction producing ^{41}Ca is the thermal neutron

capture on its stable isotope, ^{40}Ca , with a cross section of 400 ± 40 mb [Cranston and White, 1971]. That is the reason why, in the bioshield concrete, where thermal neutron fluence reaches levels up to 10^{19} cm^{-2} , and where calcium is one of the most common elements, ^{41}Ca activities can be relatively high. Even in this case, some areas from the bioshield could not be measured by LSC and sample mass required are typically higher than 1 g, which involves the necessity of radiological precautions.

For a complete study of the ^{41}Ca spatial distribution in this concrete structure, the use of an ultra-trace technique such as accelerator mass spectrometry (AMS) becomes necessary. The bases of AMS will be presented in section 1.2. This technique requires the chemical treatment of the sample, but so does LSC. Besides, for samples which can be measured with LSC, AMS measurements typically present much lower uncertainties. The presence of ^{41}Ca in other contexts is usually so low that AMS is the only option to measure this ^{41}Ca content.

The $^{40}\text{Ca}(n,\gamma)^{41}\text{Ca}$ reaction is also the main production pathway on Earth surface for naturally occurring ^{41}Ca . At sea level, secondary neutrons produced in the atmosphere represent a 98% of the total nucleonic cosmic flux. Although the energy spectrum of these neutrons has an important high energy branch, the capture cross section for these neutron energies is lower than 1 mb [Bergqvist et al., 1974]. Because of the different behaviour of thermal neutrons in different materials, the saturation $^{41}\text{Ca}/^{40}\text{Ca}$ isotopic ratio depends on the chemical composition of the rock, and it typically is in the 10^{-14} level or lower [Dunai, 2010]. This saturation isotopic ratio is

$$\left(\frac{^{41}\text{Ca}}{^{40}\text{Ca}}\right)_{\text{sat}} = \frac{\varphi\sigma}{\lambda}, \quad (1.1)$$

where φ , σ and λ are, respectively, the thermal neutron flux, the thermal neutron capture cross section from ^{40}Ca , and the ^{41}Ca decay constant.

Since ^{41}Ca half-life is ~ 18 times higher than the one of ^{14}C , its use for dating purposes was considered in early years [Raisbeck and Yiou, 1979]. However, ^{41}Ca is not produced in the atmosphere, but only in the lithosphere, so it would be a condition that the dated material stayed shielded so that the ^{41}Ca production stopped. In any case, $^{41}\text{Ca}/^{40}\text{Ca}$ ratio in these samples would be lower than 10^{-15} , which is extremely low even for AMS, and isotope enrichment would be necessary [Steinhof et al., 1989]. The possibility of using ^{41}Ca to date human and/or animal remains has not been proven so far.

A very different case is the application of ^{41}Ca measurements for the calculation of the terrestrial age of meteorites. In outer space, cosmic radiation is much higher than on Earth surface. Nevertheless, primary cosmic neutrons present much higher energies in this case,

and charged particles (mainly protons and α particles) with energies of several hundreds of MeV per nucleon are the major components of cosmic rays [Dunai, 2010]. Because of this, neutron capture becomes a less relevant reaction in ⁴¹Ca production, while spallation reactions in slightly heavier elements, like iron and nickel, become more important [Kubik et al., 1986]. For instance, the cross section of the ^{nat}Fe(p,x)⁴¹Ca spallation reaction for proton energies higher than 100 MeV reach levels up to 10 mb [Fink et al., 1987].

The relevance of neutron capture in ⁴¹Ca production in extraterrestrial material depends on the chemical composition. For iron falls, it is totally negligible, and ⁴¹Ca concentrations, instead of ⁴¹Ca/⁴⁰Ca ratios, are measured. The ⁴¹Ca concentrations in these kind of meteorites before falling to the Earth are in the 10¹² atoms·kg⁻¹ level [Fink et al., 1991]. In stony meteorites, the contribution of the ⁴⁰Ca(n, γ)⁴¹Ca reaction depends also on the size of the meteorite, since higher volumes allow the moderation of fast neutrons to lower energies where the capture cross section is much higher. Saturation ⁴¹Ca concentrations, nevertheless, are only slightly higher than in iron falls, and ⁴¹Ca/⁴⁰Ca ratios are usually in the 10⁻¹² level [Welten et al., 2007]. The neutron capture on ⁴⁰Ca becomes the main ⁴¹Ca production pathway on Moon surface. Nishiizumi et al. [1997] measured the ⁴¹Ca depth profile in a drill core taken by the Apollo 15. The ⁴¹Ca/⁴⁰Ca ratios were between 1.5×10^{-13} and 1.9×10^{-12} .

These ⁴¹Ca/⁴⁰Ca isotopic ratios have been demonstrated to be much higher in the early ages of the solar system, since primitive meteorites have shown a clear excess on its ⁴¹K/³⁹K isotopic ratio which can only be explained by ⁴¹Ca decay and an original ⁴¹Ca/⁴⁰Ca ratio around 10⁻⁸ [Srinivasan et al., 1994]. In order to study the possible irradiation scenarios in the early solar system, the cross sections of the different nuclear reactions leading to ⁴¹Ca production have to be measured. ⁴¹Ca AMS measurements of irradiated materials in several facilities have already been useful to the measurement of different cross sections relevant in this case and other cases of astrophysical interest. Some examples are: proton spallation reactions in iron, nickel and titanium [Fink et al., 1987], the ^{nat}Ca(³He,x)⁴¹Ca transfer reaction [Herzog et al., 2011], and the stellar capture neutron cross section on ⁴⁰Ca [Dillmann et al., 2009].

Anthropogenic ⁴¹Ca on Earth surface can be found in areas where nuclear bombs exploded. A clear example is Hiroshima, where Rühm et al. [1992] measured the ⁴¹Ca depth profile in a granite gravestone located 107 m from the hypocenter of Little Boy explosion. ⁴¹Ca/⁴⁰Ca ratio in the surface of this gravestone was found to be almost 10⁻¹¹, much higher than natural one on Earth. A much higher ⁴¹Ca/⁴⁰Ca ratio, 1.058×10^{-10} , was found by Lachner et al. [2014] in the Castle Bravo crater on the Bikini Atoll, produced by the test explosion of a hydrogen bomb on 1954. Most of the other thermonuclear tests were carried out detonating the devices at much higher altitudes, so the neutron fluence on surface was much lower; or underground, so the ground material between the detonation and the surface shielded the neutrons.

Nowadays, though, the most common application of ^{41}Ca does not come from its natural cosmogenic or anthropogenic production, but from its biomedical capability as a tracer of calcium metabolism [Elmore et al., 1990; Freeman et al., 1997]. The use of ^{41}Ca has none of the disadvantages from other calcium radioisotopes or its stable isotopes:

- In the first case, the radiological hazard of the administration of a dose of ^{45}Ca or ^{47}Ca , which half-lives of 165 days and 4.5 days respectively, would be higher, and they allow much lower tracing times because of their decay, while ^{41}Ca is only limited by its biological excretion. By contrast, ^{41}Ca oral doses up to 3700 Bq are actually been used [Denk et al., 2006]; taking into account that the dose coefficient for ingested ^{41}Ca is $2.9 \times 10^{-10} \text{ Sv}\cdot\text{Bq}^{-1}$ [ICRP, 2012], the dose in 50 years would be around $1 \mu\text{Sv}$. This dose is totally negligible, since it is much lower than, for instance, the annual natural background exposure (typically higher than 1 mSv).
- In the second case, stable isotopes of calcium such as ^{42}Ca or ^{44}Ca require high chemical doses so that their isotopic abundances change significantly. Since ^{41}Ca is not naturally present, if the dose has a relatively high $^{41}\text{Ca}/^{40}\text{Ca}$ ratio very low calcium content has to be administered in order to be able to measure ^{41}Ca concentrations in tissues where calcium is incorporated.

A very recent compendium of calcium metabolism studies performed with ^{41}Ca tracing and AMS measurements is found in Weaver et al. [2017].

1.2 Accelerator Mass Spectrometry (AMS): finding a needle in a haystack

Contents from any radionuclide with a relatively long half-life, such as ^{41}Ca , are intrinsically hard to measure by radiometric techniques because of the very low related activities. Its direct detection with conventional mass spectrometry systems meet with the interference of molecular ions with the same mass that the radionuclide of interest. All the mass spectrometry systems follow the same basic scheme: ionization of the sample, the use of electromagnetic separators to select its mass/charge ratio, and detection of these ions. Since the contents of long-lived radionuclides are typically orders of magnitude below the part per million (ppm) level, even a trace production of isobar molecular ions would make it impossible to measure of the radionuclide of interest.

Accelerator Mass Spectrometry (AMS) solves this problem thanks to the electron stripping

1.2. ACCELERATOR MASS SPECTROMETRY (AMS): FINDING A NEEDLE IN A HAYSTACK

process with a solid or gaseous target that takes place at energies available with particle accelerators. In this process, the molecular background is destroyed (see Figure 1.1).

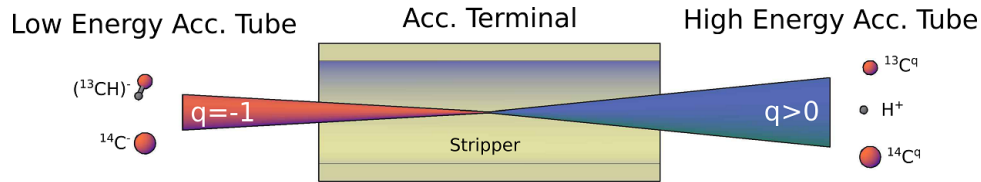


Figure 1.1: Basic scheme of the stripping process.

Other suppression processes, though, are necessary to solve the possible interference from stable isobars. Figure 1.2 shows the basic scheme of a common AMS system, together with the other isobar suppression techniques used in AMS:

- **Ionization:** negative ionization provides, in some cases, a first suppression or reduction of the interference from the stable isobar, because of the instability of negative ions from elements or molecules with a negative electron affinity (EA). This is the case, for instance, of ^{14}C , since ^{14}N does not form negative ions [Bennett et al., 1977]. Even if that EA is positive, but very low, its interference is reduced several orders of magnitude, since the negative ion production efficiency increases exponentially with the EA [Alton, 1993].

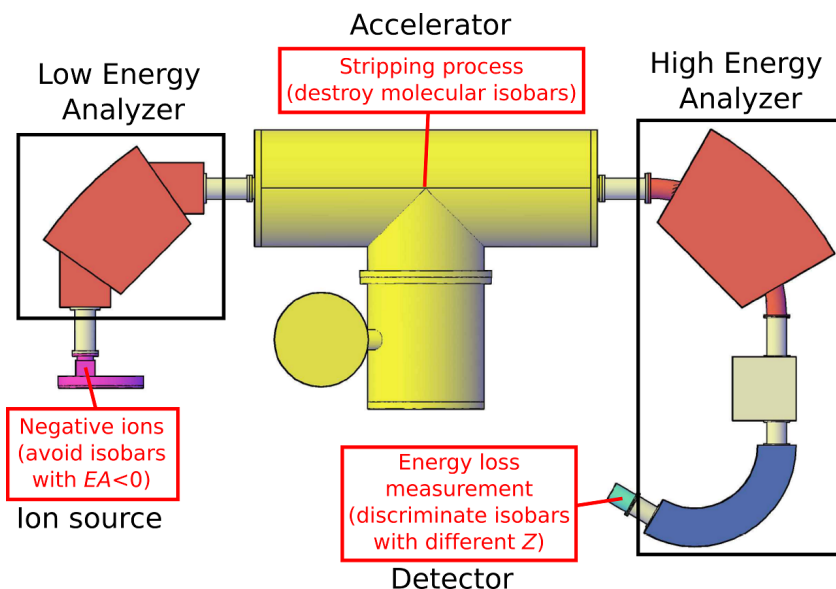


Figure 1.2: Basic scheme of an AMS system. While the possibility of suppression of stable isobars depends on the radionuclide and experimental system, the use of the stripping process to destroy the molecular isobars is common to all AMS measurements.

- **Detection:** techniques based on the different energy loss can be used because of the high energies of the ions. Since the energy loss in a material depends on the atomic number Z of the ion, the difference in the energy loss between the radionuclide of interest and its stable isobar can be used to reduce the interference entering the detector and separating both signals.

The AMS technique, initially developed for ^{14}C measurements, was soon applied to many other long-lived radionuclides, including ^{41}Ca [Gove et al., 1979; Elmore and Phillips, 1987]. Table 1.1 shows some of the most important "AMS radionuclides".

Table 1.1: Common radionuclides measured by AMS. Half-lives from National Nuclear Data Center [n.d.], except for ^{10}Be [Korschinek et al., 2010]. The main technique used to suppress/reduce the interference caused by the stable isobar is also shown: "Ionization" refers to those cases where the negative ion of the stable isobar is unstable or metastable; "Detection", to those cases where the different energy loss is used to distinguish the radionuclide from its stable isobar.

Radionuclide	Half-life (My)	Negative ion	Stable isobar	Suppression / reduction
^{10}Be	1.387	$(\text{BeO})^-$	^{10}B	Detection
^{14}C	0.0057	C^-	^{14}N	Ionization
^{26}Al	0.717	Al^- $(\text{AlO})^-$	^{26}Mg	Ionization Detection
^{36}Cl	0.301	Cl^-	^{36}Ar ^{36}S	Ionization Detection
^{41}Ca	0.0994	$(\text{CaH}_3)^-$ $(\text{CaF}_3)^-$	^{41}K	Ionization + detection
^{129}I	15.7	I^-	^{129}Xe	Ionization
^{236}U	23.42	$(\text{UO})^-$	\nexists	

1.2.1 ^{41}Ca AMS

In the particular case of ^{41}Ca , two different chemical forms and their respective negative ions can be used in order to deal with its stable isobar, ^{41}K : calcium hydride (CaH_2), and extraction of the $(\text{CaH}_3)^-$ ion; or calcium fluoride (CaF_2), and extraction of the $(\text{CaF}_3)^-$ ion. The choice of one material or the other depends on several factors, since each one has both advantages and disadvantages:

- **CaH_2 :** the main advantage of selecting the $(^{41}\text{CaH}_3)^-$ ion in the LE side is the instability of the $(\text{KH}_3)^-$ ion. A $^{41}\text{K}/^{40}\text{Ca}$ interference in the level of 10^{-13} is typically found from the

contribution of $(^{41}\text{KH}_2)^-$ ions where one of the 2 hydrogen nuclides is a deuterium (^2H) [Fink et al., 1990]. The main disadvantage is the high hygroscopy of CaH_2 , which makes its handling problematic, making it necessary to minimize its contact with air [Sharma and Middleton, 1987]. This choice is suitable for applications where few samples are measured and very high sensitivities are required, like the measurement of accretion rate of extraterrestrial ^{41}Ca in Antarctica [Gómez-Guzmán et al., 2015].

- **CaF₂**: in contrast, calcium fluoride chemical preparation is more simple and it is a chemically stable salt [Kubik and Elmore, 1989]. However, the $(\text{KF}_3)^-$ ion is stable, even when its stability is much lower than that from $(\text{CaF}_3)^-$, leading to a higher $^{41}\text{K}/^{40}\text{Ca}$ interference in the level of 10^{-12} - 10^{-11} [Zhao et al., 2010]. Ion source output currents are also slightly lower [Middleton, 1990], but in this case the difference is not so important. This choice is suitable for applications where large numbers of samples are involved and relatively lower sensitivities are required, like the biomedical applications detailed in section 1.1 [Freeman et al., 1995].

In any case, in conventional AMS facilities, which typically use terminal voltages higher than 3 MV, the different energy loss on a material, as it was already stated, can be used to separate the signals of ^{41}Ca and ^{41}K in the detector [Fink et al., 1990; Vockenhuber et al., 2005; Wallner et al., 2010; Hosoya et al., 2017]. Better separation between both signals can be achieved at higher energies, resulting in a lower fraction of ^{41}K counts that interfere with the ^{41}Ca counts. The performance parameters for ^{41}Ca from several AMS facilities are presented in Table 1.2. The layouts from these systems are shown in Figure 1.3.

Table 1.2: ^{41}Ca performance parameters from different AMS facilities. Only data from measurements using calcium fluoride are used, even when Wallner et al. [2010] presents also performance parameters with hydride.

Facility	VERA (Vienna, Austria)	DREAMS (Dresden, Germany)	14UD ANU (Canberra, Australia)
References	[Wallner et al., 2010]	[Akhmadaliev et al., 2013] [Rugel et al., 2016]	[Fifield et al., 2010]
Terminal voltage (MV)	3	6	14
Stripper material	O ₂ gas	Ar gas	O ₂ gas + C foil
HE side charge state	4+	4+	7+
Background ($\times 10^{-15}$)	50	2	1

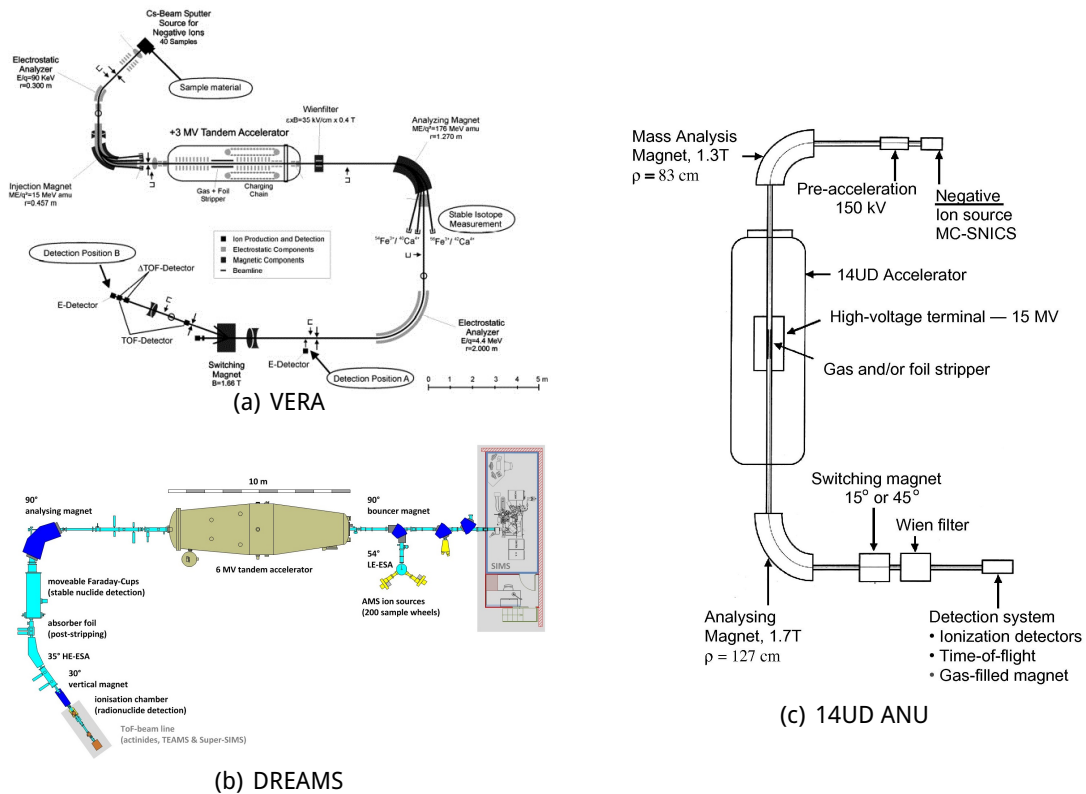


Figure 1.3: Layout of several AMS facilities: the 3 MV system at the Universität Wien (a), the 6 MV system at the Helmholtz-Zentrum Dresden-Rossendorf (b) and the 14 MV system at the Australian National University (c).

1.3 AMS at low energies

During the first decades of AMS it was believed that, in order to destroy the molecular background, charge states higher or equal to 3+ had to be selected (“golden rule” of AMS). Molecular ions with those charge states become unstable because of the electrostatic repulsion [Suter, 1990]. With compact particle accelerators with terminal voltages ≤ 1 MV, though, the most populated charge states for carbon ions are 1+ and 2+ [Jacob et al., 2000] and molecular interferences would still survive. Despite this fact, Lee et al. [1984] and Suter et al. [1997] showed that, if the stripper mass thickness of the stripper was high enough, this molecular background was reduced to negligible levels.

Based on these results, the first low-energy AMS system for ^{14}C measurements was developed: the 600 kV AMS system at ETH Zurich, TANDY, developed by the ETH Laboratory of Ion Beams Physics (LIP) in collaboration with National Electrostatics Corp. (NEC, USA) [Synal et al., 2000]. Soon, the capabilities of this system for other AMS radionuclides were studied

and, since then, the system has also performed routine measurements of ^{10}Be , ^{26}Al , ^{41}Ca , ^{129}I and actinides (^{236}U , Pu isotopes...) [Stocker et al., 2004, 2005]. The first 1 MV AMS system designed by High Voltage Engineering Europa B.V. (HVE, Netherlands) was initially designed to measure not only ^{14}C , but also other typical AMS radionuclides, such as ^{10}Be and ^{26}Al [Klein et al., 2006, 2007], and installed at the Centro Nacional de Aceleradores (CNA) in Seville. The peculiarities from these systems and the developments implemented on them are presented in chapter 2.

These small accelerators, nevertheless, still have some properties in common with larger machines, like the need of using some dielectric gas, as sulfur hexafluoride, to electrically insulate the terminal from the accelerator tank. This necessity does not apply any more when even lower terminal voltages are used, and vacuum insulation is enough to avoid discharges. This is the case of the MICADAS system, a system developed by the ETH LIP whose terminal voltage is provided by a 200 kV HV power supply [Synal et al., 2007]. The MICADAS system is designed only for ^{14}C measurements. A new multi-element AMS system whose terminal voltage is provided by a 300 kV HV power supply is now being developed also by the ETH LIP [Maxeiner, 2016].

The use of low-energy AMS systems reduce the operating and maintenance costs of these facilities. The original cost of the system is also lower. Furthermore, their sizes allow them to be placed in conventional laboratory rooms and no huge and dedicated halls are required to be built.

1.4 Motivation and outline

The main goal of this thesis has been the setting up and optimization of the performance parameters of the 1 MV AMS system at CNA for ^{41}Ca . Since its operation started in 2006 [Klein et al., 2006], the AMS research group at CNA has looked for exploiting the multi-element capacity of the system [Klein et al., 2007; Chamizo et al., 2008b]. The same setting up and optimization of the performance has been performed, for instance, for ^{10}Be and ^{26}Al [Ruiz-Gómez et al., 2010; Padilla, 2015; Scognamiglio, 2017], for ^{129}I [Gómez-Guzmán, 2010; Gómez-Guzmán et al., 2012], for ^{236}U [Chamizo et al., 2015a], and for Pu isotopes [Chamizo et al., 2008a; Chamizo, 2009]. Several technical changes and developments have been performed in collaboration with both, HVE and the ETH LIP [Chamizo et al., 2015c; Scognamiglio et al., 2016].

Nowadays, there exist several AMS facilities around the world similar to the 1 MV system at CNA. Thus, the study of the performance of its different elements are also useful to other

research groups, so they can exploit the capacities of their HVE 1 MV AMS systems. Some of these groups actually included ^{41}Ca in their acceptance tests [Klein et al., 2013; Heinemeier et al., 2015], so it can be said that they are interested on performing routine ^{41}Ca measurements in the future. The results provided by this thesis, specially those also published in Vivo-Vilches et al. [2017], are useful to these groups as much as it is to ours.

This thesis included a stay of four months at ETH LIP in order to perform some experiments related to the ^{41}K interference in ^{41}Ca AMS at low energies. The stay also included the collaboration with the ETH LIP in the ^{41}Ca measurements for biomedical applications performed by them for the NutriTrace group at the National University of Singapore. The information and experience acquired during this stay was really helpful in order to optimize the ^{41}Ca measurement performance of the 1 MV AMS system at CNA Seville.

Even when the study of the capabilities of the system for new radionuclides and technical developments themselves are two of its main research lines, our group has also focused on some important application research lines. These research lines include the development of chemical procedures for the sample preparation. Nowadays, the most important applications performed by our group are:

- Environmental applications, specially related to oceanography [Chamizo et al., 2015b, 2016; López-Lora et al., 2018; Vivo-Vilches et al., 2018].
- Characterization of Low-Level Waste (LLW) from operating and decommissioning nuclear power plants, in collaboration with the Spanish radioactive waste management agency, ENRESA [López-Gutiérrez et al., 2013].

Radiocarbon applications are no longer performed with the 1 MV AMS system since the group acquired a MICADAS system in 2012.

The ^{41}Ca AMS measurements in the group have been implemented initially in the LLW characterization project. $^{41}\text{Ca}/^{40}\text{Ca}$ ratios have been measured in concrete samples from several locations different in both radial and vertical coordinates from the primary shield of a decommissioning nuclear power plant (NPP): the José Cabrera NPP. The results from these measurements will be presented in chapter 5.

Even if we did not perform measurements for biomedical applications at CNA Seville, we did chemical tests with urine samples. We also showed that the performance of the 1 MV AMS system is well suited to perform those measurements for any interested group.

This first chapter was provided in order to introduce the reader to the applications of ^{41}Ca measurements, the AMS technique and its evolution to low energy systems.

In [chapter 2](#), a description of the fundamental principles of the most important elements in an AMS system is presented. The two systems used in the experiments carried out during this PhD thesis are also concisely described, from which a more detailed description can be found in [Chamizo \[2009\]](#): the 1 MV AMS system at CNA Seville, SARA (*Spanish Accelerator for Radionuclide Analysis*); and the 600 kV AMS system at ETH Zurich, TANDY.

The specific challenges related to ^{41}Ca AMS at low energies and how the ^{41}K interference can be estimated thanks to the detection of the other stable isotope of potassium, ^{39}K (K-correction) [[Vockenhuber et al., 2015](#)] are presented in [chapter 3](#). Some experiments performed on both compact AMS systems (SARA and TANDY) providing information about the production pathways of the ^{41}K interference are also presented, as well as the specific complexity introduced to the data analysis by the K-correction. Because of this complexity, 2 similar programs, one for each AMS system, were written in FORTRAN code to perform the data analysis.

The experiments in order to set-up and optimize the ^{41}Ca measurements with the SARA system are presented in [chapter 4](#). These experiments include the characterization and optimization of the ion source current output, the transmission using He as a stripper gas, the detection efficiency, and the performance with blank samples (with negligible content of ^{41}Ca) and standard samples (with known $^{41}\text{Ca}/^{40}\text{Ca}$ ratios). A comparison of the performance parameters with those from the TANDY system is shown, together with the measurements of some of the ETH in-house standard samples used in the measurements with that system and an intercomparison experiment carried out on some of the biomedical samples which were measured during the stay at [ETH LIP](#).

Results from the ^{41}Ca measurements with the SARA system of the concrete samples from the primary shield of the José Cabrera Nuclear Power Plant are presented in [chapter 5](#). These results are preceded by the exposition of the way the ^{41}Ca is produced in the concrete of the primary shield, and how the $^{41}\text{Ca}/^{40}\text{Ca}$ can give information about the thermal neutron fluence the shield was exposed to during the operation of the power plant.

The [last chapter](#) summarizes the most important conclusions of this work.

Chapter 2

Comparative description of the experimental systems

2.1 General overview of the systems

In this chapter, the basic physical principles from the typical elements of [AMS](#) systems are presented, together with the characteristics of each one of these elements for the systems used during this thesis (the SARA system at [CNA](#) Seville and the TANDY system at ETH Zurich). Both systems are described in detail in [Chamizo \[2009\]](#). Additional information about the TANDY system can be found in [Jacob \[2001\]](#). This chapter, therefore, focuses on the changes implemented since then and the features which are specially important for ^{41}Ca measurements.

This first section presents a general overview of both systems. The next sections present:

- The production of negative ions by Cs sputtering ([section 2.2](#)).
- The operation and optical properties of tandem accelerators, together with the basic characteristics of the stripping process ([section 2.3](#)).
- The kinematic filters used in [AMS](#), and the two different sectors: the [LE](#) injector and the [HE](#) spectrometer ([section 2.4](#)).
- The charged particle detection with gas ionization chambers ([section 2.5](#)).

In some of this sections, simulations performed with GICOSY [[Weick, n.d.](#)] are presented. The input files from these simulations are shown in [Appendix A](#).

2.1.1 The 1 MV AMS system at CNA Seville: SARA

The *Spanish Accelerator for Radionuclide Analysis* (SARA) was the first 1 MV AMS system developed by HVE [Klein et al., 2006, 2007; Chamizo et al., 2008b]. Nowadays, there exist several systems using the same model of the 1 MV tandemtron, some of them with a similar system layout as SARA [Klein et al., 2013], others with a modified one [Heinemeier et al., 2015]. The system was originally designed to measure not only ^{14}C , but other AMS radionuclides. A picture and a schematic view of the system are presented in Figure 2.1.

The most important changes implemented in the recent years are:

- The upgrade of the ion source to the HVE SO-110B sputtering source [Arnold et al., 2010; Chamizo et al., 2015c].



© Francesco Valerio

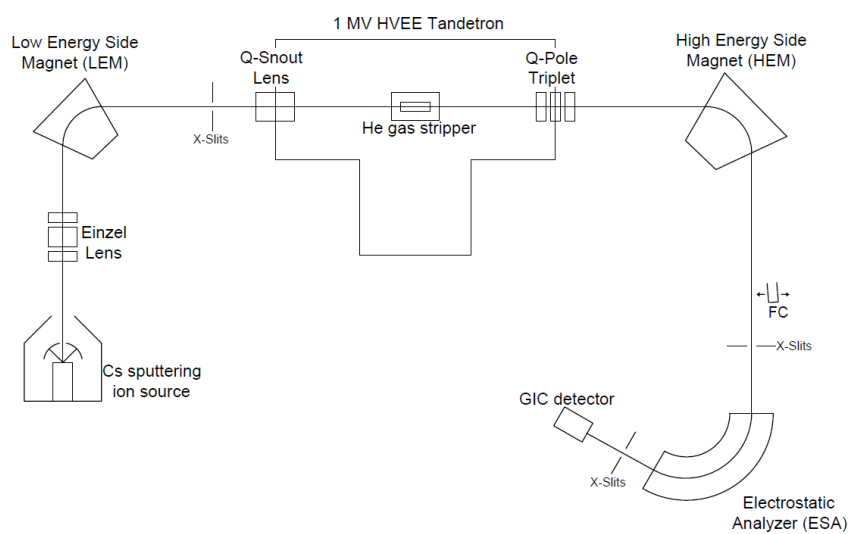


Figure 2.1: Picture and schematic view of the 1 MV AMS system at CNA Seville.

- The change of the stripper gas from Ar to He [Scognamiglio et al., 2016].
- The replacement of the original HVE detector with a compact gas ionization chamber (GIC) developed by the ETH LIP [Müller et al., 2012; Scognamiglio et al., 2016].

2.1.2 The 600 kV AMS system at ETH Zurich: TANDY

The TANDY system was the first compact AMS system in the world, developed by the ETH Laboratory of Ion Beam Physics (LIP) in collaboration with National Electrostatics Corp. (NEC).

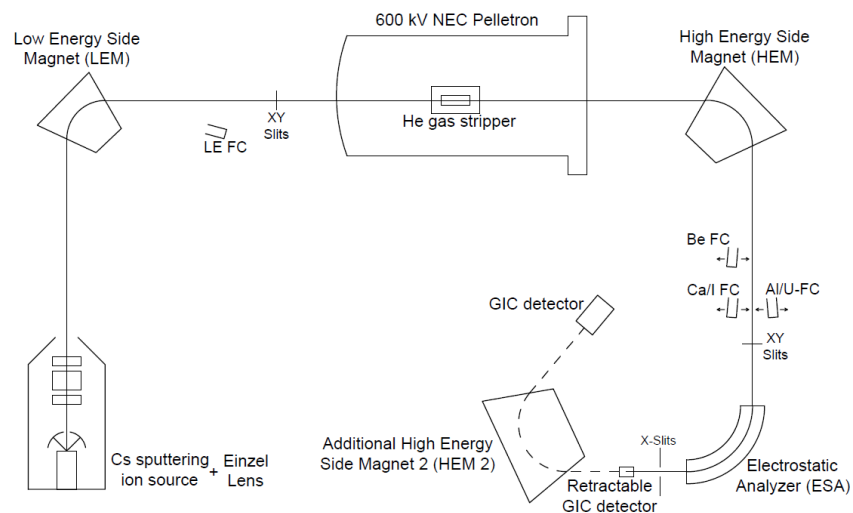
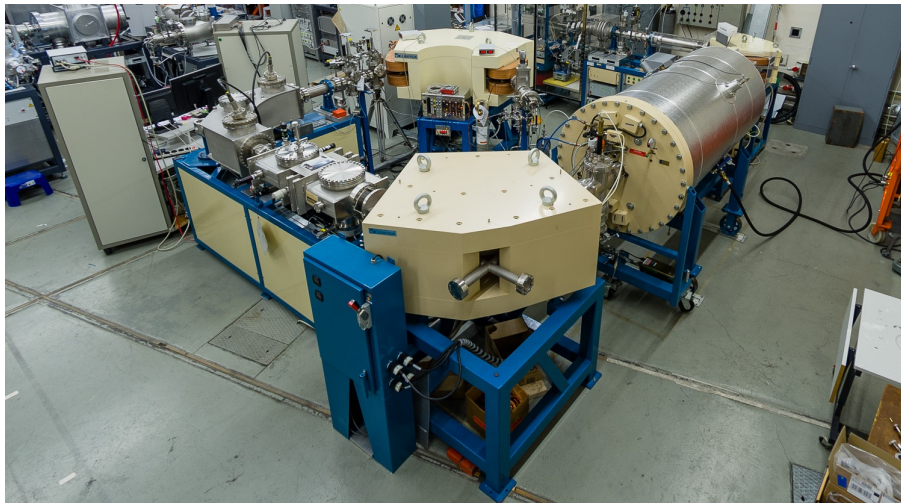


Figure 2.2: Picture and schematic view of the 600 kV AMS system at ETH. The dashed line represent the beam path for ions passing to the additional magnet. In ^{41}Ca measurements, the retractable gas ionization chamber (GIC) is used, so the ions do not reach this magnet.

It was originally designed to measure only ^{14}C selecting the 1+ charge state in the HE side [Synal et al., 2000; Jacob et al., 2000]. Nevertheless, it was soon upgraded to measure other radionuclides [Stocker et al., 2004, 2005; Stocker, 2006]. Actually, ^{14}C measurements are no longer performed in the system, but in the original MICADAS system at ETH. Figure 2.2 shows a picture and a schematic view of the system.

The most important changes implemented in the recent years are:

- Modifications of the NEC MC-SNICS ion source, being the most important the replacement of the ionizer [Müller et al., 2010].
- The change of the stripper gas from Ar to He [Vockenhuber et al., 2013].
- The design and installation of an additional magnet in the high energy side (HEM 2), after the electrostatic analyzer (ESA) [Müller et al., 2010]. This magnet is not used in ^{41}Ca measurements because of the high optical losses for this radionuclide.

2.2 Cs sputtering ion sources

Negative ionization is the first stage of almost all the AMS systems. The most common negative ion sources used in AMS are the Cs sputtering sources. In these, Cs^+ ions are produced by surface ionization and attracted to the sample target, since it is connected to a negative potential. These collisions produce multiple ions in different charge states, but only the negative ones are accelerated out of the sample by the negative potential. The production of ions with charges $\leq -2e$ is negligible. If the potential to which the sample is connected is $-V_0$, the kinetic energy of the ions with charge $-e$ after the ion source system will be eV_0 .

Depending on how the Cs^+ ions are produced and accelerated to the sample target, the sput-

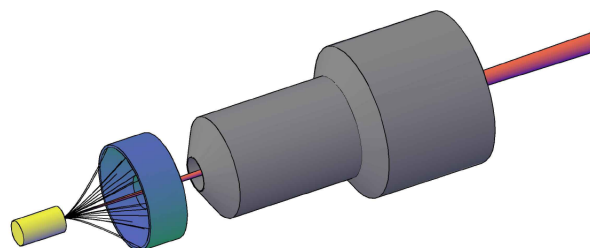


Figure 2.3: Scheme of a high-current sputtering ion source. The black lines represent the Cs^+ ions going from the ionizer to the target. The red cone represents the negative ion beam leaving the target.

tering sources are separated in different types, but the most used nowadays is the high-current sputtering ion source. A basic scheme of one of these sources is shown in Figure 2.3. The ion source chamber is filled with gaseous Cs which, in contact with a wolfram surface heated to high temperatures (ionizer) produces the Cs^+ ions. This surface is connected to a negative electric potential $-V_{\text{source}} > -V_0$; as a result of the lower potential on the sample target, the Cs^+ ions are attracted to this, reaching it with a kinetic energy

$$eV_{\text{Cs}} = e(V_0 - V_{\text{source}}). \quad (2.1)$$

The negative ions are accelerated in the opposite direction by this same potential difference. Typically, an electrode connected to potentials closer to 0 is located after the ionizer to extract the ions which reach the aperture in the center of the ionizer (extraction cone). Both systems presented in this chapter use this kind of ion source.

A common element used to refocus the ion beam after the ion source is the Einzel lens. This lens consists of a set of three cylindrical electrodes, as the one we can see in Figure 2.4, where the two side electrodes are connected to an electric potential, but the central electrode to a different one. The dependence of the electric field with both coordinates, radial and axial, has an optical effect on the ions.

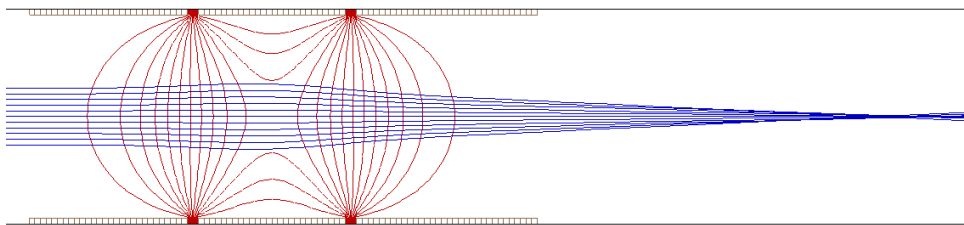


Figure 2.4: Simulation of ions passing through an Einzel lens on SIMION® [SIS, n.d.]. The red lines represent the equipotential lines to which the electric field is perpendicular.

2.2.1 The SO-110B ion source at SARA

At SARA, samples are introduced in the system individually in a *carousel*, each target screwed to a holder, and are driven to the ion source by a piston, as it is shown in Figure 2.5. This way, the rest of the samples are not in contact with the Cs gas. The sample *carousel* can carry 200 samples. When the *carousel* is open to introduce and/or extract the targets, a guillotine closes its connection to the rest of the ion source to avoid the air entering it.

The schematic view on SIMION® of the SO-110B source and the Einzel lens placed just after-

wards is presented in [Figure 2.6](#). The extraction cone is connected to ground potential, and so do the two side electrodes of the Einzel lens. The potential $V_{\text{lens}} < 0$ of the central electrode can be changed to optimize the final image of the ion source system. The extraction cone can be slightly displaced in the 3 axes to change the electric field between it and the ionizer, optimizing the focusing of the beam.

Most of the measurements performed with SARA use a $-V_0$ potential of -35 kV, so the energy of the negative ions in the LE side is 35 keV, independently of the terminal voltage used. This can be done thanks to the use of an electrostatic lens at the entrance of the accelerator, as it is explained in the [next section](#).

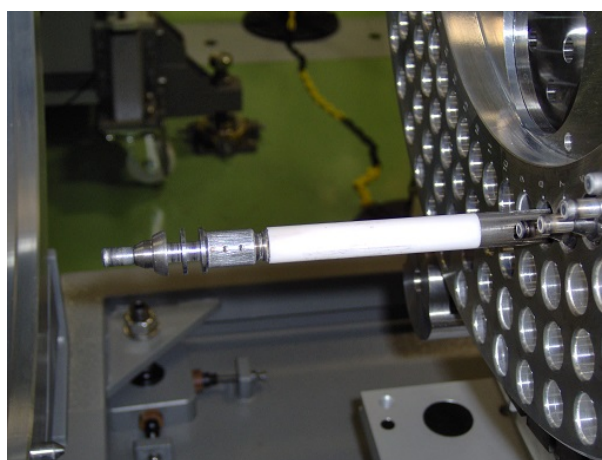


Figure 2.5: Piston taking a target out of the SARA sample *carousel*.

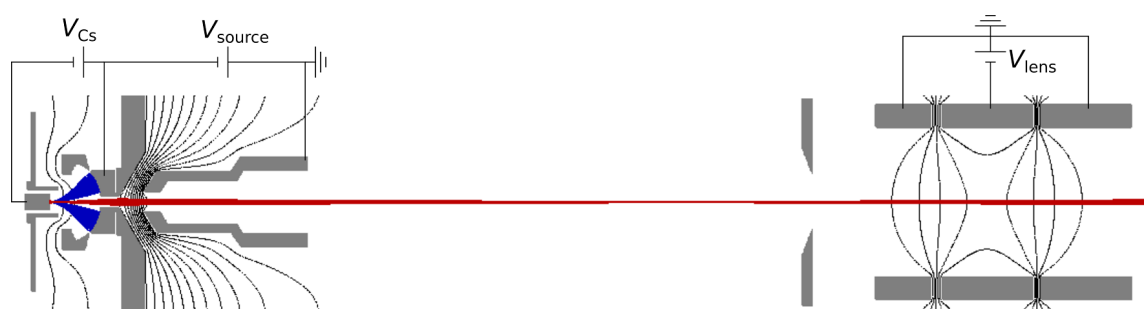


Figure 2.6: SIMION® simulation of the SO-110B ion source. Blue lines represent Cs^+ ions; red lines, the negative ion beam; black lines, equipotential lines.

2.2.2 The modified MC-SNICS ion source at TANDY

For the MC-SNICS ion source used by TANDY, targets are introduced inserting them in a wheel, which is screwed to the system. In [Figure 2.7](#), this target wheel is shown. Each wheel has slots

enough for 40 targets. If some slots are not used, aluminum targets (dummies) are placed in the slot. As a result of this design, when a target is sputtered, the nearby targets are in contact with the Cs gas. A guillotine closes the connection to the rest of the ion source while the wheel is being changed.

The new ionizer was manufactured by Spectra-Mac, Inc. (USA). This ionizer has a spherical surface, unlike the old one which had a conical geometry. A simulation of the whole ion source system with SIMION® files provided by the [ETH LIP](#) is presented in [Figure 2.8](#). In this case, the extraction cone is connected to a selectable negative potential. The side electrodes of the Einzel lens are connected to the same potential as the extraction cone, while the central one is connected to an additional selectable negative potential. The final increase to ground potential is reached through an acceleration tube placed after this whole system, so the electric fields are typically much lower than the maximum electric fields reached in the ion source from SARA.

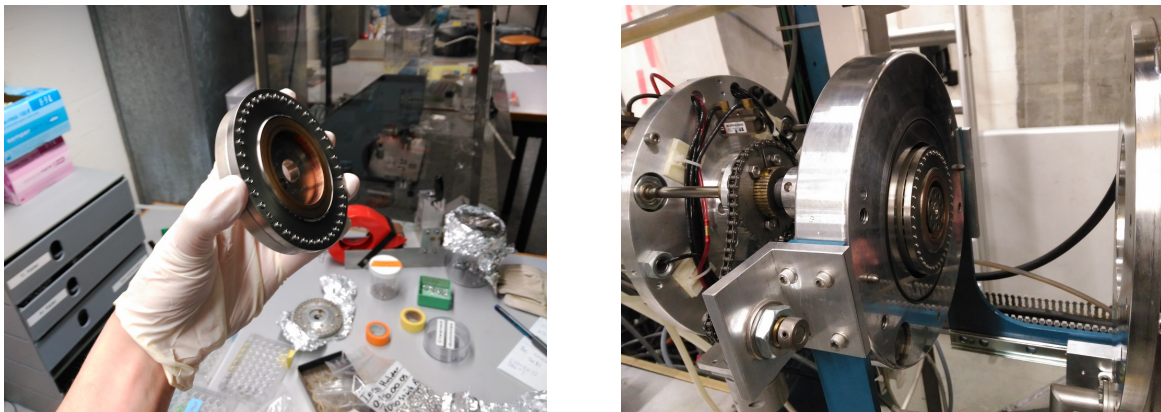


Figure 2.7: Target wheel used by the MC-SNICS ion source.

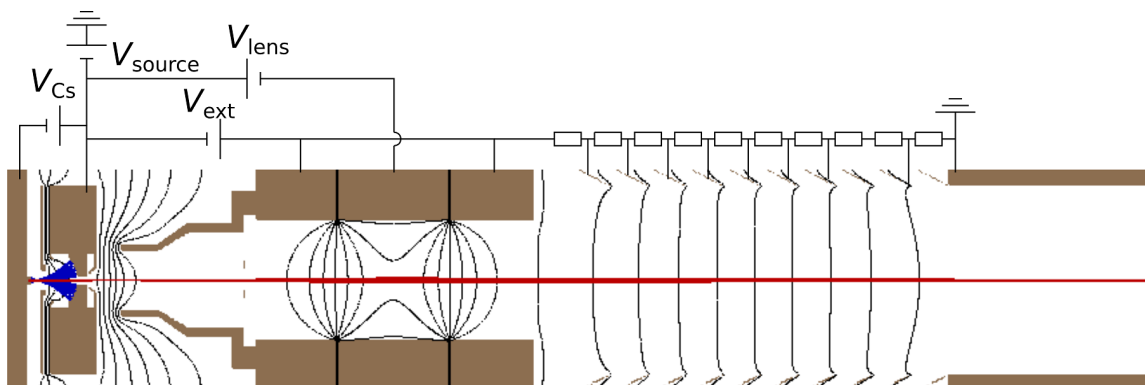


Figure 2.8: SIMION® simulation of the ion source from TANDY. Blue lines represent Cs^+ ions; red lines, the negative ion beam; black lines, equipotential lines.

The lack of electrostatic lens before the accelerator suppose a restriction in the $\frac{V_0}{V_T}$ ratio so that the LE acceleration tube focus the ion beam in the stripper center. The reason for this is explained in the [next section](#). [Jacob \[2001\]](#) calculated that the optimal ratio was $\frac{V_0}{V_T} = 0.102 \simeq 0.1$. This means that, for those radionuclides where a terminal voltage of ~ 500 kV is used (^{10}Be , ^{26}Al and ^{41}Ca), the energy of the negative ions in the LE side should be ~ 50 keV, while for those radionuclides where a terminal voltage of ~ 300 kV is used (^{129}I and actinides), this energy should be 30 keV.

2.3 Tandem accelerators

In a tandem accelerator, the negative ions are attracted to its center (terminal) by a large positive potential $V_T \gg V_0$; the same potential accelerates again the positive ions after the stripping process which takes place in the terminal, by electrostatic repulsion. At each side of the accelerator terminal there is a set of electrodes connected with resistors which avoid a sudden change in the electrostatic potential (acceleration tubes). The potential in these tubes can be supposed to increase linearly if all the resistors of each tube have the same resistance. In this case, the electrostatic force which the negative ions, with a charge $-e$, experience in the first acceleration tube (LE tube) is

$$F_{\text{LE-tube}} = \frac{eV_T}{L_{\text{LE}}}, \quad (2.2)$$

where L_{LE} is the length of the LE tube. The positive ions produced after the stripping process, with a charge $qe : q \in \mathbb{Z}^+$, experience a force in the second acceleration tube (HE tube) of

$$F_{\text{HE-tube}} = \frac{qeV_T}{L_{\text{HE}}}, \quad (2.3)$$

where L_{HE} is the length of the HE tube. In the rest of the zones (before the LE tube, in the terminal and after the HE tube) the potential is constant, so the electrostatic force is 0.

If the negative ions selected in the LE side have a mass M_0 , and the positive atomic ions have a mass of $M \leq M_0$ ¹, the kinetic energy E of the ions is:

- eV_0 at the entrance of the accelerator.

¹ $M = M_0$ if the negative ion was the same atomic species, e.g. $^{14}\text{C}^q$ ions from the stripping of ^{14}C . $M < M_0$ if this positive atomic ion is one of the fragments from a molecular negative ion, e.g. $^{41}\text{Ca}^q$ ions from the stripping of $(^{41}\text{CaF}_3)^-$.

- $e(V_0 + V_T)$ at the exit of the LE tube, this is, in the terminal before the stripping process.
- $\frac{M}{M_0}e(V_0 + V_T)$ at the entrance of the HE tube, this is, in the terminal after the stripping process. This $\frac{M}{M_0}$ factor comes from assuming that the molecular ion breaks elastically, so the velocity of its fragments is the same, distributing the kinetic energy among those fragments proportionally to their masses.
- $\frac{M}{M_0}e(V_0 + V_T) + qV_T$ at the exit of the HE tube.

In each one of these 4 locations, there is a change of the electrostatic force ΔF which has a focusing effect whose optical power $\frac{1}{f}$ is directly proportional to $\frac{\Delta F}{E}$ [Larson, 1974]². If we define the effective charge state of the positive ions as $q^* \equiv \frac{M_0}{M}q$ [Maxeiner, 2016], and taking into account that $V_T \gg V_0$, it can be deduced that the optical power is directly proportional to:

- $\frac{V_T}{V_0} \frac{1}{L_{LE}}$ at the entrance of the LE tube.
- $-\frac{1}{L_{LE}}$ at the exit of the LE tube.
- $q^* \frac{1}{L_{HE}}$ at the entrance of the HE tube.
- $-\frac{q^*}{1+q^*} \frac{1}{L_{HE}}$ at the exit of the HE tube.

The $\frac{V_T}{V_0}$ relationship becomes the key factor in the optical focusing of the negative ions in the terminal, while the effective charge state q^* defines the optical behaviour of the positive ions after the terminal, in the the HE side of the AMS system.

Depending on how the terminal voltage is achieved, there are two main types of particle accelerators used in AMS (not taking into account the HV power supplies used by the MICADAS system):

- The tandetrans: these accelerators use a Cockcroft-Walton circuit based on a RF power supply connected to a series of diodes and capacitors which, after some time, increase the output voltage to a maximum value. In the case a of Figure 2.9 the most basic version of this kind of circuit is shown, but the number of diode-capacitor stages can be increased, being the output voltage directly proportional to the number of stages. The main disadvantage of this kind of accelerator is that only terminal voltages up to 6 MV have been achieved with them. On the other hand, their terminal voltages are very stable and they require little maintenance.

²Even when this approximation to a thin lens is not suitable to get the actual behaviour of a certain accelerator tube, the proportionality can be used to compare the behaviour of different accelerator tubes or different ions.

- The pelletrons: these accelerators use a Van de Graaf generator consisting in a chain of metallic pellets which are charged positively outside the terminal, and deposit this charge on it, increasing the terminal voltage (see the case b of Figure 2.9). The pellets can also be charged negatively before leaving the terminal, so the positive charge deposited by each pellet after passing through doubles. The voltages that some of these accelerators can achieve are even higher than 20 MV. The main disadvantage from the pelletrons is that the use of the pellet chains requires a regular maintenance.

In both cases, the high electric field between the terminal and the accelerator tank (at ground potential) requires the use of a gaseous dielectric material in order to avoid the loss of the voltage by electric discharges. The most common material for this purpose is sulfur hexafluoride (SF_6).

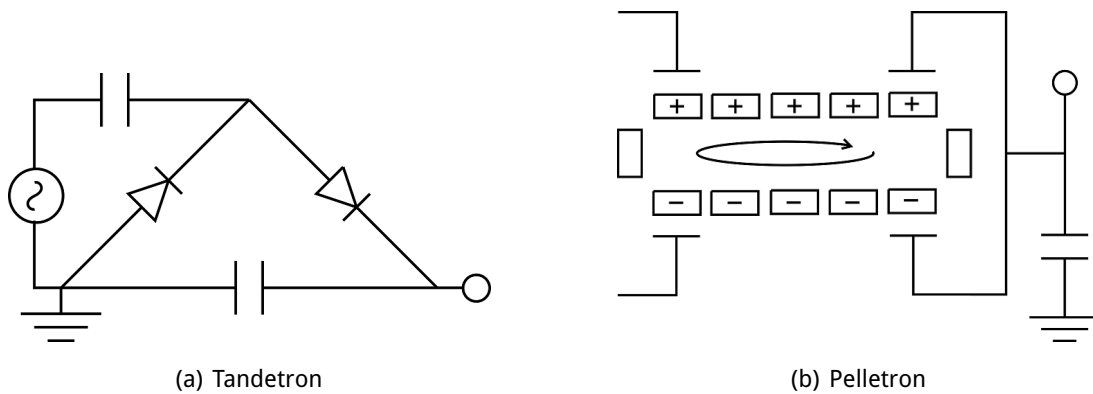


Figure 2.9: Basic operation principle of the systems used by the 2 different types of particle accelerator to get the high terminal voltage.

The stripping process

Several large AMS systems use both solid and gaseous materials as stripper materials. The angular straggling caused by solid strippers is not so important in these systems since this effect is inversely proportional to the kinetic energy. In contrast, compact AMS systems, like the 1 MV AMS system at CNA Seville and the 600 kV AMS system at ETH Zurich, only use gaseous strippers, since the possibility of easily change the mass thickness of the material is critical to destroy the molecular background without severely increasing unwanted angular straggling or scattering effects. With gaseous strippers, the desing of the pumping system of the gas in and out of the stripper tube is extremely important in order to minimize the leakage of the stripper gas to the acceleration tubes (residual gas). This reduces the background

produced by ions with different mass/charge ratio which are scattered by collisions with the residual gas, leading to a trajectory which makes them reach the detector.

The stripping process is caused by the charge exchange reactions between the stripper material and the ions. If the stripper mass thickness is high enough, these charge exchange reactions reach an equilibrium where there are no negative ions, and the positive ions and the atomic species are distributed in several charge states $q \geq 0$. The fraction Φ_q between the number of ions with charge state q produced and the total number of negative ions *stripped*

is called "charge state fraction". It is clear, then, that $\sum_{q=0}^Z \Phi_q = 1$, where Z is the atomic number of the species. The "mean charge state" is, so, defined as $\bar{q} \equiv \sum_{q=0}^Z q\Phi_q$, and depends on

the stripping material, but also on:

- The kinetic energy which the ions have in the terminal $E_{\text{strip}} = \frac{M}{M_0} e(V_0 + V_T)$, also called stripping energy. The higher this energy is, the higher the populated charge states are. The most populated states at low energy AMS systems like SARA and TANDY for most of the radionuclides are typically 1+, 2+ and/or 3+, being $\Phi_q \simeq 0 : \forall q > 3$. This is the minimum charge state reached at large AMS facilities using terminal voltages higher than 2.5 MV. This dependence actually is on the velocity; therefore, for the same stripping energy, two isotopes from the same element have slightly different \bar{q} .
- The atomic species of the ions. The higher the atomic number is, the higher the populated charge states are. At SARA, for instance, the most populated charge state in the He gas stripper for ^{10}Be is 1+, but 2+ for ^{41}Ca and 3+ for ^{236}U .

The stripper transmission for a charge state q is defined as the ratio between the rate of positive ions at this charge state that exit the accelerator and the total rate of negative ions which enter it. Therefore, this transmission is slightly lower than the charge state fraction, because of the optical losses due to the angular straggling introduced by the stripper. It is estimated by measuring the current $-I_0$ of the negative ion from the stable isotope entering the accelerator, and the current I_q from the positive ion of charge state q from stable isotope ion. The transmission, then, is

$$T_q = \frac{I_q}{qI_0}. \quad (2.4)$$

Both systems described in this chapter initially used argon as stripper gas, but changed to helium in the recent years [Vockenhuber et al., 2013; Scognamiglio et al., 2016].

The use of He gas as stripper material means an improvement at low-energy AMS because of the dependence of the mean charge state with the velocity. An example of this can be seen in Figure 2.10, which shows data from Wittkower and Betz [1973] using uranium ions (because of the high mass, velocities are much lower than for other typical ions as carbon for similar energies): while for high energies the mean charge states for other materials are higher than for helium, for low energies the case is the opposite. This makes He gas the best option for AMS at low energies and/or for heavy ion AMS [Vockenhuber et al., 2013; Winkler et al., 2015]. In addition, the angular straggling is reduced because of the low mass of helium.

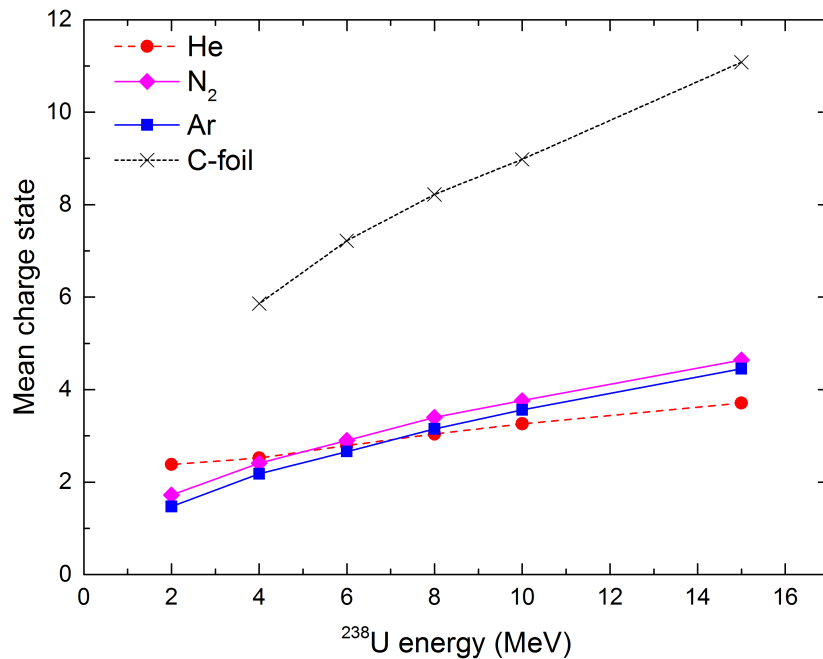


Figure 2.10: Mean charge state of uranium ions as a function of the ion energy for different stripper materials. Data from Wittkower and Betz [1973], presented also in Vockenhuber et al. [2013].

2.3.1 The 1 MV tandetron at SARA

Figure 2.11 shows the scheme of the elements within the 1 MV tandetron used by the SARA system. All the resistors from each of the acceleration tubes are equal, so it can be supposed that inside them there is a constant electric field $\epsilon = \frac{V_T}{L}$, where $L = L_{LE} = L_{HE} = 72.5$ cm. In both cases, the electric field is in direction from the terminal to the accelerator extremes.

At the entrance of the accelerator there is an electrode (Q-Snout), whose potential $V_{Q-Snout} > 0$ can be changed. The Q-Snout lens is used to increase the energy with which the ions enter the LE accelerator tube and, so, reducing the focusing power from the aperture of this tube.

The convergent power of the tube entrance is, in this case, proportional to $\frac{V_T}{V_0 + V_{Q-Snout}}$. Chamizo [2009] calculated that, in order to focus the beam in the center of the stripper tube, this voltage has to be

$$V_{Q-Snout} = 0.082 \cdot V_T - V_0. \quad (2.5)$$

In the stripper tube, the gas pressure is measured only at its center (p_0). In order to calculate the stripper mass thickness, it is assumed that the gas pressure follows a triangular distribution, so the average pressure would be $\frac{p_0}{2}$, and the mass thickness,

$$\rho_A = \frac{M_{\text{gas}} L p_0}{RT} \frac{1}{2}, \quad (2.6)$$

where M_{gas} is the molar mass of the stripper gas, L the length of the stripper tube (30 cm for SARA), $R = 83145 \text{ mbar} \cdot \text{cm}^3 \cdot \text{K}^{-1} \cdot \text{mol}^{-1}$, and T the gas temperature, which is at a room temperature of 294.15 K (21 °C).

Since the focusing power of the entrance of the HE accelerator tube is proportional to $q^* \equiv \frac{M_0}{M} q$, a quadrupole triplet (Q-Pole) is placed at the exit of the accelerator to refocus the beam. An electrostatic quadrupole is a set of four electrodes, two of them facing in the X direction and connected to a potential V_Q , and the other two facing in the Y direction and connected to a potential $-V_Q$ (see Figure 2.12). The electrodes have a geometry so that the potential ϕ in places close to the center is approximately parabolic, this is, $\phi \propto (x^2 - y^2)$ (so it follows the Laplace equation $\Delta\phi = 0$).

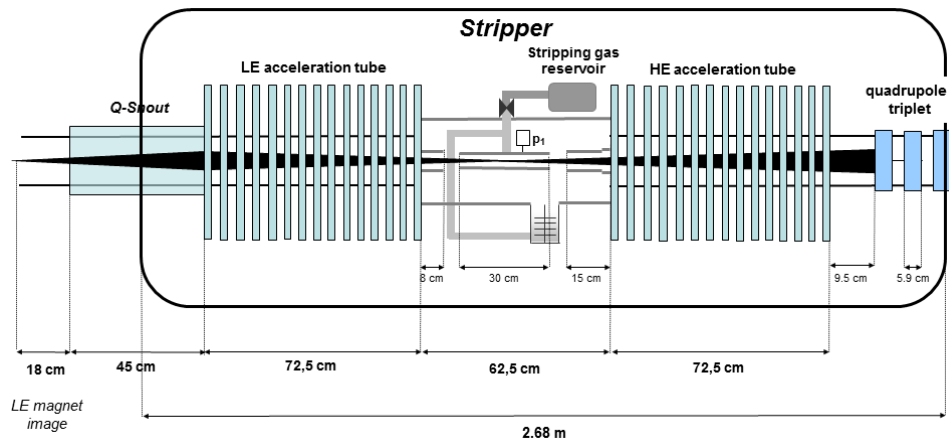


Figure 2.11: Scheme of the system of the 1 MV accelerator from SARA. Picture from Chamizo [2009], modified by Scognamiglio [2017].

Since each quadrupole focuses the beam in one axis, but unfocuses it in the other, sets of multiple quadrupoles (multiplet) are used, where each quadrupole uses the opposite potentials as the previous one. In the case of the quadrupole triplet at SARA, the potentials are, for a $V_Q > 0$:

- V_Q in the X axis for the central quadrupole, and in the Y axis for the first and third quadrupoles.
- $-V_Q$ in the Y axis for the central quadrupole, and in the X axis for the first and third quadrupoles.

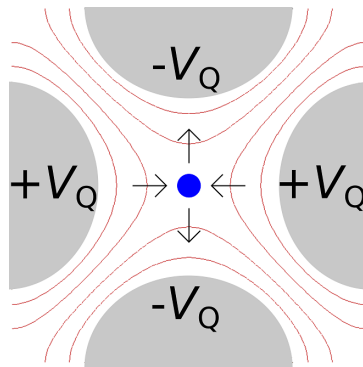


Figure 2.12: SIMION® view of an electrostatic quadrupole. The arrows represent the electrostatic force which a positively charged particle would experienced for a $V_Q > 0$.

2.3.2 The 600 kV pelletron at TANDY

TANDY uses a 600 kV pelletron from [NEC](#), which has only one charging pellet chain, shown in [Figure 2.13](#). All the resistors of the [HE](#) tube are equal, so it can be assumed that there is a constant electric field $\epsilon_{HE} = \frac{V_T}{L}$, where $L = L_{LE} = L_{HE} = 28$ cm is the length of each one of the acceleration tube. The resistors of the [LE](#), instead, have a resistance in the first third part of the acceleration tube, but $\frac{3}{2}$ times that resistance in the rest [[Jacob, 2001](#)], leading to two different electric fields: a field $\epsilon_1 = \frac{3}{4} \frac{V_T}{L}$ in the first third part, and a field $\epsilon_2 = \frac{3}{2} \epsilon_1 = \frac{9}{8} \frac{V_T}{L}$ in the other two third parts, so $\epsilon_1 \frac{L}{3} + \epsilon_2 \frac{2L}{3} = V_T$.

Thanks to this lower electric field at the entrance of the [LE](#) tube, the optimal $\frac{V_0}{V_T}$ ratio to focus the beam in the center of the stripper can be achieved with the energies available with the ion source even for terminal voltages of 500 kV³. The electric field difference after this first

³If the electric field were $\epsilon = \frac{V_T}{L} = \frac{4}{3} \epsilon_1$, the optimal $\frac{V_0}{V_T}$ would be also higher in order to have the same optical power.

third part of the tube also has a focusing effect, but this is much lower than the one at the entrance because of the higher energy of the ions in that place.

In this case, the stripper gas pressure is measured not only in the center, but also in the stripper apertures. Together with simulations, this allows a more accurate estimation of the stripper mass thickness. Nevertheless, the simulation on [Jacob et al. \[2000\]](#), for instance, estimates an Ar mass thickness of $2 \mu\text{g}\cdot\text{cm}^{-2}$ for a central pressure of 0.058 mbar, whereas using [Equation 2.6](#), a mass thickness of $2.04 \mu\text{g}\cdot\text{cm}^{-2}$ is estimated, showing the agreement of the triangular approximation with more accurate estimations.

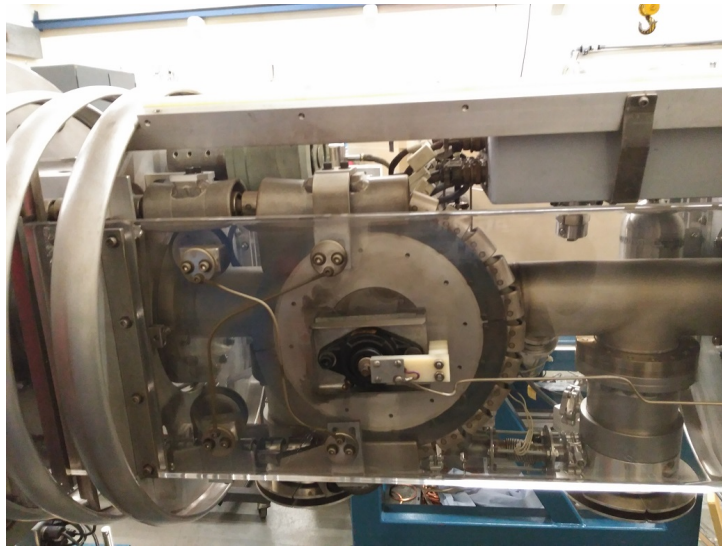


Figure 2.13: Pellet chain used to transport the charge in the pelletron from TANDY.

2.4 Electromagnetic kinematic filters

The kinematic filters most commonly used by [AMS](#) systems to select only the ions with a certain mass/charge ratio are:

- Magnetic dipoles, which use a magnetic force to select the product of both the mass/charge ratio and the energy/charge ratio ($\frac{EM}{q^2}$).
- Electrostatic analyzers, which use an electrostatic force to select the energy/charge ratio ($\frac{E}{q}$).
- Wien filters, which confront two forces (an electrostatic one and a magnetic one) to select the velocity of the ions ($v \propto \sqrt{\frac{E}{M}}$).

The AMS systems described in this thesis use only magnetic dipoles and electrostatic analyzers. Magnetic dipoles are always used in both, the LE side and the HE side.

A common characteristic of these elements is that ions with both the same mass/charge and energy/mass ratio have the same behavior. In order to distinguish the radionuclide of interest from other ions reaching the detector, it has to be able to measure the kinetic energy of these.

Magnetic dipoles

A magnetic dipole is an electromagnet which generate a magnetic field \vec{B} in a specific area. For ions with a charge qe which are moving with a linear momentum \vec{p} perpendicular to \vec{B} , the magnetic force will make these ions follow a curved trajectory, also perpendicular to \vec{B} , with a radius

$$\rho = \frac{p}{qeB}. \quad (2.7)$$

If the trajectory of these non-relativistic ions of mass m ($p = \sqrt{2Em}$) must have a radius $\rho = R$ in order to exit the magnet and continue its trajectory through the system, the product of the mass/charge ratio and the energy/charge ratio must be

$$\frac{Em}{q^2e^2} = \frac{B^2R^2}{2}. \quad (2.8)$$

In an AMS system, mass selection is needed before (LE side) and after (HE side) the ion acceleration in the tandem accelerator. Taking into account the ion kinetic energy and charge state in each of the sides, the mass selected by the LE side magnet (LEM) will be

$$M_0 = \frac{eB_{LEM}^2R_{LEM}^2}{2V_0}, \quad (2.9)$$

while the mass/charge ratio selected by the HE side magnet (HEM) must satisfy that

$$\frac{M}{q} \left(\frac{V_0 + V_T}{M_0} \frac{M}{q} + V_T \right) = \frac{eB_{HEM}^2R_{HEM}^2}{2}. \quad (2.10)$$

It can be demonstrated that this relationship between B_{HEM} and $\frac{M}{q}$ is bijective so, theoretically, for a constant B_{HEM} , the use of the HEM would be enough to select the required mass/charge ratio. However, some energy dispersion or charge exchange processes with the

residual gas in the HE accelerator tube could make some ions with different mass/charge ratio have the same $\frac{EM}{q^2}$ relationship. That is the reason that, for the sensitivities required in AMS measurements, an additional filter, like the electrostatic analyzer, must be used in the HE side.

Magnetic dipoles also play an optical role. This ion focusing effect depends on the angle between the beam and the borders of the magnet [Wollnik, 1999] (see Figure 2.14). If the entrance and the exit of the magnet are perpendicular to the beam direction (Z axis), ions diverging in the X axis (perpendicular to the beam but parallel to its curvature radius) from a point (object) before the magnet will converge in a point (image) that is lined up with both the object and the center of curvature of the ion beam. Ions diverging in the Y axis (perpendicular to both the beam and its curvature radius), nevertheless, would not be focused (see Figure 2.15) since Lorentz force, perpendicular to both the magnetic field (in the Y direction) and the ion direction, would be in the X direction. Even in the borders, where the magnetic field has a little component perpendicular to them, the magnetic force would still remain in the X direction.

If the borders are not perpendicular to the Z axis, this component perpendicular to the borders do has a focusing effect in the Y direction, since the magnetic field in them would now have components in the 3 axis [Wollnik, 1999]. This convergent power from each border is, approximately,

$$\frac{1}{f_y} = \frac{\tan \varepsilon}{R}, \quad (2.11)$$

where ε is the angle which the border is inclined respect to the plane normal to the beam,

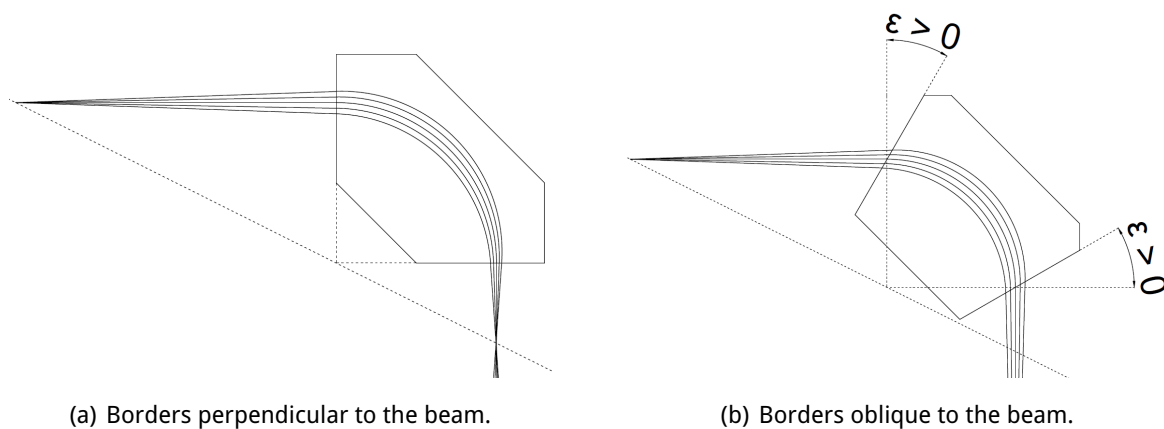


Figure 2.14: Focusing in the X axis of magnetic dipoles depending on the inclination of the borders.

and R the bending radius of the magnet. At the entrance, $\varepsilon > 0$ is defined if the border is rotated in the same direction as the ions; at the exit, if it is rotated in the opposite direction (see case b of [Figure 2.14](#)).

That is the reason that magnetic dipoles used in AMS typically have this kind of borders. This change of the geometry of the magnet also has a divergent power $\frac{1}{f_x} = -\frac{1}{f_y}$ in the X axis from the borders that has to be taken into account.

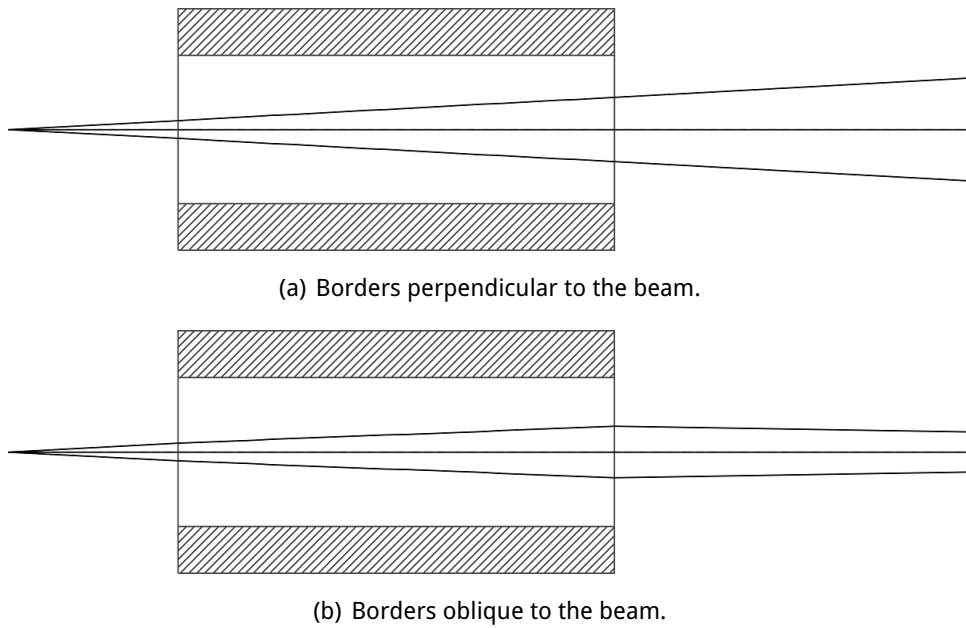


Figure 2.15: Focusing in the Y axis of magnetic dipoles depending on the inclination of the borders. Simulation performed with GICOSY [[Weick, n.d.](#)].

Electrostatic analyzers

In order to reject ions with the same $\frac{EM}{q^2}$ relationship but different $\frac{M}{q}$ than the radionuclide of interest, an electrostatic analyzer (ESA) can be used to select the $\frac{E}{q}$ ratio. Basically, an ESA consists of a pair of electrodes at different voltages, so that the resulting electric field ϵ , perpendicular to the beam direction, causes a curved trajectory with a radius

$$\rho = \frac{2E}{qe\epsilon}. \quad (2.12)$$

There exist different types of ESA depending on the geometry of the electrodes, but the most used in AMS are spherical, like the one shown in [Figure 2.16](#). This way, the ESA has the same

focusing effect in both the X and the Y axes. This effect is equivalent to the one given in the X axis by a magnetic dipole with borders perpendicular to the beam.

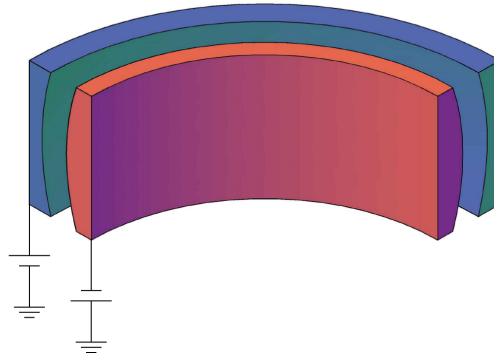


Figure 2.16: Scheme of an ESA with spherical geometry. In this case, the selected ions should have positive charge.

LE injector

The set of kinematic filters used to select the mass of the negative ion entering the accelerator is also called LE injector. The most basic way of doing this selection is just with a magnetic dipole, as it is done at SARA and TANDY.

A common feature in the LEM of any AMS facility is the *fast switching* bouncer. In AMS, not only the radionuclide of interest must be detected, but also the current of a reference stable isotope is measured to get the ratio between both. For instance, in the case of ^{41}Ca AMS, $^{40}\text{Ca}^q$ currents are measured to get the $^{41}\text{Ca}/^{40}\text{Ca}$ ratios. This requires that the stable isotope is sequentially injected in the accelerator. Changing the magnetic field of the LEM in order to do so is not operative because the magnetic hysteresis would make this switching too slow. Therefore, the stable isotope ions (of mass M'_0) are temporarily accelerated or decelerated inside the magnet changing a voltage (bouncer) $V_{\text{bouncer}} \lesseqgtr 0$ connected to it, so the EM product is the same as for the radionuclide of interest with its bouncer voltage, this is,

$$(V_0 + V_{\text{bouncer}})M'_0 = V_0M_0 : V_{\text{bouncer}} = \frac{M_0 - M'_0}{M'_0}V_0. \quad (2.13)$$

The main difference between the LE injectors of SARA and TANDY is that, at TANDY, there is a Faraday cup placed out of beam line after the LEM in order to measure the currents of the negative ions during measurements. This way, the stripper transmission can be tracked, which cannot be made at SARA.

HE spectrometer

Both SARA and TANDY use a combination of a HEM and an ESA to select the mass/charge ratio of the ions reaching the detector. An interesting property of the combination of both, a magnetic dipole and an ESA, is that they can be placed in a way that, for a certain object position, the properties of the final image depend only on the $\frac{M}{q}$ ratio, and not in the energy (achromatic system). This way, for ions with the same mass, little dispersions on the energy would not lead to optical losses, effect which is depicted in Figure 2.17. For ions of different mass, these little dispersions would not lead to part of these ions entering the detector and interfering with the measurement. Consequently, achromaticity is a considerably desired feature in the HE sector at AMS. Some systems even have a LE ESA to perform an achromatic injection of the negative ions.

When the LEM is injecting the stable isotope, its different bending radius in the HEM avoid this ion reaching the ESA. In order to measure its current, a Faraday cup (FC) is placed on its path. This way, the detector placed after the ESA measure the radionuclide ion rates, and the FC, the current from its stable isotope, which permits the calculation of the isotopic ratio between both. This ratio must be corrected taking into account

- a) the slightly different transmission in the stripper (different masses mean different velocities for similar kinetic energies),

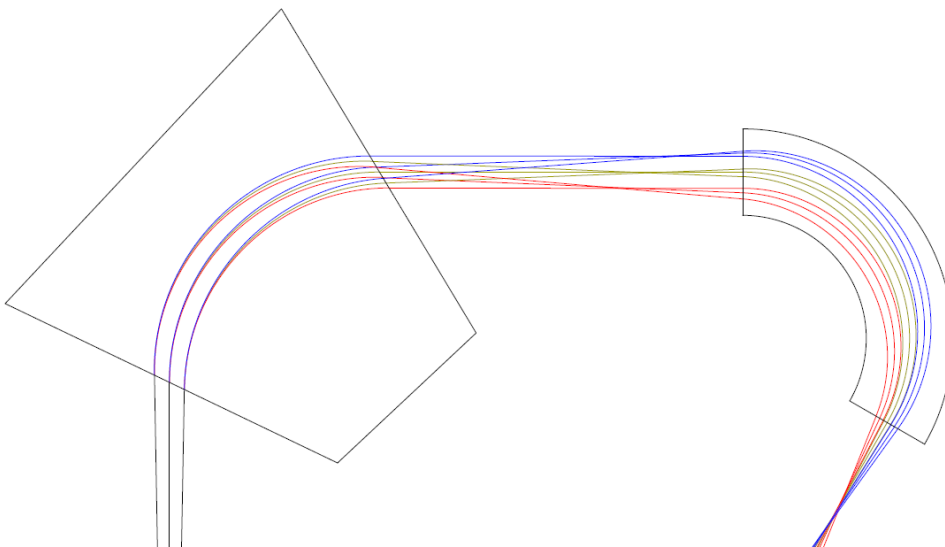


Figure 2.17: Behaviour of different ions with the same mass but different energy in an achromatic system. The different colours represent different ion energies, from lowest to highest: red, yellow and blue.

- b) the ion optical losses for the radionuclide from the accelerator to the detector,
- c) the background.

The need of these corrections is the reason why blank samples, with no content of the radionuclide, and standards, with known isotopic ratios between the radionuclide and its stable isotope, are also measured.

Both systems SARA and TANDY also present and insertable silicon nitride foil between the HEM and the ESA which is used to reduce the ^{10}B rates reaching the detector on ^{10}Be measurements. Because of its different energy loss in the foil, most of the ^{10}B will not be selected by the ESA.

2.4.1 The optical properties of the HE side at SARA

The use of the Q-Pole allows the focusing of the beam so that the object of the HE side, the HEM and the ESA form an achromatic system, independently of the effective charge state of the ions. In Figure 2.18, a simulation of $^{41}\text{Ca}^{2+}$ ions in the HE side of SARA, performed with GICOSY [Weick, n.d.], is presented. As it can be seen, all the ions converge in the same point, independently of their energy.

Between the HEM and the ESA there are two different Faraday cups: a fixed one (FC2) which was used to measure the ^{12}C currents in ^{14}C measurements (now these are performed with the MICADAS system at CNA); and a movable one (FC3) used to measure the currents of the stable isotope for the rest of AMS radionuclides. The FC3 has a hole to allow the $^{129}\text{I}^q$ ions to pass to the ESA while the FC measure the $^{127}\text{I}^q$ current in ^{129}I measurements (see Figure 2.19).

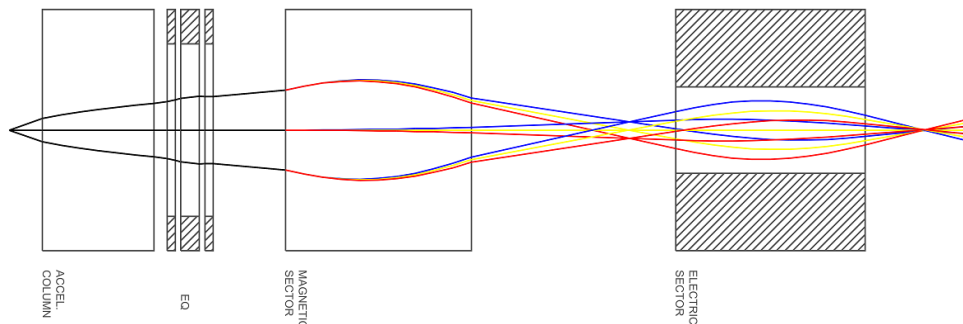


Figure 2.18: GICOSY simulation of $^{41}\text{Ca}^{2+}$ ions in the HE side of SARA (X-axis). The different colors represent different ion energies.

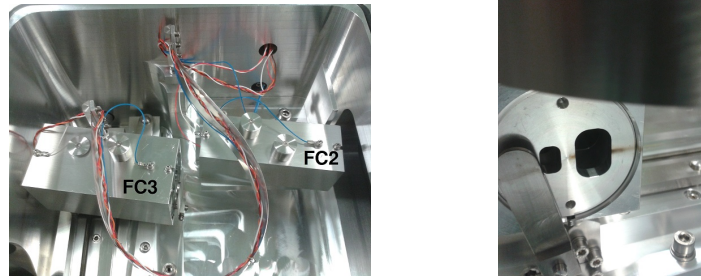


Figure 2.19: Faraday cups used in AMS measurements with SARA. On the left, an upper view of both faraday cups is shown; on the right, a frontal view of the FC3.

2.4.2 The optical properties of the HE side at TANDY

Since there is no additional focusing between the accelerator and the HEM, the optical properties of the HE side of TANDY depend on the effective charge state $q^* \equiv \frac{M_0}{M} q$. The combination of the HEM and the ESA forms an achromatic system only for $q^* = 1+$. $^{41}\text{Ca}^{2+}$ ions, on the other hand, have an effective charge state of 4.78 ± 0.22 when the $(^{41}\text{CaF}_3)^-$ negative ion, with a mass of 98 u, is selected in the LE side. The chromatic behaviour of these ions, simulated with GICOSY, is shown in Figure 2.20.

Between the HEM and the ESA there are 3 different Faraday Cups used to measure the stable isotopes: one for ^9Be , one for ^{40}Ca and ^{127}I , and another one for ^{27}Al and ^{238}U .

The optical properties of the HEM 2 (not used in ^{41}Ca measurements) are explained in detail in Müller et al. [2010].

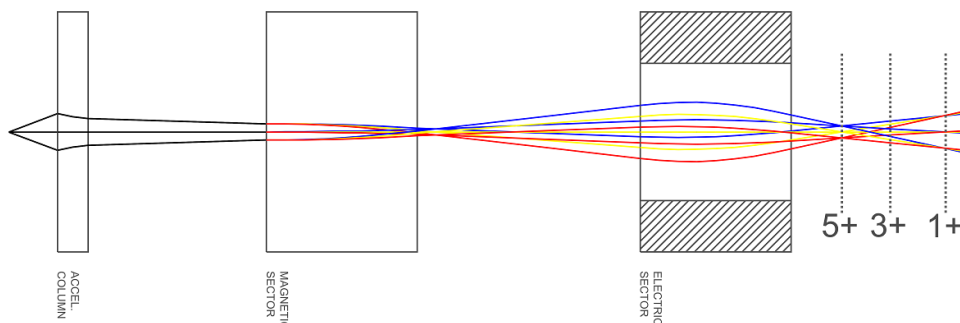


Figure 2.20: GICOSY simulation of $^{41}\text{Ca}^{2+}$ ions in the HE side of TANDY (X-axis). The different colors represent different ion energies. The position of the images from the charge states 1+, 3+ and 5+ are also shown.

2.5 Gas ionization chambers

In order to distinguish the ions with different mass M' and charge q' but the same mass/charge ratio as the radionuclide of interest, the detection system has to include the measurement of the energy of these ions. Since, as it was shown, these ions also have the same $\frac{E}{q}$ ratio, their energy will be $E' = \frac{q'}{q} E$.

Nowadays, the most common kind of detectors used in AMS are the gas ionization chambers (GIC). A scheme of the operation principle of this kind of detectors is shown in Figure 2.21. The GIC basically consists of a chamber filled with a gas, such as isobutane, and with two electrodes placed face to face, one connected to a positive potential (anode) and another one connected to a negative potential (cathode). The electric field caused by this potential difference is low enough to have no effect on the ions because of their relatively high energy. When an energetic charged particle enters the GIC, it is slowed down by the electrons from the gas, which is ionized. The electrons released in this ionization, whose number is directly proportional to the energy lost by the charged particle, are driven by the electric field to the anode. The signal caused can be electronically treated in order to get a final digital signal which depends on the energy lost by the ion inside the chamber. If the gas pressure is high enough so that the ions are stopped before reaching the end of the chamber, the signal will be directly proportional to the particle energy before entering the chamber. The Frisch grid makes the shape of the signal independent from the place where the ionization took place.

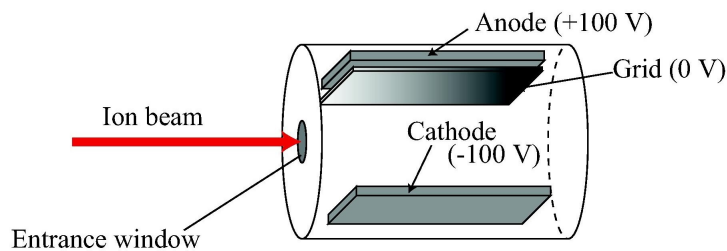


Figure 2.21: Scheme of the operation principle of a GIC. Picture from Hosoya et al. [2017].

This energy is not exactly the ion energy before reaching the whole detector system. In order to deal with the pressure difference between the chamber and the AMS system (in vacuum), a thin foil (window) is placed at the entrance of the chamber. The ion will lose some energy in that window, producing also a straggling on the energy with which it enters the chamber. This effect is reduced if silicon nitride foils are used as detector windows, thanks to the availability of foils of this material with a well defined thickness lower than 100 nm [Döbeli et al., 2004].

The energy loss per length unit $-\frac{dE}{dx}$ (stopping power) in the detector gas depends on the atomic number of the ion, but also on its energy. For energies higher than the so-called Bragg

peak energy (27.5 MeV for ^{41}Ca in butane, according to SRIM), this stopping power is $\propto \frac{Z_p^2 \cdot Z_t}{E}$ (Bethe-Bloch formula), where Z_p and Z_t are the atomic numbers of the ion (projectile) and the counting gas (target), respectively. For lower energies, as those reached at SARA and TANDY for ^{41}Ca (one order of magnitude lower) the stopping power becomes $\propto \frac{Z_p \cdot Z_t}{(Z_p^{2/3} + Z_t^{2/3})^{3/2}} \sqrt{E}$ (LSS formula).

In both cases, the higher the atomic number of the projectile, the higher this stopping power is⁴. This can be useful to distinguish the radionuclide of interest from its stable isobar. For instance, in Figure 2.22 it can be seen the different dependence of the stopping power with the distance covered by the ion for ^{41}Ca and ^{41}K . Sectioning the GIC anode in different ones, therefore, the signals from both isobars can be distinguished. If the gas ionization chamber has two or more anodes, the energy deposited on each one of them by the stable isobar ion will be different that the one deposited by the radionuclide of interest. The total energy deposited in both anodes will still be the same for both ions. An example of this separation with ^{41}Ca and ^{41}K ions with an energy of 27 MeV can be seen in Figure 2.23.

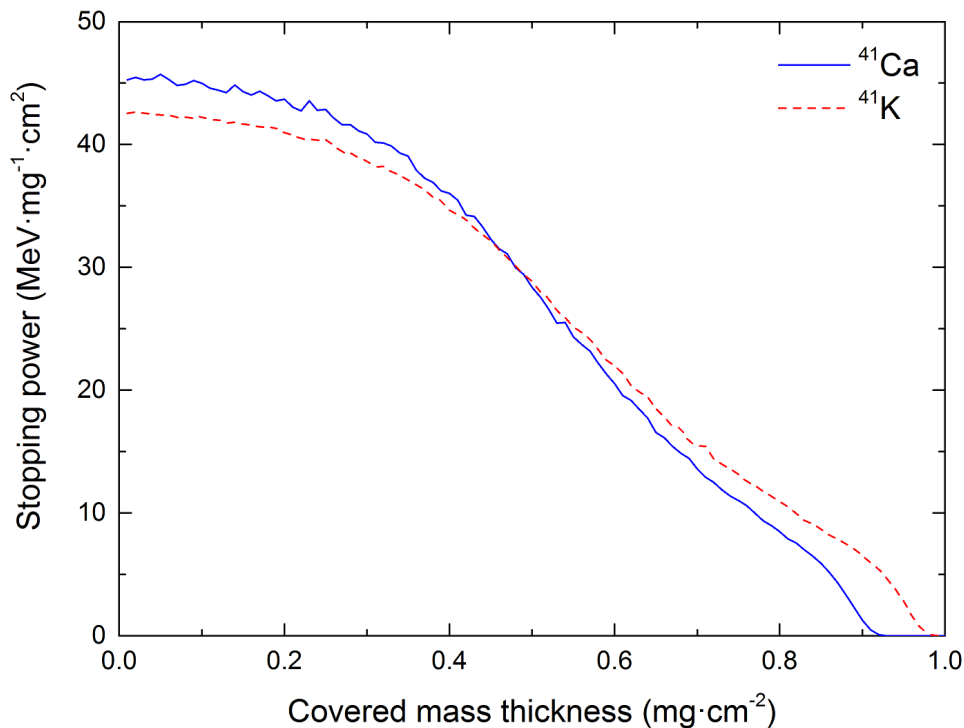


Figure 2.22: Stopping power of ^{41}Ca and ^{41}K ions with an energy of 26.5 MeV in butane according to SRIM. The butane density was set to stop the ^{41}Ca ions before covering a distance of 500 mm.

⁴Even when this is not so trivial for the LSS formula, it can be easily proven that the function $f(Z) = \frac{Z}{(Z^{2/3} + x)^{3/2}}$ fulfills that $\frac{df}{dZ} > 0$.

At low energies, though, the high angular and energy loss straggling within the counting gas leads to a higher energy straggling of the signals from the different anodes, and the distinction between ^{41}Ca and ^{41}K is not possible (see [chapter 3](#)). For heavier ions, the transmission of the kinetic energy to the whole gas atom/molecule (nuclear stopping power) becomes important at low energies.

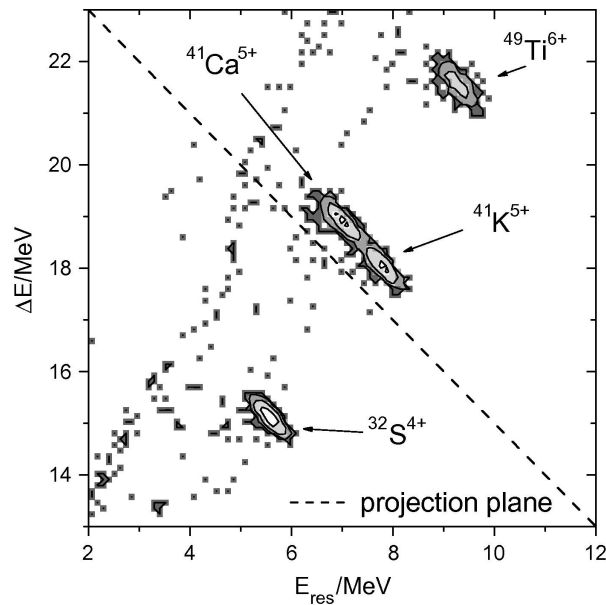


Figure 2.23: Detector signals in a ^{41}Ca measurement with the 5 MV AMS system at SUERC, Glasgow. Picture from [Schulze-König et al. \[2010\]](#).

2.5.1 The compact gas ionization chamber at SARA

The compact GIC at SARA, which is presented in Figure 2.24, was designed at the ETH LIP, and it is located after the ESA. It has two anodes, each one of them 5 cm long. Comparing with the old HVE detector (see Figure 2.25), the lower volume of the compact GIC reduce the electronic noise and the design minimizes the non-active area.

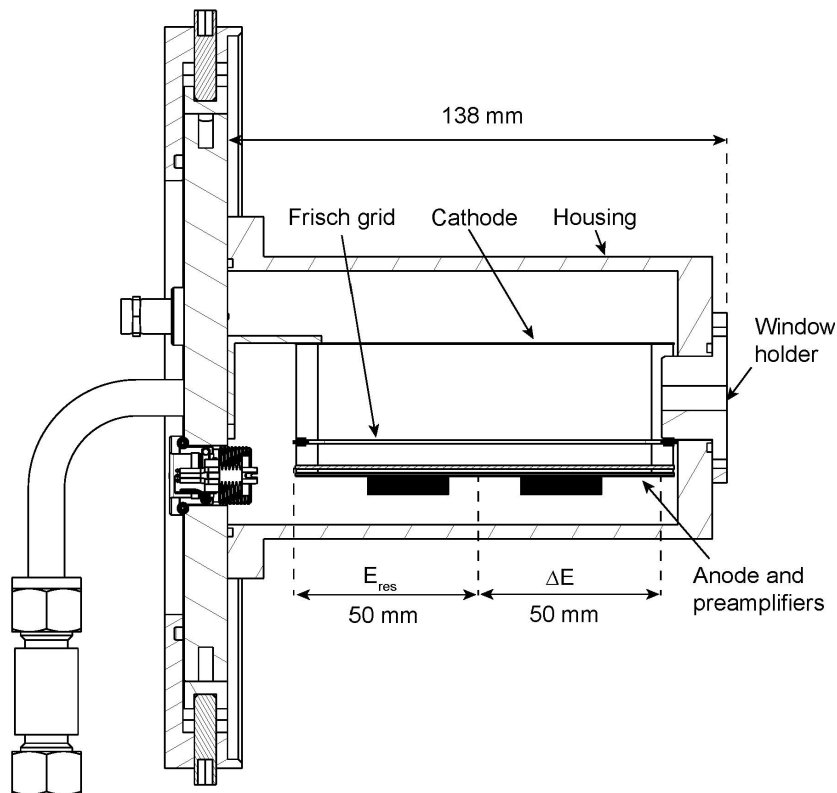


Figure 2.24: Scheme of the compact GIC at SARA. Picture from Scognamiglio et al. [2016].

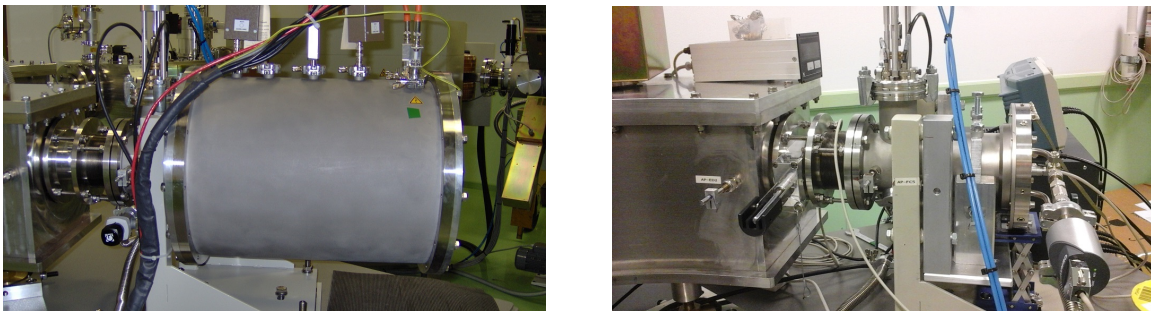


Figure 2.25: Comparison between the old HVE GIC (left), and the new compact GIC (right).

2.5.2 The retractable gas ionization chamber at TANDY

The retractable GIC at TANDY (see Figure 2.26) can be inserted after the ESA, in the image of the 3+ charge state. It has two anodes, 3 cm long each one. For other radionuclides, a compact GIC similar to the one at SARA placed after the HEM 2 is used [Müller et al., 2012].

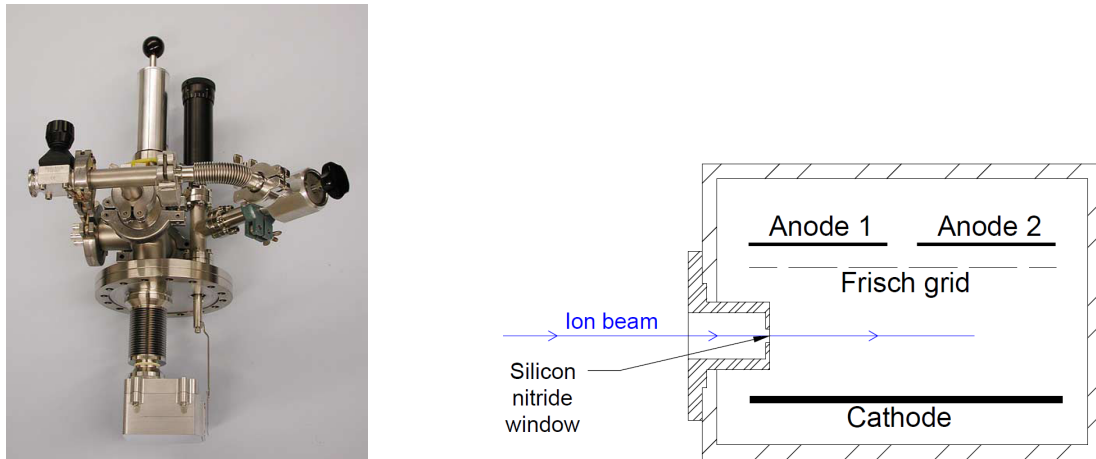


Figure 2.26: Picture (left) and scheme (right) of the retractable GIC used in the ^{41}Ca measurements with TANDY. Picture from Stocker et al. [2005]. Scheme adapted from a figure presented on Stocker [2006].

Chapter 3

^{41}Ca AMS at low energies

In this chapter, the main challenges related to ^{41}Ca AMS at low energies are detailed, and some experiments related to this performed during this thesis with both systems, SARA and TANDY, are also presented. The most important results were also published in [Vivo-Vilches et al. \[in press\]](#).

3.1 The ^{41}K interference

Kinematic filters commonly used at AMS only select ions with a certain mass/charge ratio. Nevertheless, the measurement of the energy of the ions in the detector allows the discrimination of ions with different mass but the same M/q . Therefore, the main challenge of ^{41}Ca AMS measurements is dealing with its stable isobar, ^{41}K . As it is stated in [chapter 1](#), large AMS facilities deal with this potential interference using the different stopping power in the gas of the GIC [[Hosoya et al., 2017](#)]. At low energies, on the other hand, scattering processes with the gas itself produce an important angular straggling. This straggling, together with the one on the energy loss itself, also entails a lower energy resolution, since different trajectories lead to different energy losses in each one of the anodes.

[Figure 3.1](#), for instance, shows a simulation performed with SRIM [[Ziegler, n.d.](#)] of the behaviour of ^{41}Ca ions in a GIC with 2 anodes: scattered ions will cover a longer path in the first half of the detector, leaving more energy in the first anode. This way, at lower energies, ^{41}K ions scattered an angle θ_{K} could leave more energy in the first anode than some ^{41}Ca ions scattered and angle $\theta_{\text{Ca}} < \theta_{\text{K}}$, even when the stopping power of the potassium ions is lower.

The simulated spectra corresponding to ^{41}Ca and ^{41}K ions at different energies in a 2-anode

GIC detector like the one presented in Figure 3.1 are presented in Figure 3.2. At relatively high energies, the spectrum shows 2 count areas: ^{41}K ions deposit less energy than ^{41}Ca ions in the first anode (ΔE) and more energy in the second one (E_{res}). At lower energies, like those reached with the 1 MV AMS system at CNA, the ^{41}K and ^{41}Ca counts are mixed in the spectrum.

The higher relative energy and angular straggling at low energies also avoids the use of tech-

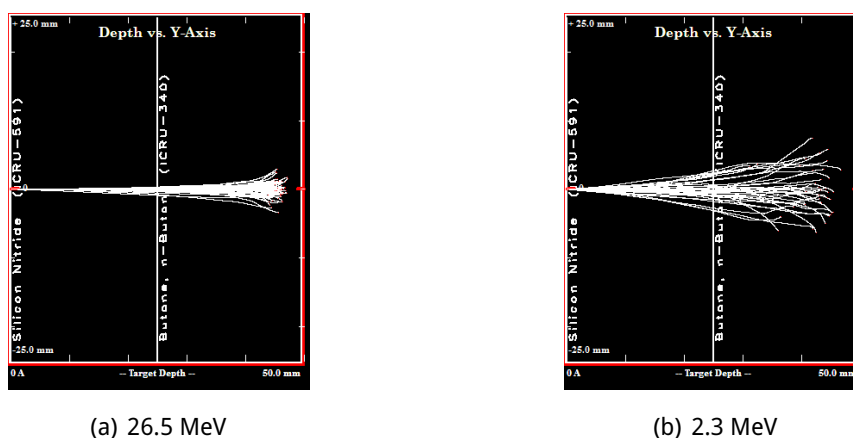


Figure 3.1: SRIM simulation of the trajectories of several ^{41}Ca ions at two different energies in a GIC detector with a 50 nm silicon nitride window, filled with isobutane and with 2 anodes 2.5 cm long each. Isobutane pressures were adjusted on each case to stop the ions just before the GIC end.

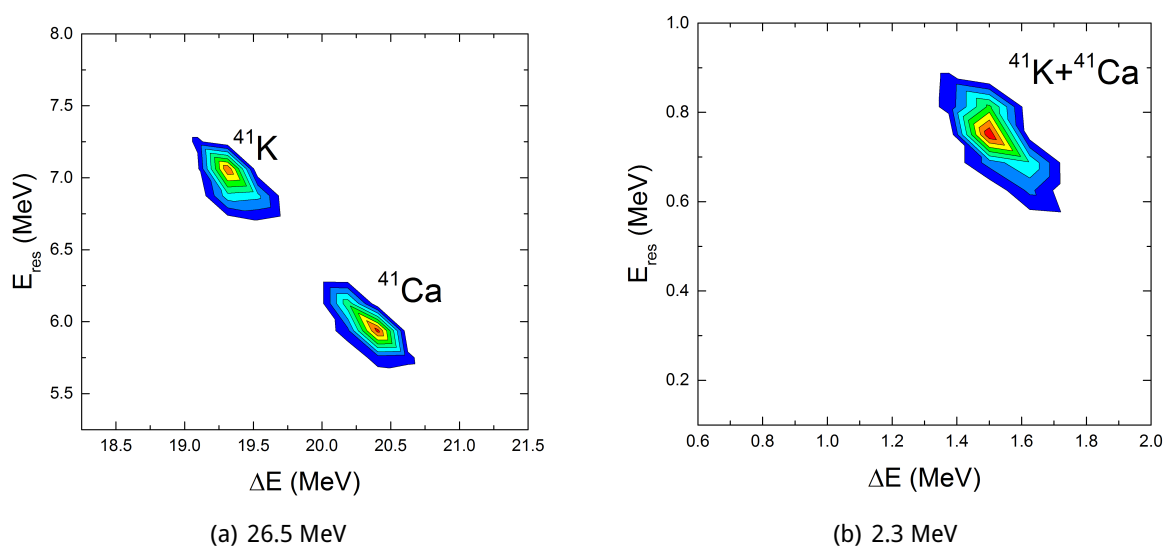


Figure 3.2: Spectra simulation with SRIM of an equal number of counts of ^{41}Ca and ^{41}K at different energies. The ΔE axis represents the energy deposited in the first anode; the E_{res} axis, the energy deposited in the second one.

niques based on the different energy loss on silicon nitride foils, such as the ΔTOF technique [Vockenhuber et al., 2005]. As it can be seen in Table 3.1, the energy straggling introduced by these foils in ^{41}K and ^{41}Ca ions with an energy of 3.4 MeV ($^{41}\text{Ca}^{3+}$ for a terminal voltage of 1 MV) would be, in most of the cases, higher, than the difference on the energy loss. Even at the very best, this difference is only slightly higher than the energy loss straggling. For thicker foils, besides, there would be an additional contribution to the energy straggling because of the angular one.

The use of CaH_2 , selecting the $(\text{CaH}_3)^-$ ion in the LE side, would reduce this potassium interference because of the instability of the $(\text{KH}_3)^-$ ion. This only leaves the minor contribution to the ^{41}K interference of the $(^{41}\text{KH}_2)^-$ ions where one of the hydrogen atoms is a deuterium one. However, because of the hygroscopic character of CaH_2 , its chemical preparation and handling is problematic. This makes this chemical form not suitable for applications which involve large number of samples, like those typically performed with low energy AMS. The possibility of extracting the $(\text{CaH}_3)^-$ ion from other matrices, like the mix of calcium salts with titanium hydride, have been tested in the past [Fink et al., 1990; Baba et al., 1997], and recently here at CNA, in the last year of this thesis. Unfortunately, only unstable currents of few nA of $(^{40}\text{CaH}_3)^-$ were measured in all these cases. More information about these experiments is provided in Appendix B.

Therefore, at SARA and TANDY, CaF_2 samples, extracting the $(\text{CaF}_3)^-$ ion in the LE side, are used, as it is also done in most of the large AMS facilities. The stability of this compound makes it very suitable for handling of a large number of samples. The negative point, is that the ^{41}K interference is increased by 2 orders of magnitude [Fink et al., 1990], this is, typically in the 10^{-11} level. Nevertheless, most of the samples measured with these systems present $^{41}\text{Ca}/^{40}\text{Ca}$ ratios higher than 10^{-10} . First ^{41}Ca measurements at TANDY were performed treating this interference as part of the background [Schulze-König et al., 2010]. However, since the relative content of potassium could differ from one sample to another, an estimation of

Table 3.1: Energy loss straggling and average energy difference with ^{41}K ions of 3.4 MeV ^{41}Ca ions after a silicon nitride window as a function of the foil thickness. The energy straggling (full width at half maximum of the Gaussian distribution) has been calculated with the semi-empirical Sun's formula [Sun et al., 2007; Müller, 2009]. Average energies after the foil were obtained from SRIM simulations.

Foil thickness (nm)	^{41}K - ^{41}Ca energy difference (keV)	Energy loss straggling (keV)
50	11	23
100	30	32
250	70	51

the ⁴¹K interference would be more suitable. The best way to estimate this interference is the measurement of the other stable isotope of potassium, the ³⁹K [Vockenhuber et al., 2015].

Potassium has 2 stable isotopes: ³⁹K, with a natural isotopic abundance of 93.2581%; and ⁴¹K, with a natural isotopic abundance of 6.7302% [National Nuclear Data Center, n.d.]. Apart from slight variations, these isotopic abundance are always the same, independently from the sample, so the ⁴¹K/³⁹K ratio should be 0.072167 in any material. Therefore, since the ⁴¹K/⁴⁰Ca interference is typically in the 10⁻¹¹-10⁻¹⁰ range, ³⁹K/⁴⁰Ca ratios are in the level of 10⁻¹⁰-10⁻⁹, ratios very suitable to be measured by AMS. Consequently, measuring not only ⁴¹M/⁴⁰Ca¹, but also ³⁹K/⁴⁰Ca ratios, the actual ⁴¹Ca/⁴⁰Ca ratio could be calculated as

$$\mathcal{R}_{41,K\text{-corr}} = \mathcal{R}_{41} - \alpha \mathcal{R}_{39}, \quad (3.1)$$

where \mathcal{R}_{41} denotes the uncorrected ⁴¹M/⁴⁰Ca ratio; \mathcal{R}_{39} , the ³⁹K/⁴⁰Ca ratio; and α , the measured ⁴¹K/³⁹K ratio. Slight differences on the stripper and optical transmission between both potassium isotopes would make α not being exactly the natural ⁴¹K/³⁹K ratio. This experimental ⁴¹K/³⁹K ratio (K-correction factor) can be calculated performing a linear regression where the values of the dependent variable x_i are the ³⁹K/⁴⁰Ca ratios from different measurements of the blank samples, and those of the independent variable y_i , the ⁴¹M/⁴⁰Ca ratios. The experimental ⁴¹K/³⁹K ratio, α , is the slope of this linear regression. More information about the related data analysis is presented in section 3.4.

In order to sequentially inject ⁴¹M and ³⁹K ions into the detector, avoiding changes in the magnetic field of the HEM, the accelerator terminal and ESA voltages have to be changed sequentially, as it is done in actinide measurements [Chamizo et al., 2008a; Fifield, 2008]. The terminal voltage to inject the ³⁹K^q ions should make its energy $\frac{41}{39}$ times that one of the ⁴¹M^q ions when these are injected. However, this switching has to be much slower than the one typically used to inject the negative ions into the accelerator, because of both: the need of counting times of several seconds for both ions, and the relatively slow change of the terminal voltage.

The most populated states at the stripping energies achieved with these compact AMS systems are the 2+ and 3+ states. Using the latter, there is no need of using relatively high stripper pressures in order to destroy the molecular background, since molecular ions with charge state 3+ are unstable. Up until 2018, it was thought that the K-correction would not allow the use of this charge state: the detection of ³⁹K³⁺ would not be possible because of the rates of ¹³C⁺ were expected to be so high that they would saturate the detector. Our recent studies at SARA, nevertheless, show that ¹³C⁺ rates are not so high, and the K-correction can

¹Where ⁴¹M denotes all the ions with mass 41, this is, ⁴¹M \equiv ⁴¹K+⁴¹Ca

be also used when the 3+ state is selected (see [chapter 4](#)).

Using the K-correction, the $^{39}\text{K}/^{40}\text{Ca}$ ratio becomes a relevant factor involved in the final uncertainty of the results. Besides, since ^{39}K and ^{41}M are not measured simultaneously, but sequentially, huge changes in the $^{39}\text{K}/^{40}\text{Ca}$ ratio should be avoided. It is clear, then, that understanding the factors related to the production of the ^{41}K interference is extremely important for ^{41}Ca AMS at low energies. In the next sections, several experiments related to this interference, performed during this thesis with both systems, SARA and TANDY, are presented.

3.2 Studies of the sources of the ^{41}K interference

During the first tests of ^{41}Ca AMS using calcium fluoride, it was thought that the $(\text{KF}_3)^-$ ion is a totally unstable ion, and the ^{41}K interference is not caused by the production of $(^{41}\text{KF}_3)^-$ ions, but from other molecular ions where ^{41}K is present and with the same mass, 98 u [[Fink et al., 1990](#)]. [Zhao et al. \[2010\]](#) proved, though, that F^+ ions were produced from the stripping of ions with a mass of 96 u, consequently identifying those ions as $(^{39}\text{KF}_3)^-$, confirming the existence of the ion. The slight stability from the $(\text{KF}_3)^-$ ion, the fluorine present in the CaF_2 sample, and the relatively high trace amount of potassium typically found in Cs, make possible the production of $(^{41}\text{KF}_3)^-$ ions, even in the theoretical case where there is no potassium trace amount within the cathode.

The existence of the $(\text{KF}_3)^-$ ion, nevertheless, does not mean that this ion is the only negative ion leading to ^{41}K interference. The relatively high mass of the $(^{41}\text{KF}_3)^-$ ion would allow, also, the formation of other several different ions with the same mass, 98 u, and where potassium is present. For instance, a common observation during experiments during this thesis is the detection of relatively high rates of both ^{41}K and ^{39}K ions when material with no fluorine was sputtered. This has been systematically observed with both systems, SARA and TANDY. [Zhao et al. \[2010\]](#) proposed the theory that another important negative ion related to ^{41}K interference would be the $(^{41}\text{K}^{57}\text{Fe})^-$ ion, since it has also, a mass of 98 u. They also checked that adding iron to the samples increased the ^{41}K rates. This would explain the high ^{41}K rates when metal is sputtered.

In order to prove that this theory is correct, and that their increase on the ^{41}K rates was not due to a higher trace amount of potassium in their iron material, an experiment was performed with the TANDY system during thw stay at the [ETH LIP](#). This experiment consisted in the measurement of the $^{41}\text{M}^{2+}$, $^{39}\text{K}^{2+}$, $^{57}\text{Fe}^{2+}$ and $^{19}\text{F}^+$ rates in a blank sample and an aluminum dummy. $^{41}\text{M}^{2+}$ and $^{39}\text{K}^{2+}$ rates were measured sequentially using the slow switching

of the terminal and ESA voltages, as it is done during routine ⁴¹Ca measurements at that system. For the later detection of the other ions, the magnetic field from the HEM was changed, first, so that it selected the magnetic rigidity of the ⁵⁷Fe²⁺ ions, and then, changed again to select the one of ¹⁹F⁺. Because of this, only qualitative comparisons between these ions and both potassium ion rates can be done. Only during the detection of ⁴¹K the bouncer magnet was set to select a mass of 98 u, this is, (⁴¹KF₃)⁻ and (⁴¹K⁵⁷Fe)⁻ ions; in the rest of the cases, a mass of 96 u, this is, (³⁹KF₃)⁻ and (³⁹K⁵⁷Fe)⁻ ions, was selected in the low energy side.

As it can be seen in Table 3.2, ⁵⁷Fe was indeed detected, and its rates were almost directly proportional to those from ⁴¹M and ³⁹K. The rates from these 3 ions were one order of magnitude higher in the Al dummy than in the blank sample. In order to ensure that the ions with mass 57 were ⁵⁷Fe ions, the He stripper pressure was increased up to 2.5 times the pressure used during routine ⁴¹Ca measurements. No significant decrease of the ion rates was observed, which should have happened if those ions were molecular ions. Another discarded option was that those ions had been other elemental ions with a $\frac{M}{q}$ ratio of 28.5, based on two evidences:

1. Only ions with $M = 57 \cdot n$, with $n = \frac{q}{2}$ being an integer, would have that $\frac{M}{q}$ ratio. Since the mass M_0 selected in the LE side was 96 u, the only mass $M = 57 \cdot n$ which fulfils $M < M_0$ is 57 u, which only has one stable isobar: ⁵⁷Fe.
2. The energy of these ions, according to the GIC detector spectrum, was consequent with the theoretical energy that ⁵⁷Fe²⁺ ions should have in those conditions.

It seems clear that ⁵⁷Fe played an important role in the production of ⁴¹K interference when the aluminum dummy was sputtered, while the (⁴¹KF₃)⁻ was the main source in the case of the fluoride sample. Nevertheless, the high mass difference $M_0 - M$ allows the formation of several different negative ions leading to ⁴¹K interference.

In any case, it is a fact that the sputtering of metallic parts does increase the ⁴¹K interference, so it is interesting to know how this interference depends on the material used, for instance,

Table 3.2: Rates from different ions in an aluminum dummy and a blank sample during the experiment with the 600 kV AMS system at ETH. The ¹⁹F⁺ rate with the blank sample could not be measured because it saturated the detector. Standard deviations were used as uncertainties.

Ion	⁴¹ M ²⁺	³⁹ K ²⁺	⁵⁷ Fe ²⁺	¹⁹ F ⁺
Mass injected in LE side (u)	98	96	96	96
Rate on CaF ₂ blank (s ⁻¹)	143.4 ± 3.5	1402 ± 34	194 ± 29	>10000
Rate on Al dummy (s ⁻¹)	1243 ± 63	16270 ± 550	1368 ± 95	460 ± 14

as target holder. At ETH LIP there are 3 different metals available as target holders for the TANDY ion source: titanium (Ti), copper (Cu) and aluminum (Al). To test the possible dependence of the target holder material on the ^{41}K interference, the $^{39}\text{K}/^{40}\text{Ca}$ ratio was measured in blank and standard samples pressed in cathodes of the 3 different materials. For each of these materials, 2 blank cathodes and 3 standards, each one with a different $^{41}\text{Ca}/^{40}\text{Ca}$ ratio, were pressed. The use of different standards was not relevant because of their different nominal $^{41}\text{Ca}/^{40}\text{Ca}$ ratio, but for testing the target holders with different CaF_2 material.

This experiment was conducted after a small accident which stained the ion source with cesium. After the cleaning of the ion source, ^{39}K rates were still higher than usual, which was taken advantage of to study the relationship between the ^{41}K interference and the target holder material. In Figure 3.3, the evolution of the $^{39}\text{K}/^{40}\text{Ca}$ ratios is shown.

As expected, no dependence on the CaF_2 material used (blank, standard...) was observed, so no reference to that is shown in the figure. After 30 minutes, the $^{39}\text{K}/^{40}\text{Ca}$ ratios were already stable and in the 10^{-10} - 10^{-9} range, as it happens in optimal conditions. At this plateau region, no relevant difference between the copper and titanium targets were observed, being their average $^{39}\text{K}/^{40}\text{Ca}$ ratios, respectively, $(3.53 \pm 0.90) \times 10^{-10}$ and $(4.2 \pm 1.5) \times 10^{-10}$. On the other hand, aluminum targets exhibited a slightly higher $^{39}\text{K}/^{40}\text{Ca}$ ratio of $(7.3 \pm 2.0) \times 10^{-10}$.

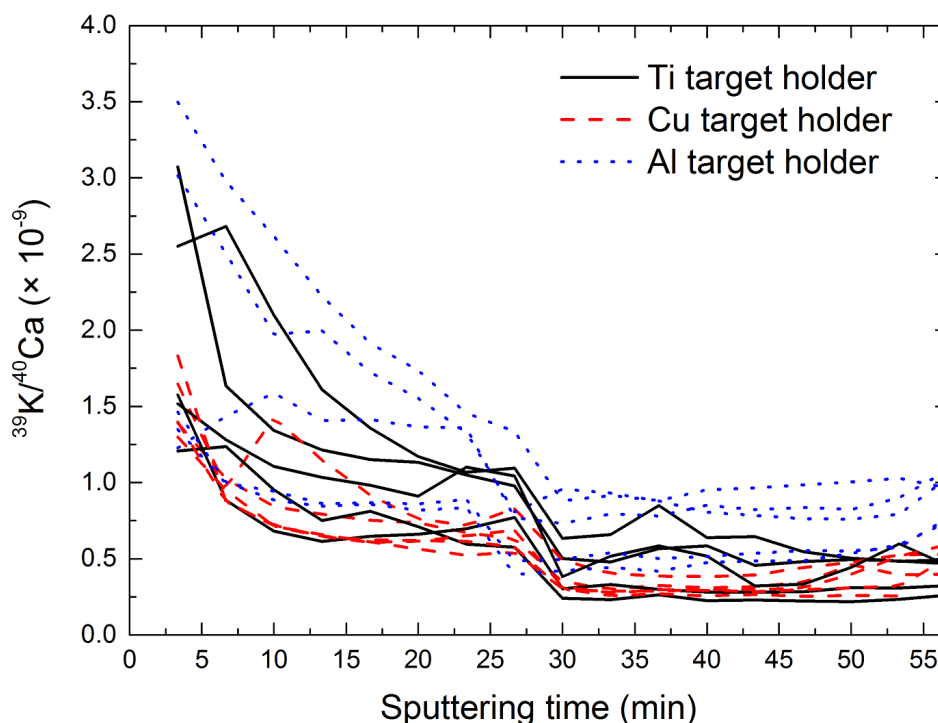


Figure 3.3: Evolution of $^{39}\text{K}/^{40}\text{Ca}$ ratios from blank and standard samples in target holders from different materials.

Commercial chemical companies typically report a higher iron trace amount for aluminum than, for instance, for copper, so these slightly higher $^{39}\text{K}/^{40}\text{Ca}$ ratios could be a direct consequence from the $(^{39}\text{K}^{57}\text{Fe})^-$ ion production.

The possible influence of ^{57}Fe in the production of ^{41}K interference makes advisable taking into account iron-calcium separation during the chemical preparation of the samples, as well as avoiding the use of steel material for any part of the cathode.

3.3 Time evolution of the ^{41}K interference

The possibility of producing the ^{41}K interference even when an area different from the actual sample is sputtered implies that ^{39}K and ^{41}K rates are not directly related to the $(^{40}\text{CaF}_3)^-$ ion source output, which produces appreciable temporal changes in the $^{41}\text{K}/^{40}\text{Ca}$ interference. A better explanation of how the measurement time is structured is presented in [section 3.4](#). This feature can be perfectly seen in the results from one of the ^{41}Ca measurements with the 1 MV AMS system at CNA. More information about the setup of this system for ^{41}Ca measurements is presented in [chapter 4](#). Even when, recently, experiments with the 3+ state have been made, these measurements were performed selecting the 2+ state.

A measurement performed with a non optimal ion source output was selected to study the relationship between the temporal evolution of the ^{41}K interference and the stability of the ion source output. [Figure 3.4](#) and [Figure 3.5](#) represent, for 2 different blank targets used during this measurement, the time evolution of the $^{40}\text{Ca}^{2+}$ current; the $^{41}\text{M}^{2+}$ and $^{39}\text{K}^{2+}$ rates; and the $^{39}\text{K}/^{40}\text{Ca}$, $^{41}\text{M}/^{40}\text{Ca}$ and $^{41}\text{M}/^{39}\text{K}$ ratios. Note that ^{41}M and ^{39}K are not measured simultaneously, but sequentially. Even when both cathodes were pressed using the same CaF_2+Ag material, their evolution was very different.

In the first case (blank 1, [Figure 3.4](#)), the ion source current output was more stable, at least after 10 minutes of sputtering. The $^{40}\text{Ca}^{2+}$ ion current kept increasing 20-30 minutes further and, then, started a slight decrease. However, $^{41}\text{M}^{2+}$ and $^{39}\text{K}^{2+}$ rates were almost constant after the first 15-20 minutes of sputtering, implying an slight increasing of the $^{39}\text{K}/^{40}\text{Ca}$ and $^{41}\text{M}/^{40}\text{Ca}$ ratios when the $^{40}\text{Ca}^{2+}$ current decreases.

In the second case (blank 2, [Figure 3.5](#)), the $^{40}\text{Ca}^{2+}$ ion current was much more unstable. Its initial increase stops after 20 minutes of sputtering; then, the current started to decrease exponentially. On the other hand, $^{41}\text{M}^{2+}$ and $^{39}\text{K}^{2+}$ rates kept increasing 20 minutes more, reaching levels almost 2 times higher than those from blank 1. Consequently, the $^{41}\text{M}/^{40}\text{Ca}$ ratio from this blank reached levels even higher than 10^{-10} , while, for the blank 1, it kept

lower than 4×10^{-11} the most of the time.

A very different behavior was presented by the $^{41}\text{M}/^{39}\text{K}$ ratio. The changes in the $^{41}\text{M}/^{40}\text{Ca}$ ratios in both blanks were directly related to the changes in the $^{39}\text{K}/^{40}\text{Ca}$ ratio. This means that that time evolution of that $^{41}\text{M}/^{40}\text{Ca}$ ratio was only caused by changes in the $^{41}\text{K}/^{40}\text{Ca}$ interference, and not in the $^{41}\text{Ca}/^{40}\text{Ca}$ background. Therefore, the different behaviour between both blanks did not imply a sustantial difference in the $^{41}\text{M}/^{39}\text{K}$ ratio. In both cases, that ratio

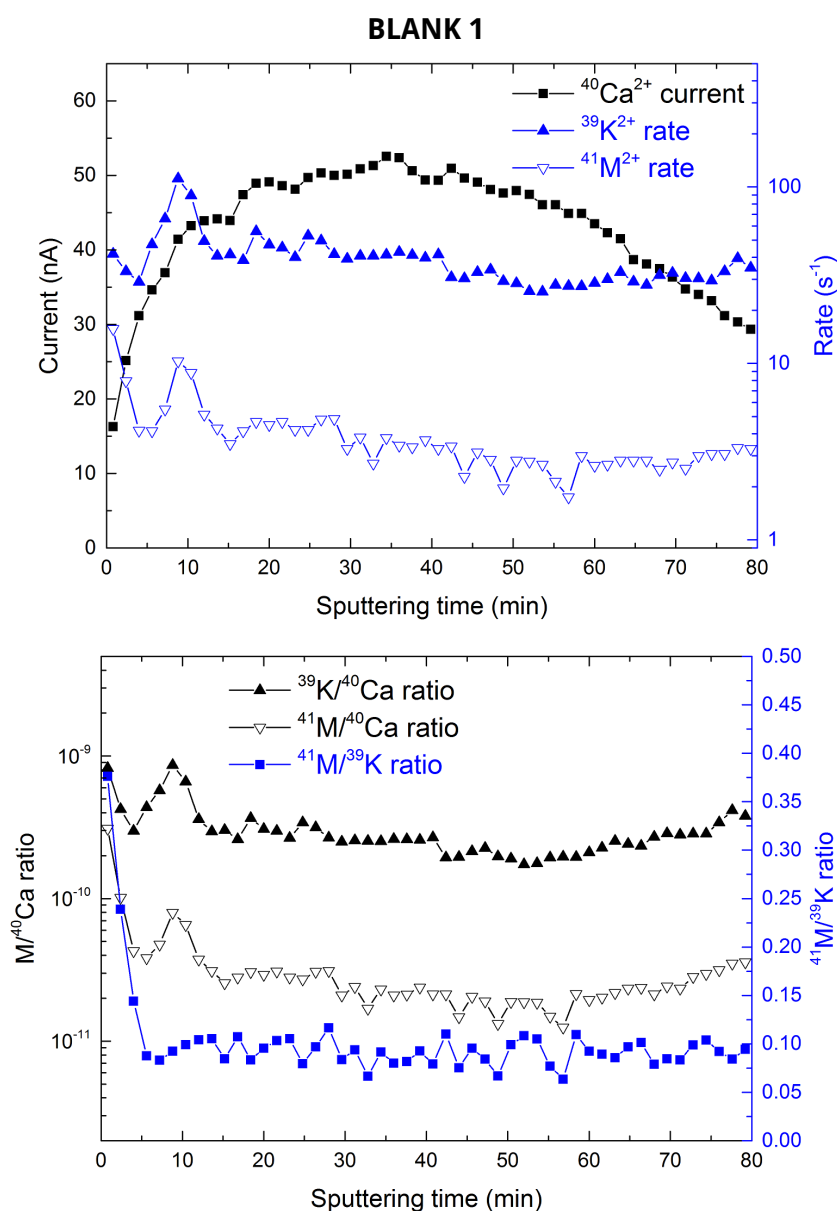


Figure 3.4: Time evolution of the $^{40}\text{Ca}^{2+}$ current, the $^{41}\text{M}^{2+}$ and $^{39}\text{K}^{2+}$ rates, and the $^{39}\text{K}/^{40}\text{Ca}$, $^{41}\text{M}/^{40}\text{Ca}$ and $^{41}\text{M}/^{39}\text{K}$ ratios for a blank sample (blank 1) during a measurement at SARA.

stayed stable, except for the first sputtering minutes. The $^{41}\text{M}/^{39}\text{K}$ ratio was 0.092 ± 0.012 for the blank 1, and 0.0843 ± 0.0096 for the blank 2.

The most plausible explanation to this different behaviour between both targets is that a slight difference in the sample mass used for each cathode had caused that the steel pin were closer to the surface. Copper pins are used now for the ^{41}Ca targets at SARA to avoid the influence of ^{57}Fe in the production of ^{41}K interference.

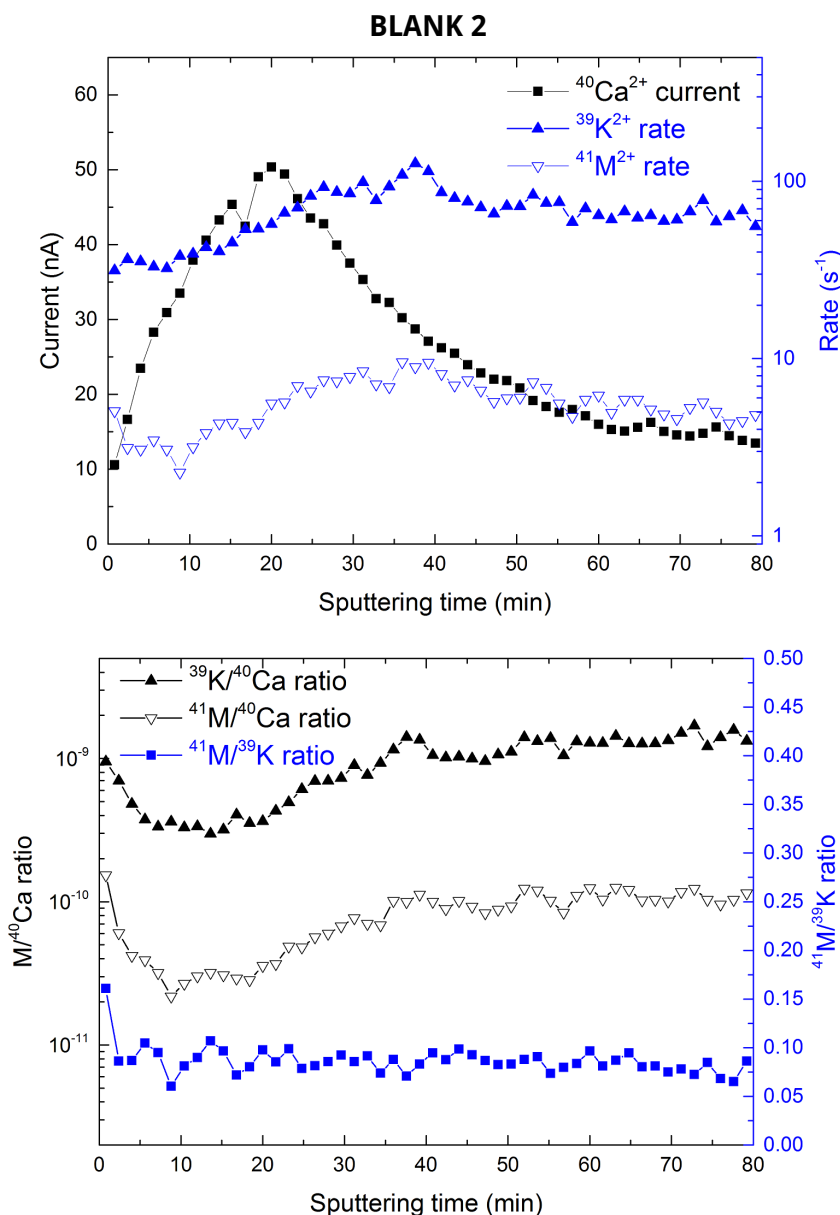


Figure 3.5: Time evolution of the $^{40}\text{Ca}^{2+}$ current, the $^{41}\text{M}^{2+}$ and $^{39}\text{K}^{2+}$ rates, and the $^{39}\text{K}/^{40}\text{Ca}$, $^{41}\text{M}/^{40}\text{Ca}$ and $^{41}\text{M}/^{39}\text{K}$ ratios for another blank sample (blank 2) during a measurement at SARA.

Summarizing, the key points that can be extracted from these results, and which are important to optimize the performance of the K-correction in ⁴¹Ca AMS at low energies, are:

- If there is such a huge change in the ⁴¹K/⁴⁰Ca ratio from one target to another, even when they are using the same blank material, treating the ⁴¹K interference as part of the background for ⁴¹Ca AMS at low energies compromises the reliability of the results.
- Even in the worst cases, the ⁴¹K/³⁹K measured ratio is quite stable, which proves that the K-correction is a robust method to estimate the ⁴¹K interference at low energies.
- Because of the temporal changes in the ⁴¹M/⁴⁰Ca and ³⁹K/⁴⁰Ca ratios, the K-correction should be applied sequentially (as explained in [section 3.4](#)), and not to the average ⁴¹M/⁴⁰Ca ratio from each sample, in order to reduce the final standard deviation.

Taking as example the measurement from which the previous results were obtained, the ⁴¹Ca/⁴⁰Ca background, after the K-correction, was $(7.1 \pm 2.4) \times 10^{-12}$, while the average total ⁴¹M/⁴⁰Ca ratio in blanks was $(66 \pm 35) \times 10^{-12}$. If we suppose that the limit of detection is directly proportional to the standard deviation of the background², this means that the limit of detection is lowered a factor ~ 15 by using the K-correction. More information about the ⁴¹Ca background at SARA is provided in [chapter 4](#).

3.4 Data analysis for ⁴¹Ca AMS at TANDY and SARA

General AMS measurements need the application of several corrections after performing the measurements in order to get reliable results. For instance, different causes typically lead to the identification of some events as ions from the radionuclide of interest, when they are not (background). In order to correct this background, samples with no content of the radionuclide (blanks) are also measured. Other fact that must be corrected is that, even after subtracting the background, the measured isotopic ratios may slightly differ from the real ones because of the optical losses suffered by radionuclide ions before reaching the detector. In order to solve that, samples with known content of the radionuclide of interest (standards) are also measured.

On the other hand, the specific challenges from each radionuclide make necessary additional corrections. In the case of ⁴¹Ca, even in large facilities, it is advisable to deal with the ⁴¹K ions which may interfere with the ⁴¹Ca spectrum in the detector [[Rugel et al., 2016](#)]. In the case of

²For instance, in analytical chemistry, the limit of detection is typically calculated as 3 times the standard deviation of the blank measurement.

^{41}Ca AMS at low energies, as it was stated in [section 3.1](#), the only way to estimate the whole contribution of this interference is during the data analysis. This K-correction becomes one of the key steps of this analysis.

The specific features of ^{41}Ca AMS data analysis at low energies depend on the system used, since available information slightly depends on the elements present on the system; for instance, the possibility of measuring the $(^{40}\text{CaF}_3)^-$ current on the LE side at TANDY makes possible using discard criteria based on the stripper transmission. However, the basic steps are the same.

In order to reduce the time consumed by this data analysis, 2 programs were written in FORTRAN code during this thesis: one for the measurements at TANDY, written during the 4 months stay at [ETH LIP](#); and another one, based on it, for the measurements at SARA. The code changes are only related to these slight differences in the information provided by each AMS system. More information about these programs is provided in [Appendix C](#).

In this section, an overview of the steps followed by these programs is presented.

3.4.1 AMS measurement

In order to understand the data analysis of the measurements, it is very important to know how the measurements are performed. [Figure 3.6](#) shows the typical measurement procedure in ^{41}Ca AMS at low energies. Each sample i ³ is introduced in the machine a number n_{runs} of runs. During each one of these (i, j) runs, both ions, ^{41}M and ^{39}K , are sequentially measured using different sequence times t_{41} and t_{39} for each one. Both ions are measured the same number of sequences n_{seqs} . Each ^{41}M sequence (i, j, k) , except the first one from each run, $(i, j, 1)$, is preceded by the ^{39}K sequence $(i, j, k - 1)$ and followed by the ^{39}K sequence (i, j, k) . Typically, 5 sequences of $t_{41} = 30$ s for ^{41}M , and $t_{39} = 10$ s for ^{39}K , are used in the measurements at SARA and TANDY. This time can be lower if a certain number of ion counts in the detector is reached.

The measurement of the ^{40}Ca current is performed in a different way at SARA than at TANDY. In the first case, a ^{40}Ca sequence is added just after the ^{41}M one, using the same terminal and ESA voltage than those used in ^{39}K sequences; the reason for this will be explained in [chapter 4](#). In the second case, the ^{40}Ca current is measured using the fast switching of the LEM bouncer during the ^{41}M sequence.

Theoretically, a system with 2 FCs in the HE side and with the proper software could mea-

³This includes not only the samples whose $^{41}\text{Ca}/^{40}\text{Ca}$ we want to know, but also blank and standard samples.

sure the ^{40}Ca current during both, the ^{41}M and the ^{39}K sequences, and it would be possible to directly get the $^{41}\text{M}/^{40}\text{Ca}$ ratio $\mathcal{R}_{41}^{\text{seq}}(i, j, k)$ and the $^{39}\text{K}/^{40}\text{Ca}$ ratio $\mathcal{R}_{39}^{\text{seq}}(i, j, k)$ from each sequence. At SARA and TANDY, the ^{40}Ca current is assumed to change linearly from one sequence to the next in order to calculate these ratios.

If the uncertainties of the ^{40}Ca current and the measuring time are disregarded, the statistical uncertainty from each of these $\mathcal{R}_A^{\text{seq}}(i, j, k)$ ratios, where A is either 41 or 39, is

$$\mathcal{U}_A^{\text{seq}}(i, j, k) = \frac{\mathcal{R}_A^{\text{seq}}(i, j, k)}{\sqrt{\mathcal{N}_A(i, j, k)}}, \quad (3.2)$$

where $\mathcal{N}_A(i, j, k)$ is the total number of ions with mass A detected in that sequence⁴.

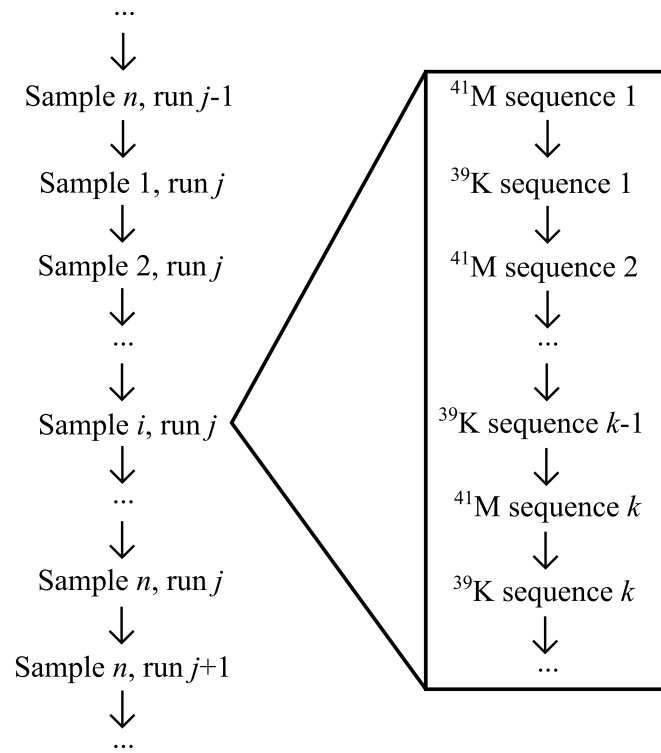


Figure 3.6: Typical scheme of a ^{41}Ca measurement with a compact AMS system implementing the K-correction.

⁴The uncertainty from $\mathcal{N}_A(i, j, k)$ is $\sqrt{\mathcal{N}_A(i, j, k)}$

3.4.2 Calculation of the experimental ⁴¹K/³⁹K ratio (K-correction factor)

In order to get the experimental ⁴¹K/³⁹K ratio α (or K-correction factor), the ⁴¹M/⁴⁰Ca and ³⁹K/⁴⁰Ca ratios from each run of the blank samples are used in order to perform the linear regression. These ratios are calculated as

$$\mathcal{R}_A^{\text{run}}(i, j) = \frac{\sum_{k=1}^{n_{\text{seqs}}} w_A^{\text{seq}}(i, j, k) \cdot \mathcal{R}_A^{\text{seq}}(i, j, k)}{\sum_{k=1}^{n_{\text{seqs}}} w_A^{\text{seq}}(i, j, k)}, \quad (3.3)$$

where $w_A^{\text{seq}}(i, j, k)$ is a weight function dependent on the ⁴⁰Ca current in that sequence $\mathcal{I}_A(i, j, k)$ and the sequence time $t_A(i, j, k)$, defined as

$$w_A(i, j, k) \equiv \mathcal{I}_A(i, j, k) \cdot t_A(i, j, k) \cdot \mathcal{C}_A^{\text{seq}}(i, j, k). \quad (3.4)$$

This weight function makes more important those sequences with higher statistics. The $\mathcal{C}_A^{\text{seq}}(i, j, k)$ is a logical factor which is 0 if any of the selection criteria (minimum ⁴⁰Ca current, for instance) is not passed, and 1 otherwise. The common selection criteria used at SARA and TANDY are presented in [subsection 3.4.5](#).

Once all the $\mathcal{R}_{41}^{\text{run}}(i, j)$ and $\mathcal{R}_{39}^{\text{run}}(i, j)$ ratios from the blank samples have been calculated, a linear regression is performed by the method of least squares, using the $\mathcal{R}_{41}^{\text{run}}(i, j)$ ratios as independent variable x , and $\mathcal{R}_{39}^{\text{run}}(i, j)$ as dependent variable y ⁵. The slope from this linear regression is the K-correction factor $\alpha \pm \mathcal{U}(\alpha)$.

3.4.3 Application of the K-correction and sample average

Since each ⁴¹M measurement sequence is performed between two ³⁹K sequences, the ³⁹K/⁴⁰Ca ratio which should be applied to correct the $\mathcal{R}_{41}^{\text{seq}}(i, j, k)$ ratio is not exactly $\mathcal{R}_{39}^{\text{seq}}(i, j, k)$, neither $\mathcal{R}_{39}^{\text{seq}}(i, j, k-1)$. Nevertheless, since the expected changes in this ³⁹K/⁴⁰Ca ratio are slight in the time scale between two sequences, during the ⁴¹M sequence it can be supposed to be the average from the previous and the following one. The K-corrected ⁴¹Ca/⁴⁰Ca ratio from each sequence, therefore, is

⁵ $[x; y](i, j) = [\mathcal{R}_{41}^{\text{run}}(i, j); \mathcal{R}_{39}^{\text{run}}(i, j)]$

$$\begin{aligned} \mathcal{R}_{\text{K-corrected}}^{\text{seq}}(i, j, k) &= \\ &= \mathcal{R}_{41}^{\text{seq}}(i, j, k) - \alpha \cdot \frac{\mathcal{R}_{39}^{\text{seq}}(i, j, k-1) + \mathcal{R}_{39}^{\text{seq}}(i, j, k)}{2} \quad : \quad k = [2, n_{\text{seqs}}] . \end{aligned} \quad (3.5)$$

The uncertainty from this K-corrected ratio is calculated as

$$\mathcal{U}_{\text{K-corrected}}^{\text{seq}}(i, j, k) = \sqrt{[\mathcal{U}_{41}^{\text{seq}}(i, j, k)]^2 + \left[\alpha \cdot \frac{\mathcal{R}_{39}^{\text{seq}}(i, j, k-1) + \mathcal{R}_{39}^{\text{seq}}(i, j, k)}{2\sqrt{\mathcal{N}_{39}(i, j, k-1) + \mathcal{N}_{39}(i, j, k)}} \right]^2 + \left[\mathcal{U}(\alpha) \cdot \frac{\mathcal{R}_{39}^{\text{seq}}(i, j, k-1) + \mathcal{R}_{39}^{\text{seq}}(i, j, k)}{2} \right]^2} . \quad (3.6)$$

Using the same weight functions $w_{41}(i, j, k)$ used to calculate the uncorrected $^{41}\text{M}/^{40}\text{Ca}$ ratios from each blank sample run, the K-corrected $^{41}\text{Ca}/^{40}\text{Ca}$ ratios from each run can be calculated for every sample as

$$\mathcal{R}_{\text{K-corrected}}^{\text{run}}(i, j) = \frac{\sum_{k=2}^{n_{\text{seqs}}} w_{41}^{\text{seq}}(i, j, k) \cdot \mathcal{R}_{\text{K-corrected}}^{\text{seq}}(i, j, k)}{\sum_{k=2}^{n_{\text{seqs}}} w_{41}^{\text{seq}}(i, j, k)} . \quad (3.7)$$

and the standard deviation is

$$\begin{aligned} \mathcal{S}_{\text{K-corrected}}^{\text{run}}(i, j) &= \\ &= \sqrt{\frac{N_{\text{effseqs}}(i, j)}{N_{\text{effseqs}}(i, j) - 1} \cdot \frac{\sum_{k=2}^{n_{\text{seqs}}} w_{41}^{\text{seq}}(i, j, k) \cdot [\mathcal{R}_{\text{K-corrected}}^{\text{seq}}(i, j, k) - \mathcal{R}_{\text{K-corrected}}^{\text{run}}(i, j)]^2}{\sum_{k=2}^{n_{\text{seqs}}} w_{41}^{\text{seq}}(i, j, k)}} , \end{aligned} \quad (3.8)$$

where $N_{\text{effseqs}}(i, j)$ is defined as the number of sequences in the run (i, j) where $C_{41}^{\text{seq}}(i, j, k) = 1$. The standard deviation is only calculated if $N_{\text{effseqs}}(i, j) > 1$.

Assuming a virtual number of ^{41}Ca counts in each sequence equal to $\left[\frac{\mathcal{R}_{\text{K-corrected}}^{\text{seq}}(i, j, k)}{\mathcal{U}_{\text{K-corrected}}^{\text{seq}}(i, j, k)} \right]^2$, the uncertainty of $\mathcal{R}_{\text{K-corrected}}^{\text{run}}(i, j)$ is

$$\mathcal{U}_{\text{K-corrected}}^{\text{run}}(i, j) = \frac{\mathcal{R}_{\text{K-corrected}}^{\text{run}}(i, j)}{\sqrt{\sum_{k=2}^{n_{\text{seqs}}} \left[C_{41}^{\text{seq}}(i, j, k) \cdot \frac{\mathcal{R}_{\text{K-corrected}}^{\text{seq}}(i, j, k)}{\mathcal{U}_{\text{K-corrected}}^{\text{seq}}(i, j, k)} \right]^2}} , \quad (3.9)$$

The weight function $w^{\text{run}}(i, j)$ from each run is defined as

$$w^{\text{run}}(i, j) \equiv \begin{cases} 0 & \text{if } \mathcal{C}^{\text{run}}(i, j) = 0 \\ \left[\frac{\mathcal{R}_{\text{K-corrected}}^{\text{run}}(i, j)}{\mathcal{U}_{\text{K-corrected}}^{\text{run}}(i, j)} \right]^2 & \text{if } N_{\text{effseqs}}(i, j) = 1 \\ \min \left\{ \left[\frac{\mathcal{R}_{\text{K-corrected}}^{\text{run}}(i, j)}{\mathcal{S}_{\text{K-corrected}}^{\text{run}}(i, j)} \right]^2 ; \left[\frac{\mathcal{R}_{\text{K-corrected}}^{\text{run}}(i, j)}{\mathcal{U}_{\text{K-corrected}}^{\text{run}}(i, j)} \right]^2 \right\} & \text{if } N_{\text{effseqs}}(i, j) > 1 \end{cases}, \quad (3.10)$$

where, evidently, at least one of the criteria making $\mathcal{C}^{\text{run}}(i, j) = 0$ is that $N_{\text{effseqs}}(i, j) = 0$. This way, those runs where the behavior was more stable and, therefore, with lower relative uncertainties, take more importance. The sample average of the K-corrected ⁴¹Ca/⁴⁰Ca ratio $\mathcal{R}_{\text{K-corrected}}(i)$ and its standard deviation $\mathcal{S}_{\text{K-corrected}}(i)$ are calculated from the results of the runs in an analogous way as these results of the runs are calculated from the results of the sequences. The uncertainty is calculated as

$$\mathcal{U}_{\text{K-corrected}}(i) = \frac{\mathcal{R}_{\text{K-corrected}}(i)}{\sqrt{\sum_{j=1}^{n_{\text{runs}}} w^{\text{run}}(i, j)}}. \quad (3.11)$$

3.4.4 Blank and standard correction

The next corrections are common to almost all the **AMS** measurements, no matter the system or the radionuclide. The background \mathcal{B} is calculated as the non-weighted average of the K-corrected ratios from all the blank targets. This way, the blank corrected ratio from each sample is

$$\mathcal{R}_{\text{BLK-corrected}}(i) = \mathcal{R}_{\text{K-corrected}}(i) - \mathcal{B}. \quad (3.12)$$

In this case, no weight function is added since no reason makes some blank samples more scientifically relevant than others. The uncertainty from this ratio is

$$\mathcal{U}_{\text{BLK-corrected}}(i) = \begin{cases} \sqrt{[\mathcal{U}_{\text{K-corrected}}(i)]^2 + [\mathcal{S}(\mathcal{B})]^2} & \text{if } \int_0^s \chi^2[x; N_{\text{effruns}}(i) - 1] dx < 0.95 \\ \sqrt{[\mathcal{S}_{\text{K-corrected}}(i)]^2 + [\mathcal{S}(\mathcal{B})]^2} & \text{if } \int_0^s \chi^2[x; N_{\text{effruns}}(i) - 1] dx \geq 0.95 \end{cases}, \quad (3.13)$$

where $\mathcal{S}(\mathcal{B})$ is the standard deviation of the background, $N_{\text{effruns}}(i)$ is the total number of runs from the sample i with $w^{\text{run}}(i, j) > 0$, and $s \equiv \left[\frac{\mathcal{S}_{\text{K-corrected}}(i)}{\mathcal{U}_{\text{K-corrected}}(i)} \right]^2 \cdot [N_{\text{effruns}}(i) - 1]$.

The next step is the correction of the stripping and optical fractionation, or standard correction. The $\mathcal{R}_{\text{exp}}(\ell)$ from each standard material ℓ , with a nominal $^{41}\text{Ca}/^{40}\text{Ca}$ ratio of $\mathcal{R}_{\text{nom}}(\ell)$, is calculated as the non-weighted average of the BLK-corrected ratios from all the targets of that standard material. If that average has a standard deviation $\mathcal{S}_{\text{ratio}}(\ell)$, the nominal/experimental factor $f(\ell) = \frac{\mathcal{R}_{\text{nom}}(\ell)}{\mathcal{R}_{\text{exp}}(\ell)}$ will have a standard deviation $\sigma_f(\ell) = \frac{\mathcal{S}_{\text{ratio}}(\ell)}{\mathcal{R}_{\text{nom}}(\ell)} \cdot f(\ell)$.

Since, typically, several different standard materials are used during measurements, the final nominal/experimental factor \mathcal{F} applied for the standard correction will be the non-weighted average of the different $f(\ell)$ factors. No weight function is applied because the same reasons as those for blank correction: no reason makes some standard samples more scientifically relevant than others. If this produces a standard deviation $\sigma(\mathcal{F})$, the final uncertainty of the standard correction factor \mathcal{F} is

$$\mathcal{U}(\mathcal{F}) = \max \left\{ \sigma(\mathcal{F}); \frac{\mathcal{F}}{\sum_{\ell} \left[\frac{f(\ell)}{\sigma_f(\ell)} \right]^2} \right\}. \quad (3.14)$$

The final $^{41}\text{Ca}/^{40}\text{Ca}$ from each sample is, therefore,

$$\mathcal{R}_{\text{STD-corrected}}(i) = \mathcal{F} \cdot \mathcal{R}_{\text{BLK-corrected}}(i), \quad (3.15)$$

with an uncertainty

$$\mathcal{U}_{\text{STD-corrected}}(i) = \sqrt{[\mathcal{U}(\mathcal{F}) \cdot \mathcal{R}_{\text{BLK-corrected}}(i)]^2 + [\mathcal{F} \cdot \mathcal{U}_{\text{BLK-corrected}}(i)]^2}. \quad (3.16)$$

3.4.5 Common selection criteria used at SARA and TANDY

The only selection criteria used only in ^{41}Ca measurements at TANDY, and not at SARA, are those related to the stripper transmission, since that information is available in the measurements with that system. Typically, sequences (i, j, k) where the stripper pressure has a difference of 5% or higher with either the average transmission through the whole measurement, or the average transmission during that run (i, j) , are discarded. Nevertheless, these possible changes in the transmission are not expected to be relevant at SARA, where the optical losses are lower for ^{41}Ca .

Therewith, the rest of selection criteria, used also in the measurement at SARA, are presented, and the reasons to apply them are explained.

Ignoring first run

As it can be seen in [section 3.3](#), during the first sputtering minutes the ion source current output typically presents a quite unstable behaviour. It is advisable not to use these results in the data analysis, so a common selection criterion is that

$$C^{\text{run}}(i, 1) = 0 \quad \forall i. \quad (3.17)$$

Minimum ⁴⁰Ca current output

A very low ion source current output within a sequence (i, j, k) can be symptomatic of a temporal failure, which makes the results of the ratios from that sequence not representative of the reality. Besides, a low current output is a common feature of time intervals where that same output is more unstable; for instance, when the target is starting to run out of sample material. In order to work with sequences where the behaviour of this output is stable, a minimum ⁴⁰Ca current \mathcal{I}_{min} can be established. For any sequence $(i, j, k) : \mathcal{I}_A(i, j, k) < \mathcal{I}_{\text{min}}$, the weight function will be set as 0. This minimum current should be established taking into account the average currents observed during that measurement, as well as the typical currents observed historically with that [AMS](#) system. At SARA for instance, we typically use a minimum ⁴⁰Ca²⁺ current of 20 nA.

Maximum ion rate

[GIC](#) detectors typically do not work properly when the total ion rates are too high. In these cases, mainly 2 effects reduce the detection efficiency:

- The pile-up, or combination of the signals from 2 or more ions, producing a signal proper to an ion with a higher energy.
- The saturation of the electronic chain that transform the signal produced by the ion into a digital one.

It is suitable, therefore, to establish a maximum ion rate, so the sequences where that ⁴¹M or ³⁹K rates are higher are discarded. To establish this limit, a study of the relationship between the ion rate and the [GIC](#) detector efficiency should be performed. More information about the efficiency of the SARA [GIC](#) and the typical maximum rates in our measurements is presented in [chapter 4](#).

Maximum $^{39}\text{K}/^{40}\text{Ca}$ ratio

In order to take the measurements of each sample where the ^{41}K interference was the least, and to avoid the unstable behaviour of the $^{39}\text{K}/^{40}\text{Ca}$ ratio when it is higher, a maximal $^{39}\text{K}/^{40}\text{Ca}$ ratio $\mathcal{R}_{39}^{\text{MAX}}$ can be set, so all the runs (i, j) where the average $^{39}\text{K}/^{40}\text{Ca}$ ratio $\mathcal{R}_{39}^{\text{run}}(i, j)$ is higher than $\mathcal{R}_{39}^{\text{MAX}}$ are discarded. This also avoids the extrapolation of the K-correction factor for $\mathcal{R}_{39}^{\text{run}}(i, j)$ higher than those found in blank samples, provided that this maximum $^{39}\text{K}/^{40}\text{Ca}$ ratio is lower or equal than the highest $^{39}\text{K}/^{40}\text{Ca}$ ratio found in blank samples. This maximum $^{39}\text{K}/^{40}\text{Ca}$ ratio is typically set in $1-2 \times 10^{-9}$ range, so the $^{41}\text{K}/^{40}\text{Ca}$ interference is expected to stay in the 10^{-11} - 10^{-10} range.

Chapter 4

Setup of the 1 MV AMS system at CNA for ^{41}Ca measurements

In this chapter, several experiments performed throughout this thesis related to the performance parameters for ^{41}Ca measurements at SARA are detailed. These parameters are related to the final efficiency of the ^{41}Ca ion detection in order to provide a strong statistics, and the final $^{41}\text{Ca}/^{40}\text{Ca}$ background and sensitivity. The most important results presented here were also presented in [Vivo-Vilches et al. \[2017\]](#). The specific parameters studied and/or optimized have been:

- The $(^{40}\text{CaF}_3)^-$ current output with the SO-110B ion source ([section 4.1](#)).
- The transmission in the He gas stripper of the charge states 2+ and 3+ ([section 4.2](#)).
- The detection efficiency and signal identification ΔE - E_{res} spectra of the compact GIC ([section 4.3](#)).
- The linear correlation between ^{41}K and ^{39}K ions and the final ^{41}Ca background after the K-correction ([section 4.4](#)).
- The optical transmission of ^{41}Ca through the HE spectrometer by the comparison of nominal and experimental ratios in standard samples ([section 4.5](#)).

A comparison of these performance parameters with those at TANDY is also presented in [section 4.6](#). In order to complete this comparison, measurements of the ETH LIP in-house ^{41}Ca standards [[Christl et al., 2013](#)] and several samples of biomedical interest previously measured at TANDY are also shown.

4.1 Optimization of the ion source extraction

The ionization efficiency of Cs sputtering not only depends on the electron affinity of the ionized element or molecule, but also on both the thermal and the electrical conductivities of the material within the sample target. In order to produce the $(\text{CaF}_3)^-$ ions, therefore, it is necessary to mix the calcium fluoride¹ with a metallic element (binder). The most common element with which CaF_2 is mixed for ^{41}Ca AMS is silver (Ag), but, for other radionuclides, other materials, like niobium (Nb), are used.

In a simple model, therefore, it can be assumed that the ionization efficiency \mathcal{E} depends only on the relative volume occupied by the binder. The total number of $(\text{CaF}_3)^-$ ions produced would be, then, directly proportional to the product of this efficiency and the relative volume occupied by the sample. Consequently, it can be proven that the maximum total production of $(\text{CaF}_3)^-$ ions is achieved when the relative volume occupied by the binder and the one occupied by the CaF_2 sample are the same. In terms of weight ratio, this means that the optimal ion source performance is achieved when the CaF_2 :binder weight ratio is

$$\mathcal{X} = \frac{\rho(\text{CaF}_2)}{\rho(\text{binder})}, \quad (4.1)$$

where $\rho(\text{binder})$ and $\rho(\text{CaF}_2) = 3.18 \text{ g} \cdot \text{cm}^{-3}$ are the densities of, respectively, the binder and CaF_2 . In the case of a CaF_2 :Ag mix, this optimal weight ratio would be 1:3.3. Nevertheless, this theoretical result, based on simple assumptions, is not totally reliable. For instance, with the ion source at TANDY, the optimal CaF_2 :Ag weight ratio is 1:9.

In order to make sure that the optimal binder material at SARA is also silver, and to find the optimal weight ratio, the $(^{40}\text{CaF}_3)^-$ current from different targets of blank CaF_2 mixed with Ag or Nb at different weight ratios was measured. The results of these measurements are shown in [Figure 4.1](#). It is clear that silver was, in any case, a much better choice as binder material than niobium, getting higher and more stable $(^{40}\text{CaF}_3)^-$ currents. Few tests were performed, also, using copper as binder material at different weight ratios. $(^{40}\text{CaF}_3)^-$ currents were also much lower than those obtained using silver.

From the CaF_2 :Ag mixes, those with weight ratios of 1:2 and 1:4 exhibited the highest and most stable current outputs. The slight difference between both is not representative, since only one target from each one of them was measured. These same optimal weight ratios were found in the the 6 MV AMS system in Dresden (Germany), which uses a similar ion

¹As any ionic compound, CaF_2 has electric and thermal conductivities on its solid form much lower than those from metallic elements.

source [Rugel et al., 2016].

At SARA, consequently, CaF_2 :Ag mixes of weight ratio 1:4 are used. This way, the optimal ion source output is combined with a use of less CaF_2 material. Interestingly, this ratio is close to the one which was theoretically calculated (1:3.3), assuming that the ionization efficiency depends only on the relative volume occupied by silver.

A better assessment of the ionization efficiency is performed by studying the evolution of the $(^{40}\text{CaF}_3)^-$ current over a longer time period, as it can be seen in Figure 4.2. Integrating the current over the time, and comparing the total number of $(^{40}\text{CaF}_3)^-$ ions produced with the number of ^{40}Ca atoms in the sample, the ionization efficiency is obtained. An exponential fitting of the final results is necessary to complete this integral to infinite. For the results on Figure 4.2, the result of this integral, was 6.1×10^{15} $(^{40}\text{CaF}_3)^-$ ions in one of the blanks, and 7.3×10^{15} $(^{40}\text{CaF}_3)^-$ ions in the other one. Taking into account that in each cathode there is, approximately, 1 mg of CaF_2 , this is, around 7.5×10^{18} ^{40}Ca atoms, the ionization efficiency is very close to 0.1%.

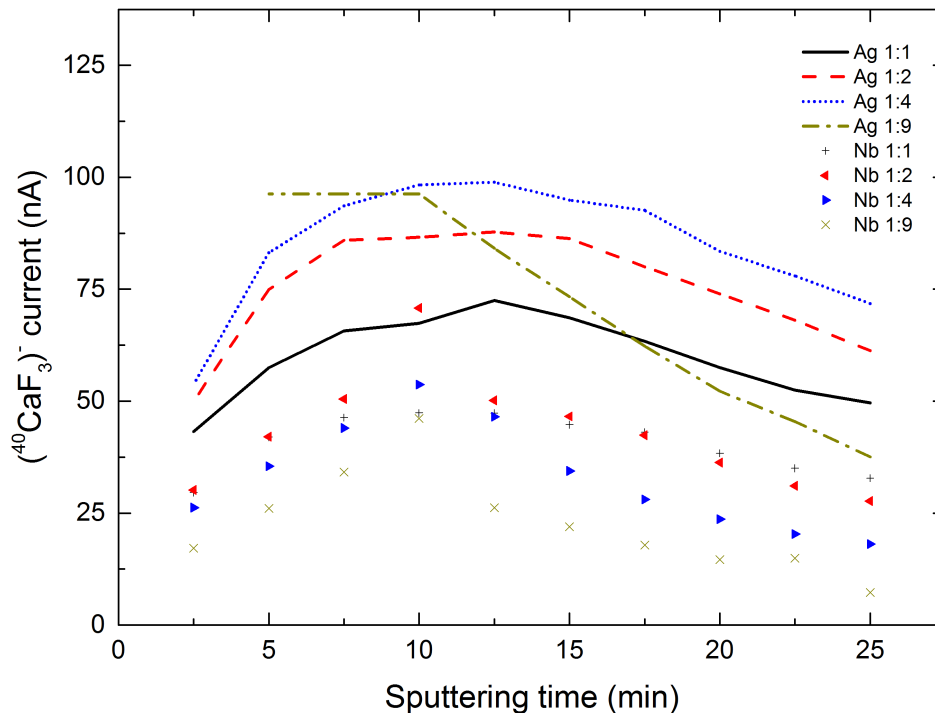


Figure 4.1: $(^{40}\text{CaF}_3)^-$ current output from the SO-110B ion source at SARA for different blank targets mixed with silver or niobium at different weight ratios.

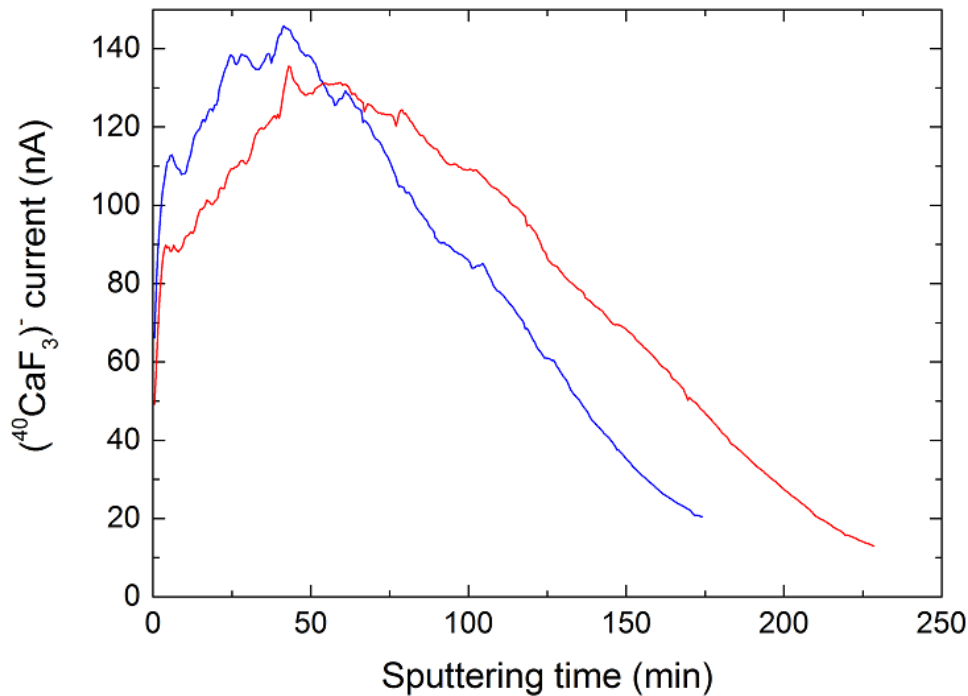


Figure 4.2: ($^{40}\text{CaF}_3$)⁻ current from 2 different blank samples over a long time range.

4.2 He stripper performance

As well as the ionization efficiency, the stripper transmission is other parameter related to the final counting efficiency which can importantly change. The other two parameters involved (optical transmission and detection efficiency) are typically higher than 80%, at SARA, for every radionuclide. The He stripper performance for the most populated charge states, 2+ and 3+, are presented in this section.

4.2.1 2+ state

When the charge state 2+ is used, a relatively high molecular background is expected when low stripper pressures are used, and it is necessary to make sure that this interference is destroyed in the stripping process. Consequently, the dependence on the stripper gas pressure of both the transmission and the blank $^{41}\text{M}/^{40}\text{Ca}^{2+}$ ratio must be studied.

These dependences for the He stripper, at a terminal voltage of ~ 950 kV (stripping energy of ~ 400 keV), are presented in Figure 4.3. As it can be seen, the highest ($^{40}\text{CaF}_3$)⁻ \rightarrow $^{40}\text{Ca}^{2+}$ trans-

²Here, ^{41}M denotes not only ^{41}K and ^{41}Ca ions, but also molecular ions with a mass of 41 u. These ratios are those directly given by the measurement software, so no correction is applied.

mission, around 45%, is found for He pressures in the 0.01-0.015 mbar range. On the other hand, molecular background is still not totally destroyed when those pressures are used, with blank $^{41}\text{M}/^{40}\text{Ca}$ ratios in the 10^{-10} range. For a He pressure of 0.03 mbar, transmission is still higher than 40%, and the total destruction of the molecular background is achieved, since the blank $^{41}\text{M}/^{40}\text{Ca}$ ratio is equivalent to that for higher stripper pressures. Therefore, a He gas pressure of 0.03 mbar is used during the ^{41}Ca measurements at SARA. The transmission for the $2+$ state is almost 2 times higher than the one achieved at the same energy using Ar as stripping gas, which is 23% [Heinemeier et al., 2015].

The curve used to fit the dependence of the $^{40}\text{Ca}^{2+}$ transmission T_{2+} on the He mass thickness ρ_A was

$$T_{2+}(\rho_A) = \underbrace{\Phi_{2+}[1 - e^{-\Sigma_p \cdot \rho_A}]}_{\text{Production}} \underbrace{(1 - \Sigma_m \cdot \rho_A)}_{\text{Optical losses}}, \quad (4.2)$$

where Φ_{2+} is the charge state fraction of the state $2+$ for calcium in helium at that stripping energy, Σ_p is a theoretical cross section for $(^{40}\text{CaF}_3)^-$ stripping in helium gas, and Σ_m a

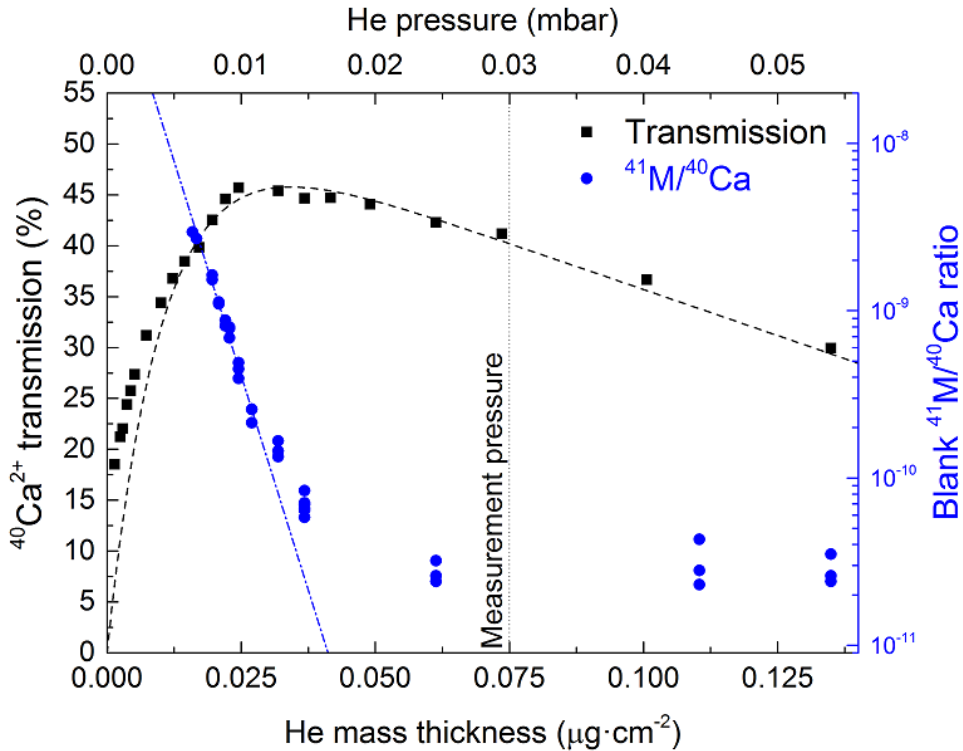


Figure 4.3: $^{40}\text{Ca}^{2+}$ transmission and $^{41}\text{M}/^{40}\text{Ca}$ background as functions of the He stripper pressure at SARA. As it was stated in chapter 2, the mass thickness is calculated assuming that the gas pressure in the stripper tube follows a triangular distribution.

theoretical optical loss cross section [Jacob et al., 2000].

The production term of the fitting curve is obtained assuming that, after each mass thickness differential $d\rho_A$, a differential of $(^{40}\text{CaF}_3)^-$ ions $-dN_- = \Sigma_p N_- d\rho_A$ are "stripped", producing a differential of $^{40}\text{Ca}^q$ ions $dN_q = \Phi_q \Sigma_p N_- d\rho_A$, this is,

$$\frac{dN_q}{d\rho_A} = \Phi_q \Sigma_p N_-(\rho_A) \quad : \quad N_-(\rho_A) = N_-^0 e^{-\Sigma_p \cdot \rho_A}. \quad (4.3)$$

In this case, N_-^0 would be the number of $(^{40}\text{CaF}_3)^-$ ions entering the stripper. The transmission of the charge state 2+ after a mass thickness ρ_A , not taking into account optical losses, would be then the $\frac{N_{2+}(\rho_A)}{N_-^0}$ ratio, which would be equal to the production term of Equation 4.2.

The optical losses have been assumed to be directly proportional to the mass thickness, as it was observed in simulations by Jacob et al. [2000]. A different possibility would be assuming that those losses also depend on the number of ions, so $dN_q = -\Sigma_m N_q d\rho_A$. Consequently, that term would be $e^{-\Sigma_m \cdot \rho_A}$. The linear term was used, instead of the exponential one, because of the better adjustment to the results. Nevertheless, the linear term is just the approximation of the exponential one for low mass thicknesses.

In both cases, only those results where the mass thickness was above $0.015 \mu\text{g}\cdot\text{cm}^{-2}$ were used during the fit. The reason is that the assumption of a triangular distribution of the He stripper pressure is not trustworthy at low pressures. For those data, the R^2 value of the fit was 0.992.

According to the fit, the charge state fraction of the 2+ state in He at ~ 400 keV is 55%, which means an optical loss of around a 25% of the $^{40}\text{Ca}^{2+}$ ions produced for the stripper gas pressure used in measurements.

4.2.2 3+ state

Figure 4.4 shows the relationship between stripper transmission and He mass thickness at SARA for the charge state 3+. Maximum transmissions around 20% are found for a He pressure in the range of 0.015-0.020 mbar. Klein et al. [2013] reports half that transmission, 11%, using Ar as stripping gas at the same energy. The charge state fraction calculated from the fit of this curve, equivalent to the one used for state 2+, is 30%.

Some presence of molecular background in charge state 3+ is typically observed in AMS measurements of actinides and ^{129}I [Gómez-Guzmán et al., 2012; Vockenhuber et al., 2013; Chamizo and López-Lora, in press]. Nevertheless, for an ion as light as $^{41}\text{Ca}^{2+}$, the electro-

static repulsion on molecular ions with the same mass and charge state 3+ would be more important. Tests with this charge state at SARA support this idea, with no changes in the $^{41}\text{M}/^{40}\text{Ca}$ ratios from blanks when the stripper pressure is decreased, even at 0.005 mbar.

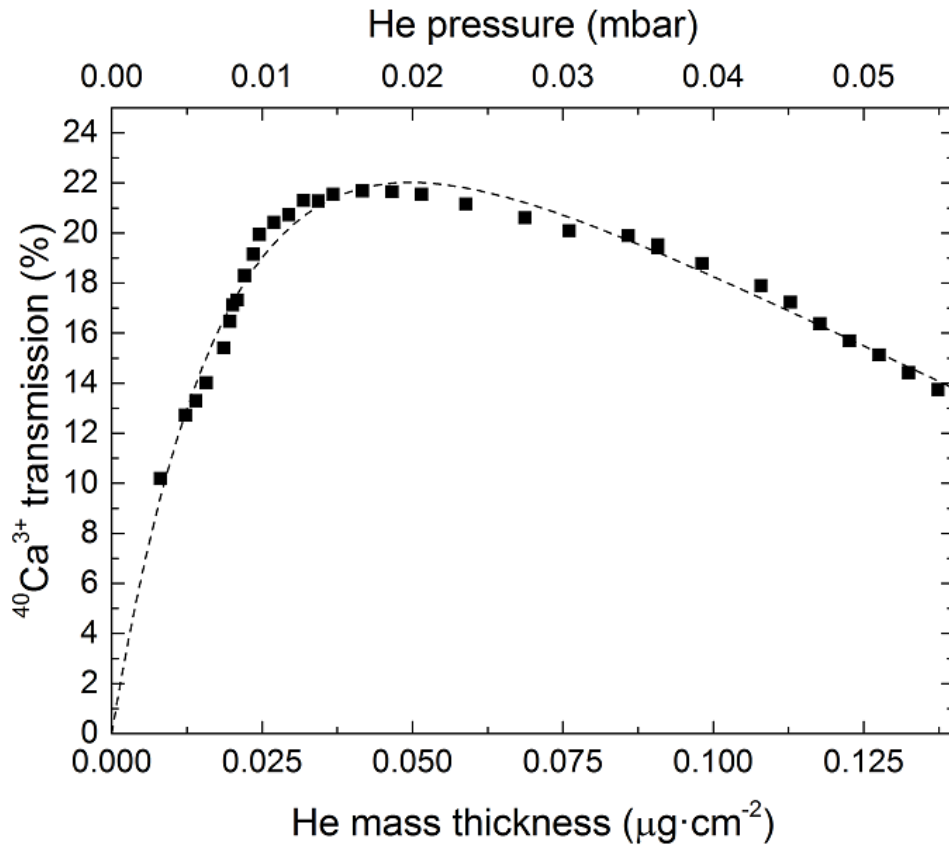


Figure 4.4: $^{40}\text{Ca}^{3+}$ transmission as a function of the He stripper pressure at SARA.

4.2.3 Charge state distribution

Besides 2+ and 3+, the transmission of the charge state 4+ was measured for a stripper pressure of 0.015 mbar. As expected, this transmission was very low, close to 2%. Assuming similar optical losses as those found for the other charge states, a charge state fraction of around 2.5% is found. The charge state fractions compared to those at TANDY, are presented in [Figure 4.5](#) (the fraction for the 4+ state here was assumed to be 0).

The Gaussian fit of these results gives mean charge states of 2.0 at 225 keV and 2.2 at 400 keV. The fit also predicts, in both cases, that the production of neutral species in the stripping with helium can be neglected. The application of this fit to the transmission results reported with argon suggest a much lower mean charge state of 1.4 at 400 keV [[Stocker et al., 2004](#)]. The

higher mean charge state with He as stripping gas for low energies agrees with which has been observed in uranium [Wittkower and Betz, 1973]. On the other hand, semi-empirical formulas applied to higher energies, like the one from Schiwietz and Grande [2001]³, predict the opposite: that, at large facilities, these mean charge states would be higher using Ar as stripping gas than using He. Therefore, it is clear that Schiwietz-Grande formula cannot be applied at low energies: for ^{40}Ca with an energy of 400 keV, the mean charge state according to this formula would be 0.9, less than the half of the one we calculate. Therefore, the measurements of this kind of parameters are truly important in order to provide data about the stripping process at low energies.

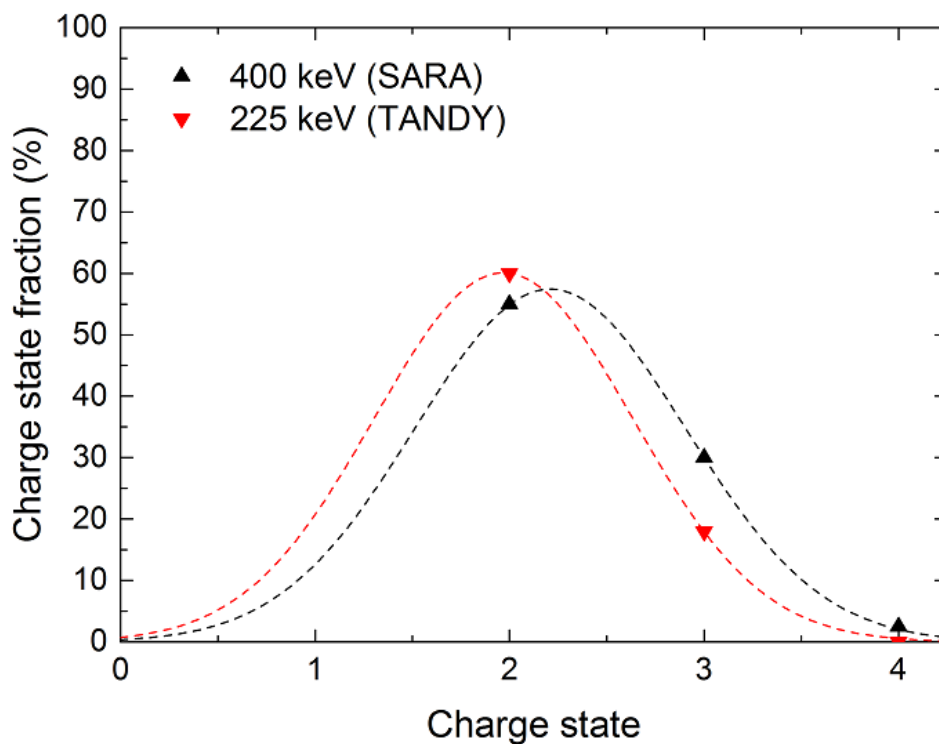


Figure 4.5: Charge state distribution for the $(^{40}\text{CaF}_3)^- \rightarrow ^{40}\text{Ca}^q$ stripping process in He at 225 keV and 400 keV. The charge state fraction of the 4+ state was supposed to be 0 at TANDY.

4.3 ^{40}Ca current measurement with the FC3 and ^{41}Ca detection with the compact GIC

A special feature of the ^{41}Ca measurements at SARA is that the measurement of the ^{40}Ca current with the FC3 cannot be performed when the accelerator terminal voltage is the same

³This formula can only be applied to ^{40}Ca with energies ≥ 800 keV.

4.3. ^{40}Ca CURRENT MEASUREMENT WITH THE FC3 AND ^{41}Ca CA DETECTION WITH THE COMPACT GIC

which is used when the ^{41}Ca is being detected with the GIC. The reason is the geometry of this FC. As it can be seen in Figure 4.6, the hole for ^{129}I measurements involves that, when the terminal voltage is tuned to detect ^{41}Ca in the GIC, part of the FC measuring ^{40}Ca current would block the way of ^{41}Ca ions to the ESA. Fortunately, this feature is no problem, since the FC can be placed where ^{40}Ca is deviated when ^{39}K is being detected. This way, ^{40}Ca current is measured during ^{39}K sequences, instead of during ^{41}Ca sequences. In order to get the $^{41}\text{Ca}/^{40}\text{Ca}$ ratios for each sequence, the ^{40}Ca current is supposed to be the average from those measured just before and just after that sequence.

As expected, the ^{41}Ca ΔE - E_{res} spectrum at the GIC when the 2+ state is selected in the HE side is very similar to the one at TANDY for the same charge state [Vockenhuber et al., 2015] being $^{82}\text{Se}^{4+}$ the only other ion reaching the detector. Figure 4.7 shows how, when the isobutane pressure is low enough to let the ^{41}Ca ions reach the second anode, the $^{82}\text{Se}^{4+}$ ions lose only a part of its kinetic energy in the gas, matching up with the spectrum predicted by SRIM simulations. Both signals can still be distinguished in the spectrum, but there exists a remote possibility of some ^{82}Se ions interfering with the ^{41}Ca signal.

Nevertheless, since at these energies the signals from ^{41}K and ^{41}Ca cannot be distinguished, there is no advantage in using this ΔE - E_{res} spectrum. In order to have a $^{82}\text{Se}^{4+}$ peak with well-defined energy, the gas pressure inside the GIC can be increased so that both ions are stopped before reaching the second anode. This way, the signal from the first anode would be directly related to the total energy with which these ions reach the detector. As it is shown in Figure 4.7, with this configuration, the $^{82}\text{Se}^{4+}$ peak presents a well-defined deposited energy of 2 times the energy of $^{41}\text{Ca}^{2+}$, as expected. This configuration is, therefore, the one used

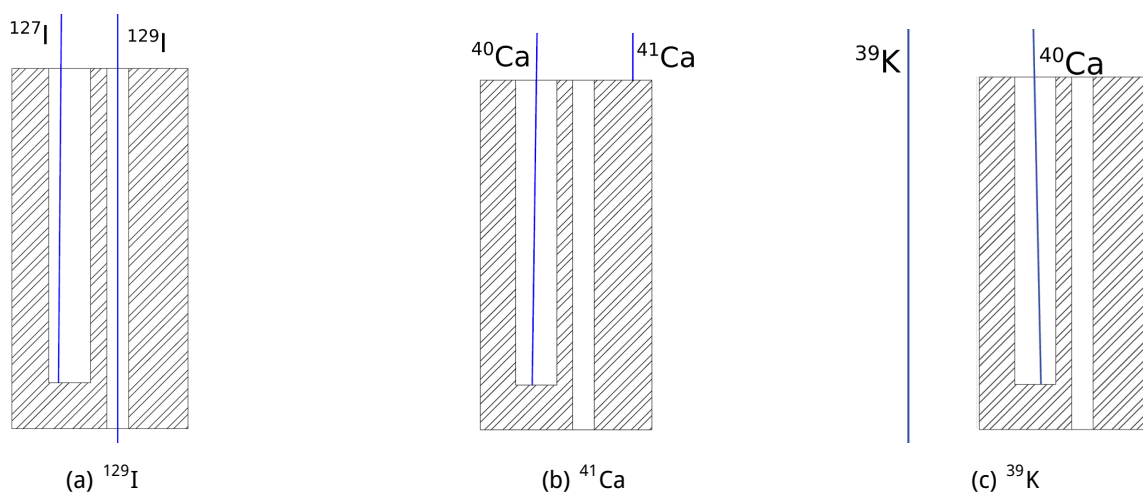


Figure 4.6: Relative position of the FC3 depending on the isotope whose current is measured and the radionuclide which is tuned to cross to the ESA.

during routine ^{41}Ca measurements at SARA.

The ^{41}Ca ΔE - E_{res} spectrum when the 3+ state is used (see Figure 4.8) does not present many of the peaks which can be seen at TANDY for that charge state, where ions with different $\frac{M}{q}$ ratio reach the detector because of the worse optical transport through the HE spectrometer. At SARA, only $^{82}\text{Se}^{6+}$ ions reach the detector with ^{41}Ca , as it happens when the state 2+ is used. The relative production of $^{82}\text{Se}^{6+}$ ions is much lower in this case, presumably because of a much lower stripper transmission for such a high charge state.

The integer $\frac{M}{q}$ ratio of the $^{39}\text{K}^{3+}$ ion implies the detection of several other ion species, being the most important of them $^{13}\text{C}^+$, $^{26}\text{Mg}^{2+}$ and, when copper target holders are used, $^{65}\text{Cu}^{5+}$. $^{13}\text{C}^+$ rates when sputtering a blank sample in copper targets are in the 1000-2000 s^{-1} range;

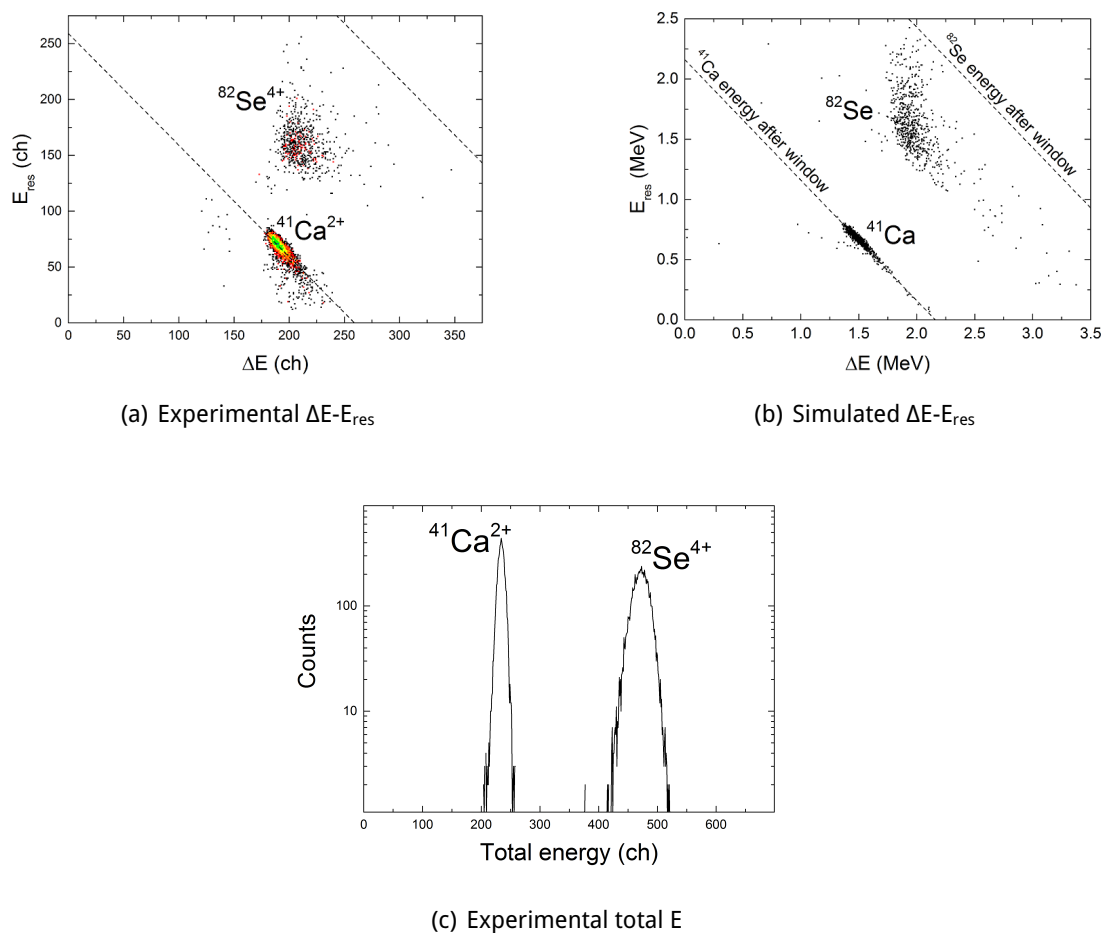


Figure 4.7: Experimental and simulated spectra for $^{41}\text{Ca}^{2+}$ and $^{82}\text{Se}^{4+}$ ions reaching the compact GIC at SARA. In the experimental ΔE - E_{res} spectrum, the dashed lines represent the average energy deposited by the ^{41}Ca ions, and twice that energy. In the SRIM simulation, each dot represents a single ion.

4.3. ^{40}Ca CURRENT MEASUREMENT WITH THE FC3 AND ^{41}Ca DETECTION WITH THE COMPACT GIC

this is several orders of magnitude below the $^{13}\text{C}^+$ found when trying to detect $^{26}\text{Al}^{2+}$ [Müller et al., 2015]. This is not totally unexpected, since the formation of negative ions where ^{13}C is present and with a mass of 96 u, when injecting $(^{39}\text{KF}_3)^-$, should not be as important as the formation of $(^{13}\text{C}_2)^-$ and $(^{12}\text{C}^{13}\text{CH})^-$ clusters, when injecting $^{26}\text{Al}^-$. $^{13}\text{C}^+$ and $^{26}\text{Mg}^{2+}$ when Al target holders were used were much higher, leading to important pile-up interfering with ^{39}K counting region.

The relationship between the total ^{41}M rate and the compact GIC efficiency has also been studied for charge state 2+, in order to provide a reliable maximum rate for the data analysis (see chapter 3). This was done by connecting a pulse generator to the detector, and comparing the measured rate from this pulse with its nominal value, previously measured with an oscilloscope. Figure 4.9 shows that, for ^{41}M rates lower than 1000 s^{-1} , the efficiency keeps higher than 90%. For higher rates, efficiency becomes inversely proportional to this ^{41}M rate.

It is convenient setting the maximum ^{41}M rate in $3000\text{--}5000\text{ s}^{-1}$, for instance, and using the pulse generator during the measurements to control the detector efficiency. This way, the efficiency will stay stable and higher than 80%, but it will be possible to measure $^{41}\text{Ca}/^{40}\text{Ca}$ ratios up to 10^{-8} even when the source output current is relatively high.

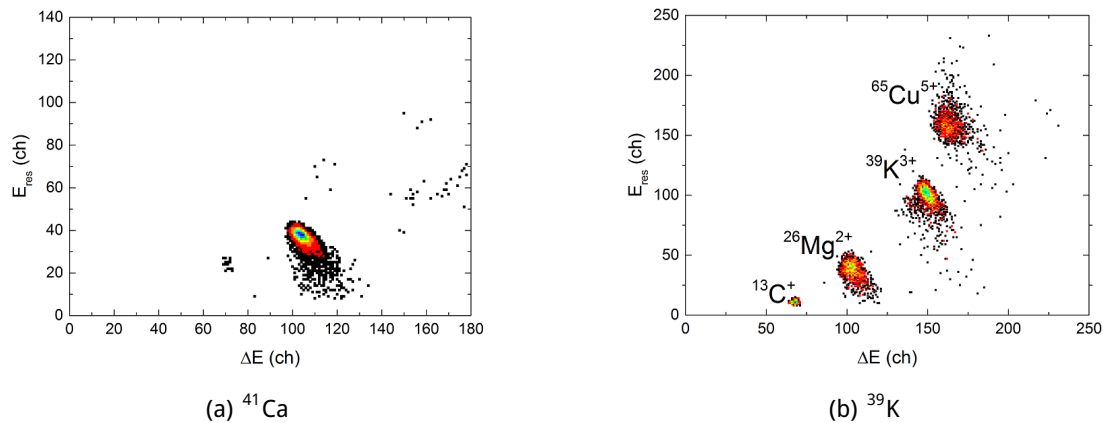


Figure 4.8: Experimental spectra for $^{41}\text{Ca}^{3+}$ and $^{39}\text{K}^{3+}$ ions reaching the compact GIC at SARA. Different amplifier gains were used during the acquisition of these spectra.

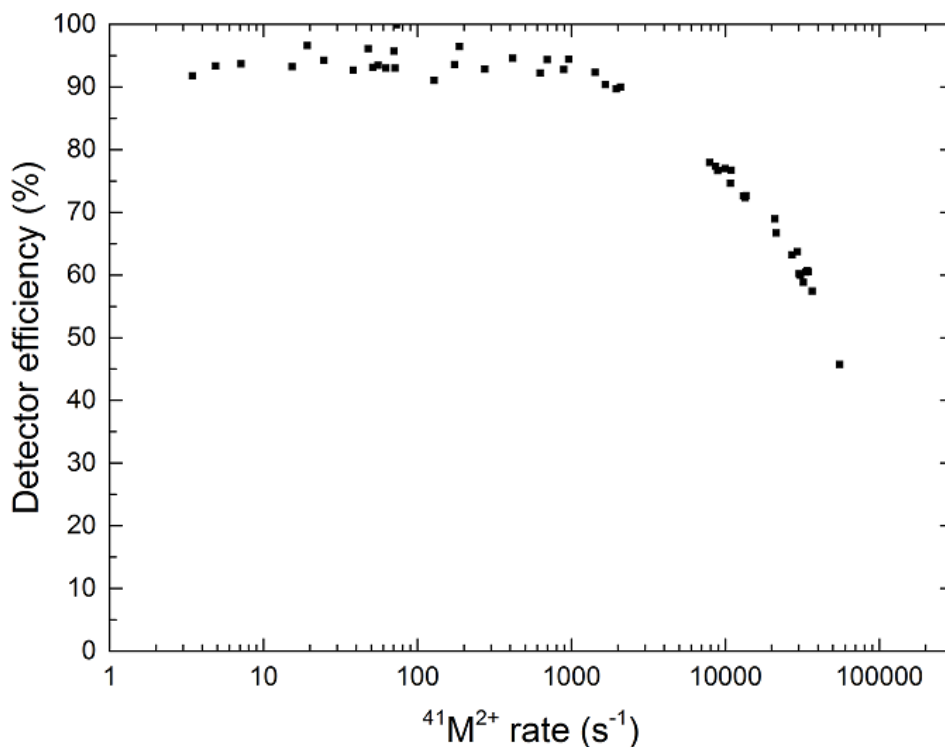


Figure 4.9: Relationship between the ^{41}M rate reaching the compact GIC and the detector efficiency. The ^{41}M rates presented have been already corrected dividing the measured rate by the efficiency.

4.4 K-correction and ^{41}Ca background

As it was stated in [chapter 3](#), the sequential detection of ions of two different masses, 41 and 39 u, requires the use of different terminal and ESA potentials. At SARA, the best way to do so is tuning, first, the voltages which would make ^{40}Ca ions reach the GIC, thanks to an insertable Faraday cup which can be placed just after the ESA (FC5). This also allows a better tuning of the other parameters, like the Q-Pole triplet voltage.

From these voltages, it is relatively easy to calculate the terminal voltage to make another ion have the same EM product so that it is selected by the HEM. Since the energy is changed, so has to be the ESA voltage. [Table 4.1](#) shows typical voltages used at SARA for ^{41}M and ^{39}K , based on the previous tuning of ^{40}Ca in the FC5.

One of the first studies at SARA of the relationship between the $^{41}\text{M}/^{40}\text{Ca}$ and $^{39}\text{K}/^{40}\text{Ca}$ ratios in blank samples is presented in [Figure 4.10](#). As it happened in this case, most of the ^{41}Ca measurements at SARA have shown a R^2 value higher than 0.9 in this linear regression, with a K-correction factor typically between 0.065 and 0.09, this is, around the natural $^{41}\text{K}/^{39}\text{K}$ ratio (0.0721).

The ⁴¹Ca/⁴⁰Ca background for the 2+ state, after applying the K-correction, is usually on the (2-8) × 10⁻¹² range, and only has been higher than 10⁻¹¹ when samples with ⁴¹Ca/⁴⁰Ca ratios higher than 10⁻⁸ have been measured. This background levels are similar to those found at TANDY. Since ⁴¹K interference is corrected, the main cause of this background, still much higher than those found in larger AMS facilities, would be the one produced by scattering processes

Table 4.1: Voltages at the accelerator terminal and the ESA in order to select different ions with the HE spectrometer at SARA.

Ion	⁴⁰ Ca	⁴¹ M	³⁹ K
LE side ion mass (u)	97	98	96
Bouncer magnet voltage (V)	0	-357	364
Terminal voltage (kV)	940	915	965
2+ energy (keV)	2280	2225	2335
2+ ESA voltage (kV)	44.7	43.6	45.9
3+ energy (keV)	3220	3140	3300
3+ ESA voltage (kV)	42.1	41.1	43.2

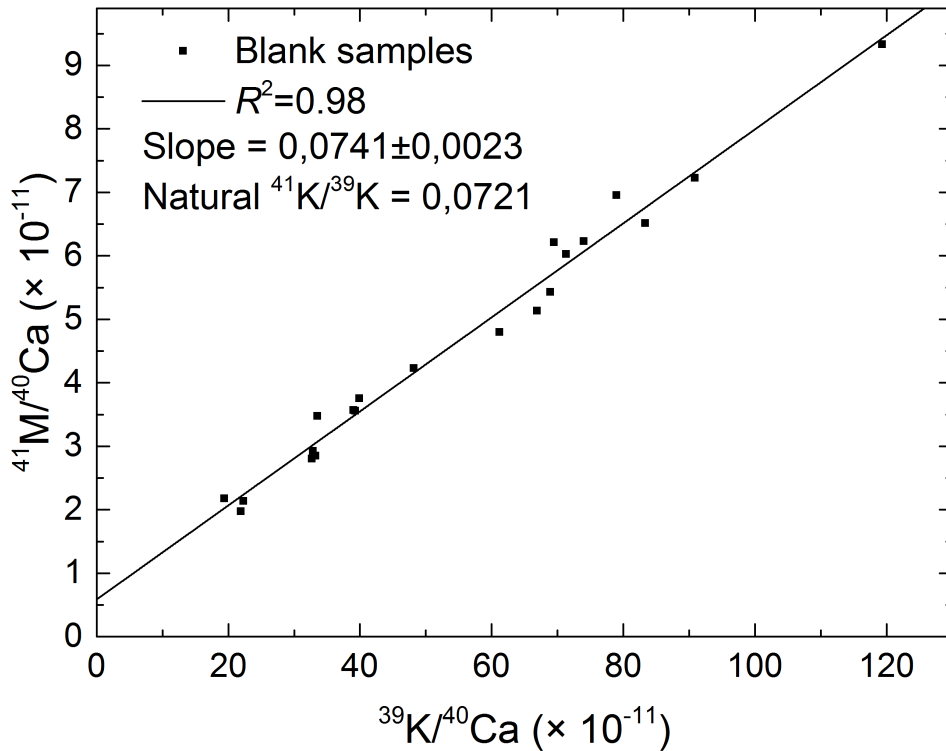


Figure 4.10: Linear correlation between the ⁴¹M/⁴⁰Ca and ³⁹K/⁴⁰Ca ratios in blank samples at SARA. 7 different blank samples were measured during 3 runs.

on residual gas, apertures, etc. This effect, which is increased because of the lower energies and the need of using higher stripper pressures to destroy the 2+ molecular background [Suter, 1998], takes also additional importance in ^{41}Ca measurements because of the high mass difference between the $(^{41}\text{CaF}_3)^-$ ion and ^{41}Ca . This fact makes easier the production of ions with mass 98 u where stable isotopes of calcium with masses close to 41 u, mainly ^{40}Ca and ^{42}Ca , are present. Theoretically, the cross section of this effect should be lower at SARA than at TANDY, because of the higher energy. However, at TANDY, the presence at the exit of the stripping tube of one of the pumps which recirculates the stripping gas could reduce the presence of residual gas in the HE acceleration tube, compensating the higher scattering cross section.

The $^{41}\text{Ca}/^{40}\text{Ca}$ background for the 3+ state has not been studied yet.

4.4.1 Tests with blank urine samples: radiochemical method

One of the applications where ^{41}Ca backgrounds found in low-energy AMS systems allow to perform measurements completely competitive with large facilities is the biomedical one. For instance, administrating oral doses of ^{41}Ca of 100 nCi (28.23 nmol), minimum urinary $^{41}\text{Ca}/^{40}\text{Ca}$ ratios⁴ are in the $5\text{-}10 \times 10^{-11}$ range [Denk et al., 2006, 2007]. As it was stated in chapter 1, such a dose can be considered radiologically exempt. Even studies where ^{41}Ca doses are one order of magnitude higher (and so would be $^{41}\text{Ca}/^{40}\text{Ca}$ ratios) are still considered to have no radiological hazard [Weaver et al., 2009], since the dose over 50 years would be $10 \mu\text{Sv}$ ⁵ [ICRP, 2012].

The capabilities of the SARA system to measure this kind of samples was tested in an inter-comparison measurement with the TANDY system (see section 4.6). These samples were sent to the ETH LIP in CaF_2 form by the NutriTrace group at the National University of Singapore. Nevertheless, in order to be able to perform ^{41}Ca measurements for biomedical groups at CNA, including the chemical preparation of the samples in our service, chemical preparation tests with blank urine samples have been performed.

The chemical procedure was based on those presented on the bibliography [Freeman et al., 1995; Miller et al., 2013; Jackson et al., 2013], but with two important changes: the initial precipitation of calcium carbonate instead of calcium oxalate; and the omission of the use of ion-exchange resins. The use of calcium carbonate avoids the presence of this salt in the final

⁴Urine samples are the most common biomedical samples use to control the changes of the ^{41}Ca concentration in the extracellular fluids on this kind of studies.

⁵The yearly background dose because of natural sources is typically higher than 1 mSv.

CaF₂ precipitate, since the carbonate ion is destroyed if the salt is dissolved in an acid⁶. The ion-exchange step was discarded because our tests with carbonate samples did not show a clear reduction of the final ³⁹K/⁴⁰Ca ratios. The time consumption and sample loss because of this process are, therefore, not worthy.

The steps of the first part of our chemical procedure, the calcium carbonate isolation (see Figure 4.11), designed for 24 h samples and tested with 1 l collections from volunteers⁷, are:

1. Addition, per 100 ml urine, of 5 ml of concentrated HCl and settling of the solution for 1 h.
2. Decanting of the supernatant in a 2 l (or larger) beaker and addition of concentrated NH₃ until pH=11.
3. Addition, per 100 ml urine, of 10 ml Na₂CO₃ solution (0.4 g/ml), heated until it almost boils.
4. Settling of the beaker overnight with some inclination. It is also possible to let the beaker upright, but heating without boiling to take advantage of the indirect relationship between temperature and the solubility of calcium carbonate⁸.
5. Discarding of most of the supernatant and transfer of the rest, together with the precipitate, to 50 ml centrifuge tubes.
6. Centrifugation and discarding of the supernatant. Transfer precipitates to an unique 50 ml centrifuge tube per sample.

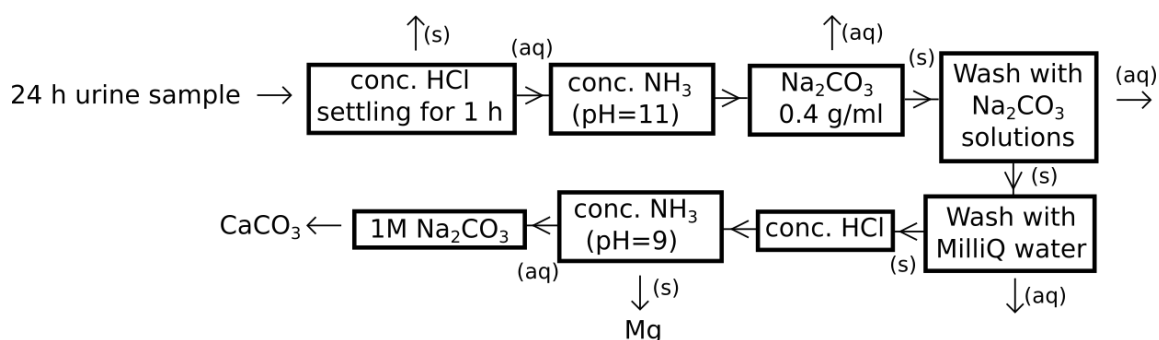


Figure 4.11: Scheme of the calcium isolation method for urine samples.

⁶ $(\text{CO}_3)^{2-} + 2 \text{H}^+ \longrightarrow \text{CO}_2 + \text{H}_2\text{O}$

⁷Since these volunteers were not dosed with ⁴¹Ca these samples are considered blanks.

⁸This also avoids the presence of other calcium salts since, unlike calcium carbonate, most of the compounds present a direct relationship between temperature and solubility.

7. Washing with 20 ml saturated Na_2CO_3 solution (0.2 g/ml). Centrifugation and discarding of the supernatant. This step should be performed twice.
8. Washing with 20 ml Na_2CO_3 solution (0.02 g/ml). Centrifugation and discarding of the supernatant. This step should be performed twice.
9. Washing with 20 ml of MilliQ water. Centrifugation and discarding of the supernatant.
10. Dissolving of the precipitate with 5 ml of concentrated HCl.
11. Addition of concentrated NH_3 until pH=9.
12. Centrifugation and discarding of the precipitate (mostly magnesium hydroxide).
13. Addition of some drops of concentrated Na_2CO_3 solution (0.2 g/ml).
14. Centrifugation and discarding of the supernatant.
15. Washing with acetone.
16. Centrifugation and discarding of the supernatant.
17. Drying at 70 °C for 1 h.

The CaF_2 precipitation part is a much more simple procedure. The carbonate is dissolved with 1 M HCl, and just some drops of concentrated HF are necessary to precipitate the calcium fluoride. After centrifuging and discarding the supernatant, the precipitate is washed with MilliQ water. Then, the centrifugation and discarding of the supernatant is repeated. The final precipitate is dried at 105 °C overnight.

K-corrected $^{41}\text{Ca}/^{40}\text{Ca}$ ratios from these blank urine samples was equivalent to those found in our typical blank samples, around 5×10^{-12} . This agrees with the fact that, in large facilities where background levels are in the 10^{-15} - 10^{-14} , the $^{41}\text{Ca}/^{40}\text{Ca}$ ratio from processed urine blanks is typically lower than 5×10^{-13} [Jackson et al., 2013], one order of magnitude lower than our background values.

During this thesis, we have been in contact with several biomedical groups from different universities in Spain in order to perform these kind of ^{41}Ca measurements. Unfortunately, these contacts were not successful. Nevertheless, our system is totally capable of performing the measurements in the case that any group is interested in the future.

4.5 Measurement of the HE side optical transmission with standard samples

The presence of a quadrupole triplet at the exit of the 1 MV tandetron allows an optimal optical focusing no matter the effective charge state $q^* \equiv \frac{M_0}{M} q$ of the ions (see [chapter 2](#)). This is one of the most important differences of SARA with the TANDY system at [ETH LIP](#) for ^{41}Ca [AMS](#). The non-optimal optical behaviour of ^{41}Ca through the [HE](#) side spectrometer at TANDY implies optical losses of, at least, 15% for the charge state 2+, and 33% for the charge state 3+ [[Christl et al., 2013](#); [Vockenhuber et al., 2015](#)].

At SARA, therefore, there should exist an improvement on this transmission relative to the one at TANDY, and no such a dependency on the charge state. An approximation to this optical transmission can be obtained by checking the measured $^{41}\text{Ca}/^{40}\text{Ca}$ ratios from the standard samples, provided that the detector efficiency is corrected. At SARA, this study has only been performed, yet, with the 2+ state.

The AE701 standards from the Institute for Reference Materials and Measurements (IRMM) of the European Commission's Joint Research Centre [[Hennessy et al., 2005](#)] have been used for standard correction in ^{41}Ca measurements at SARA during this thesis. Minimum measured/nominal $^{41}\text{Ca}/^{40}\text{Ca}$ ratios higher than 80% were typically consequence of slight changes in the terminal voltages, while the optimal conditions lead to measured/nominal relationship even higher than 99%. Taking, for instance, all the ^{41}Ca measurements performed during the year 2017, the average of this measured/nominal factor is $(93.8 \pm 5.5)\%$, using the standard deviation as uncertainty.

[Table 4.2](#) shows an example of the blank corrected $^{41}\text{Ca}/^{40}\text{Ca}$ ratios from each of the 3 standards used during one of our ^{41}Ca measurements at SARA; this is, the $^{41}\text{Ca}/^{40}\text{Ca}$ ratios calculated in order to perform the standard correction (see [chapter 3](#)) During this measurement, 2 cathodes from each standard material were measured.

The optical transmission for the 3+ state has not been studied yet.

Table 4.2: Blank corrected $^{41}\text{Ca}/^{40}\text{Ca}$ ratios of the standard samples used in one of the ^{41}Ca measurements at SARA using the 2+ state.

Standard	Nominal $^{41}\text{Ca}/^{40}\text{Ca}$	Measured $^{41}\text{Ca}/^{40}\text{Ca}$	Measured/nominal (%)
AE701/3	$(1.0181 \pm 0.0069) \times 10^{-8}$	$(0.988 \pm 0.019) \times 10^{-8}$	97.0 ± 2.0
AE701/4	$(1.0479 \pm 0.0071) \times 10^{-9}$	$(1.029 \pm 0.049) \times 10^{-9}$	98.2 ± 4.8
AE701/5	$(1.0520 \pm 0.0071) \times 10^{-10}$	$(1.000 \pm 0.013) \times 10^{-10}$	95.1 ± 1.5

4.6 Comparison measurements with TANDY

4.6.1 Performance parameters

Table 4.3 presents the performance parameters from both systems for ^{41}Ca AMS. Using the charge state 2+, the lower stripper transmission at SARA is compensated by the higher optical transmission through the HE side spectrometer. Taking into account the similar background levels, the most significant difference in the performance of ^{41}Ca measurements between both systems relies in the $(^{40}\text{CaF}_3)^-$ current output from the ion source. In any case, the capabilities of SARA for ^{41}Ca measurements are totally equivalent to those of TANDY.

The $^{41}\text{Ca}/^{40}\text{Ca}$ background when the 3+ state is used has not been studied yet. The optical transmission through the HE spectrometer should be similar to the one of 2+ state. This is caused by the presence of the Q-Pole triplet at the exit of the accelerator which eliminates the dependency of the object point of the HE spectrometer on the charge state. At TANDY, where the 3+ optical transmission does not reach the 66% and the stripper transmission is much lower (15%) than the transmission for state 2+ (50%) [Christl et al., 2013; Vockenhuber et al., 2015], the use of this charge state would mean a reduction of the overall efficiency of a factor 4 in comparison with the state 2+.

Table 4.3: Comparison of the ^{41}Ca performance parameters at SARA and TANDY. Data from TANDY are gathered from Vockenhuber et al. [2015] and the measurements performed during the stay of four months at ETH LIP.

Facility	SARA	TANDY
$(^{40}\text{CaF}_3)^-$ current (nA)	50-150	100-200
HE side charge state	2+ 3+	2+
He stripper transmission	40	20 50
HE side optical transmission	90-100	— 80-85
$^{41}\text{Ca}/^{40}\text{Ca}$ background ($\times 10^{-12}$)	2-8	— 2-8

4.6.2 Measurement of ETH in-house standards

One of the measurements performed at SARA to compare its performance with that at TANDY was carried out with two of the ETH in-house ^{41}Ca standards: B8 and B10. Additional information about these standards is presented in Christl et al. [2013] and Vockenhuber et al. [2015]. The samples were received already mixed with silver in a $\text{CaF}_2:\text{Ag}$ weight ratio of 1:10, so the ion source output was not optimal. The measurements were performed using the IRMM ref-

reference materials AE701/3, AE701/4 and AE701/5 (see [section 4.5](#)) for the standard correction, and performing all the analysis and corrections as for samples of unknown $^{41}\text{Ca}/^{40}\text{Ca}$ ratios (K-correction, blank correction...).

From each one of these standards, 3 cathodes were pressed and measured at SARA. For one of the cathodes from the B10 standard no run passed two of the discard criteria used: the minimum ^{40}Ca current and the maximum $^{39}\text{K}/^{40}\text{Ca}$ ratio. The results from the rest of the cathodes, shown in [Table 4.4](#), did not differ from the nominal value more than a 5.5%. However, these results at SARA are systematically higher than the nominal values, obtained from different measurements performed with both, TANDY and the 6 MV tandem at ETH⁹.

4.6.3 Intercomparison with biomedical samples

As it was stated in [chapter 1](#), the most important ^{41}Ca application nowadays is its use as a tracer of the calcium metabolism. ^{41}Ca doses well below exemption levels, administered either orally or by intravenous route, are enough to produce $^{41}\text{Ca}/^{40}\text{Ca}$ ratios in different body fluids which can be measured by AMS. Most of the studies with human subjects nowadays use the urinary $^{41}\text{Ca}/^{40}\text{Ca}$ ratio in order to measure changes in ^{41}Ca concentration in the extracellular fluids (ECF), since total calcium concentration is constant in these fluids, and they have the same $^{41}\text{Ca}/^{40}\text{Ca}$ ratio as the urine. Since ^{41}Ca is first incorporated by the ECF, initial urinary $^{41}\text{Ca}/^{40}\text{Ca}$ ratio is relatively high. The incorporation of this ^{41}Ca to the bone produces a decrease of the urinary $^{41}\text{Ca}/^{40}\text{Ca}$ ratio until it reaches an equilibrium in the ^{41}Ca exchange between the ECF and the bone (with a slow decrease because of the excretion), and different interventions against calcium resorption can then be tested. If those interventions are successful, the urinary $^{41}\text{Ca}/^{40}\text{Ca}$ ratio decreases significantly because of the ^{41}Ca absorption by the bone. [Denk et al. \[2006\]](#) present the experimental data when oral ^{41}Ca doses of 3700 Bq are administered to different subjects. Initial urinary $^{41}\text{Ca}/^{40}\text{Ca}$ ratios are close to 10^{-7} , while

Table 4.4: Measurement of the ETH in-house ^{41}Ca standards B10 and B8 at SARA.

ETH standard	Nominal $^{41}\text{Ca}/^{40}\text{Ca}$	Cathode	$^{41}\text{Ca}/^{40}\text{Ca}$ at SARA
B10	$(4.200 \pm 0.042) \times 10^{-10}$	ETH-B10a	$(4.20 \pm 0.33) \times 10^{-10}$
		ETH-B10c	$(4.43 \pm 0.23) \times 10^{-10}$
B8	$(4.000 \pm 0.040) \times 10^{-8}$	ETH-B8a	$(4.06 \pm 0.18) \times 10^{-8}$
		ETH-B8b	$(4.06 \pm 0.18) \times 10^{-8}$
		ETH-B8c	$(4.17 \pm 0.20) \times 10^{-8}$

⁹The measurements at the 6 MV tandem were performed using calcium hydride instead of fluoride.

equilibrium levels are in the 10^{-10} level.

One of the main goals during the stay at [ETH LIP](#) was the collaboration with the group in the ^{41}Ca measurements which they perform for the NutriTrace group at the National University of Singapore (NUS). A total of 111 samples were measured at TANDY. The urine samples, collected from 10 different subjects at different days after the ^{41}Ca oral administration, were chemically treated at [NUS](#) and sent to Zurich in CaF_2 form.

40 samples from 7 subjects were chosen to be measured also at SARA. While, at TANDY, the ETH in-house standards B9, B10 and B11¹⁰ were used for the standard corrections, at SARA, we used the IRMM standards AE701/3, AE701/4 and AE701/5. At both systems, the data analysis was equivalent, following the procedure described in [chapter 3](#). 6 samples could not be measured, since they did not pass the discard criteria; in most of the cases, that was due to high $^{39}\text{K}/^{40}\text{Ca}$ ratios. The results for the rest of the samples, compared to the results at TANDY, are presented in [Figure 4.12](#). Results at SARA are higher by a 7%, which is consistent with the different standards used in both labs, since, as it was shown in previous subsection, the $^{41}\text{Ca}/^{40}\text{Ca}$ ratios from the ETH standards, measured at SARA, are also higher than the nominal values reported by the [ETH LIP](#).

The figures presented in next pages show these results as a function of the time after the ^{41}Ca administration, including, also, the measurements at TANDY from those samples which were not measured at SARA. It can be seen that this little difference is not enough to make our results not fitting with the tendency. This is a clear indication of the suitability of the SARA system to perform ^{41}Ca measurements for biomedical applications. These figures clearly present the decrease on the $^{41}\text{Ca}/^{40}\text{Ca}$ ratio due to the ^{41}Ca incorporation to the bone.

¹⁰The respective nominal $^{41}\text{Ca}/^{40}\text{Ca}$ ratios from these standards are $(4.119 \pm 0.041) \times 10^{-9}$, $(4.200 \pm 0.042) \times 10^{-10}$ and $(4.160 \pm 0.042) \times 10^{-11}$ [[Christl et al., 2013](#)].

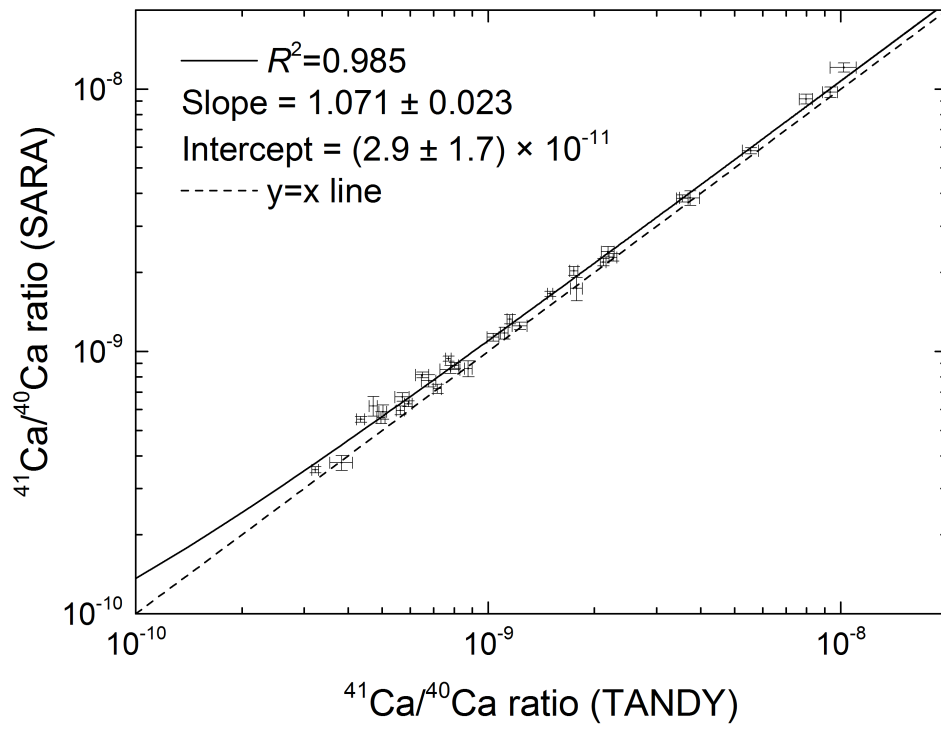


Figure 4.12: Comparison of the $^{41}\text{Ca}/^{40}\text{Ca}$ ratios from the biomedical samples at TANDY and SARA.

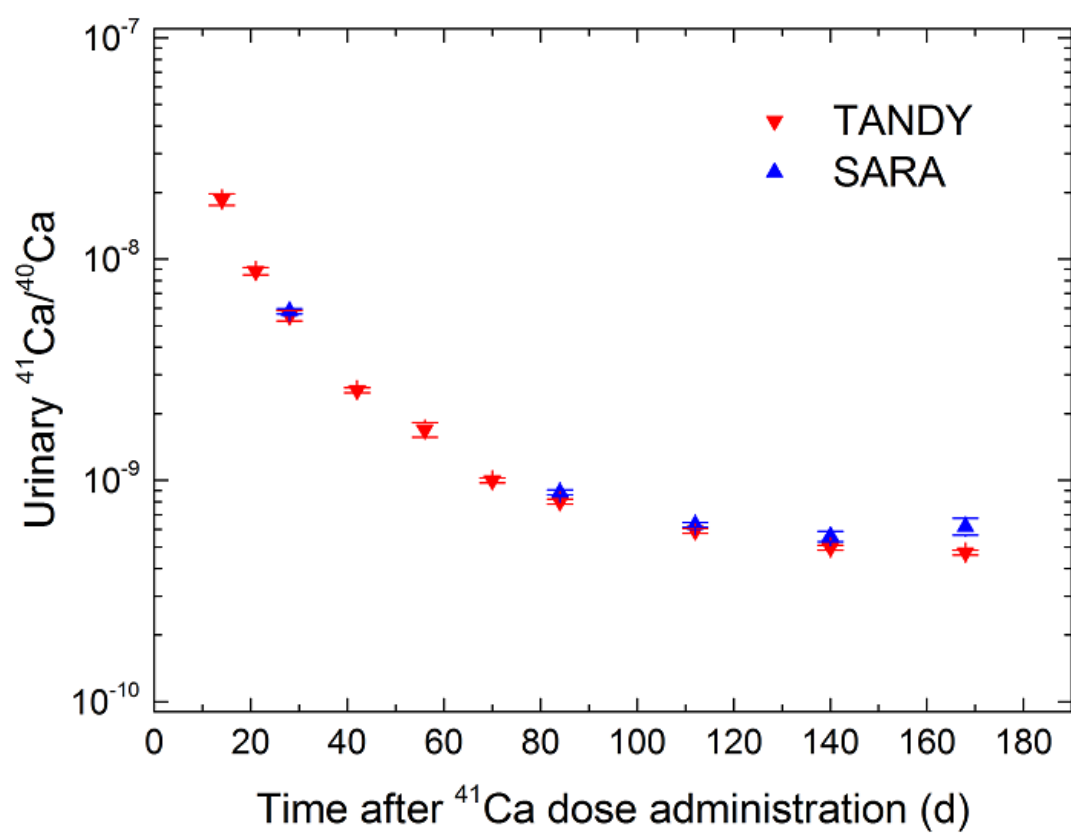


Figure 4.13: Temporal evolution of the urinary $^{41}\text{Ca}/^{40}\text{Ca}$ ratio in subject 4, including measurements at TANDY and SARA.

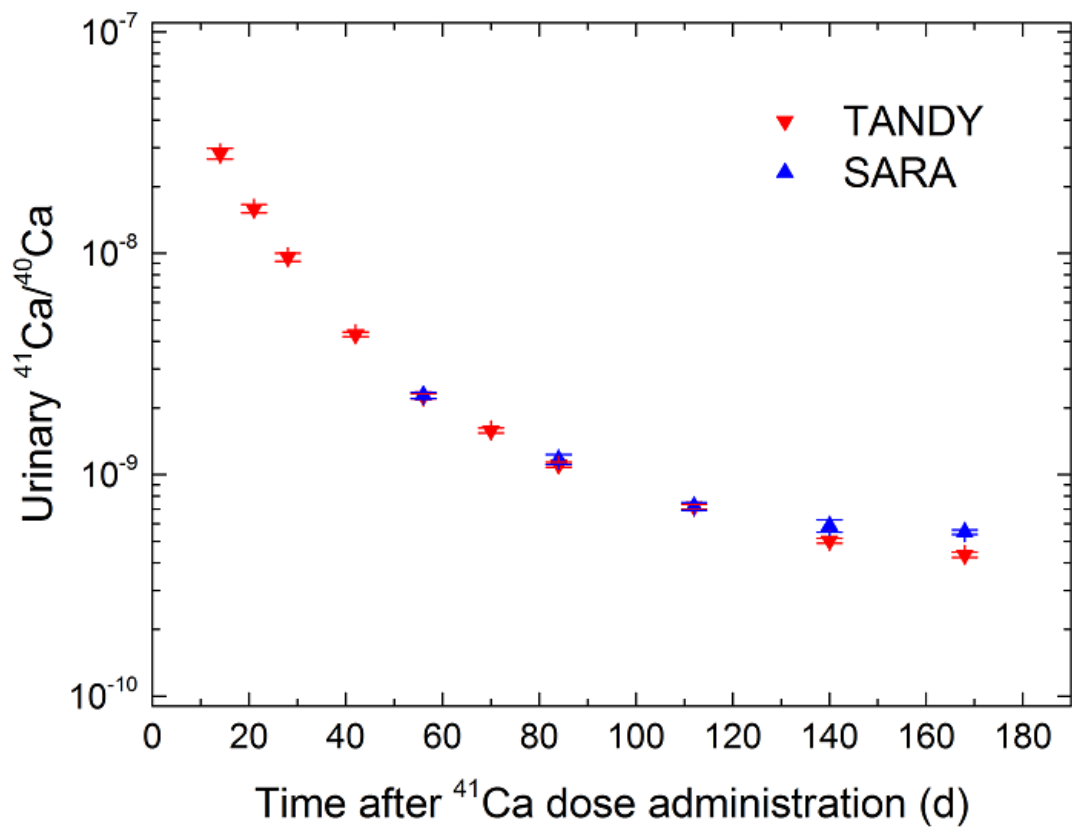


Figure 4.14: Temporal evolution of the urinary $^{41}\text{Ca}/^{40}\text{Ca}$ ratio in subject 5, including measurements at TANDY and SARA.

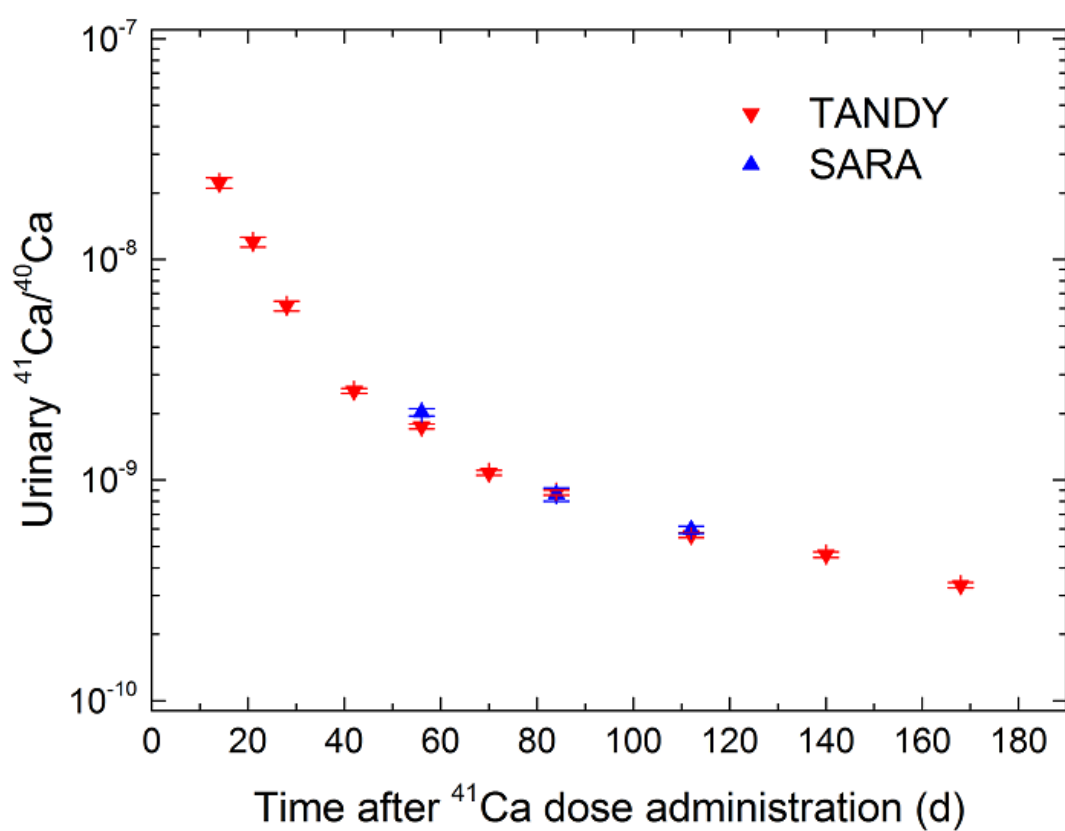


Figure 4.15: Temporal evolution of the urinary $^{41}\text{Ca}/^{40}\text{Ca}$ ratio in subject 6, including measurements at TANDY and SARA.

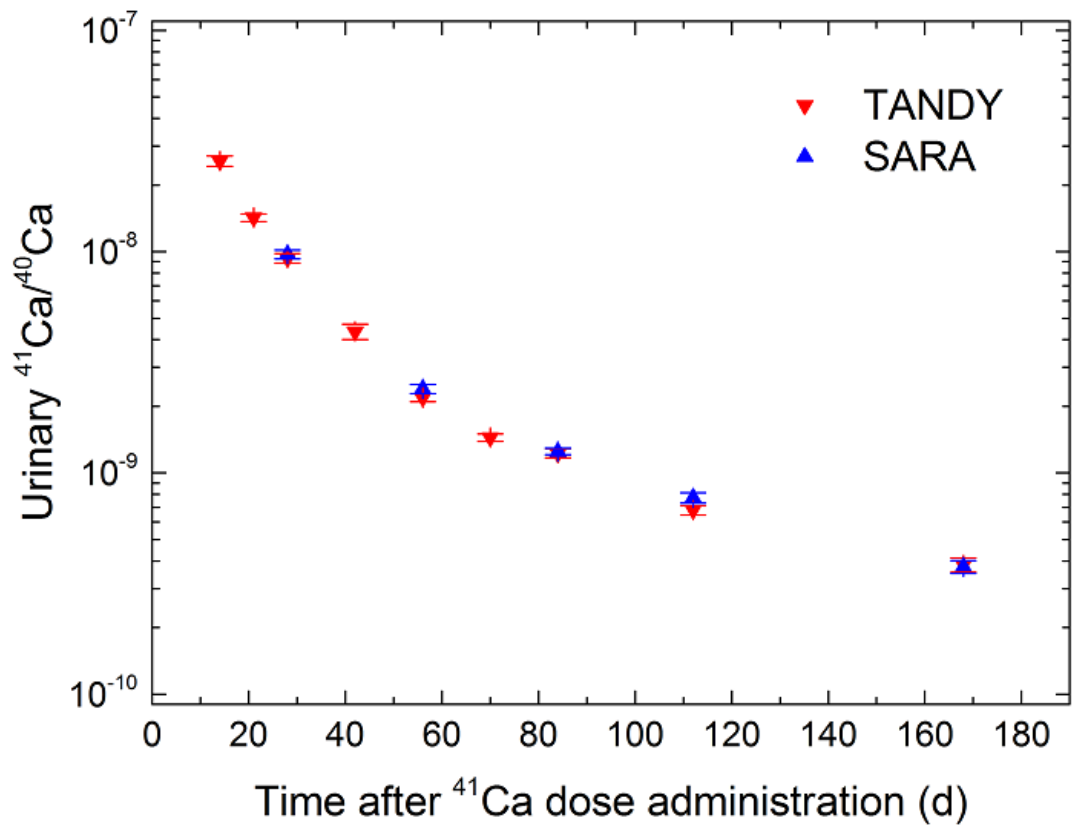


Figure 4.16: Temporal evolution of the urinary $^{41}\text{Ca}/^{40}\text{Ca}$ ratio in subject 7, including measurements at TANDY and SARA.

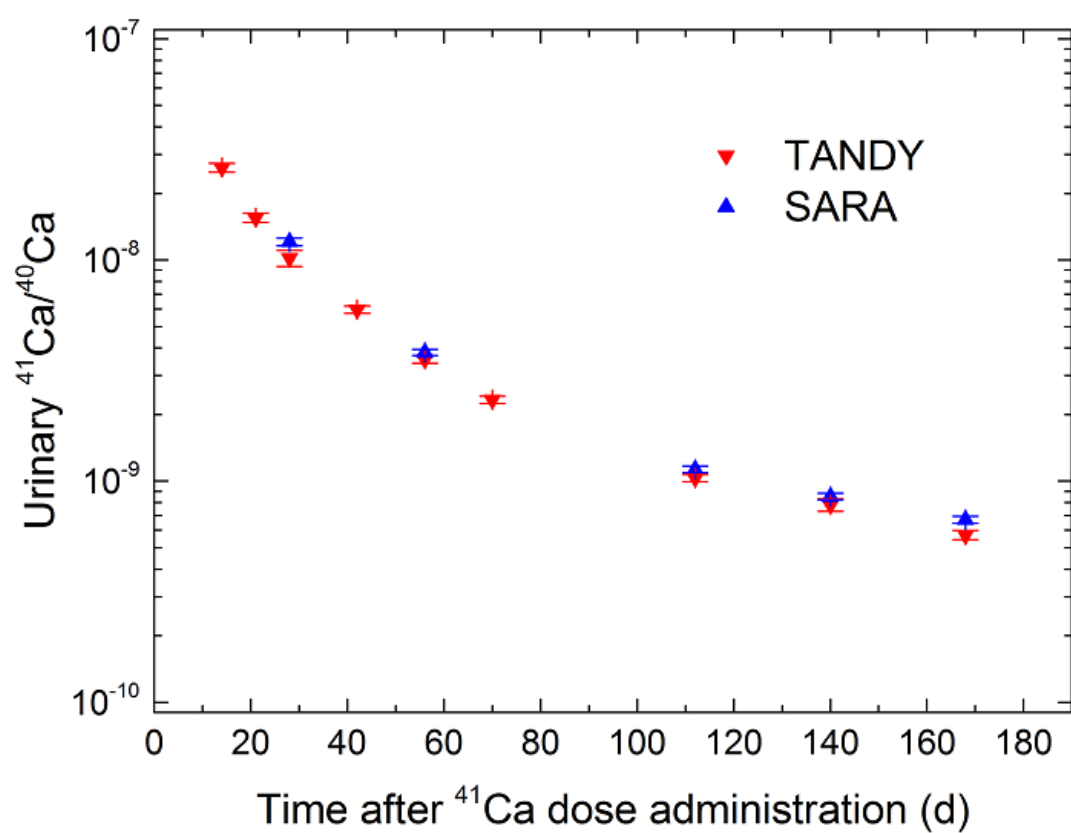


Figure 4.17: Temporal evolution of the urinary $^{41}\text{Ca}/^{40}\text{Ca}$ ratio in subject 8, including measurements at TANDY and SARA.

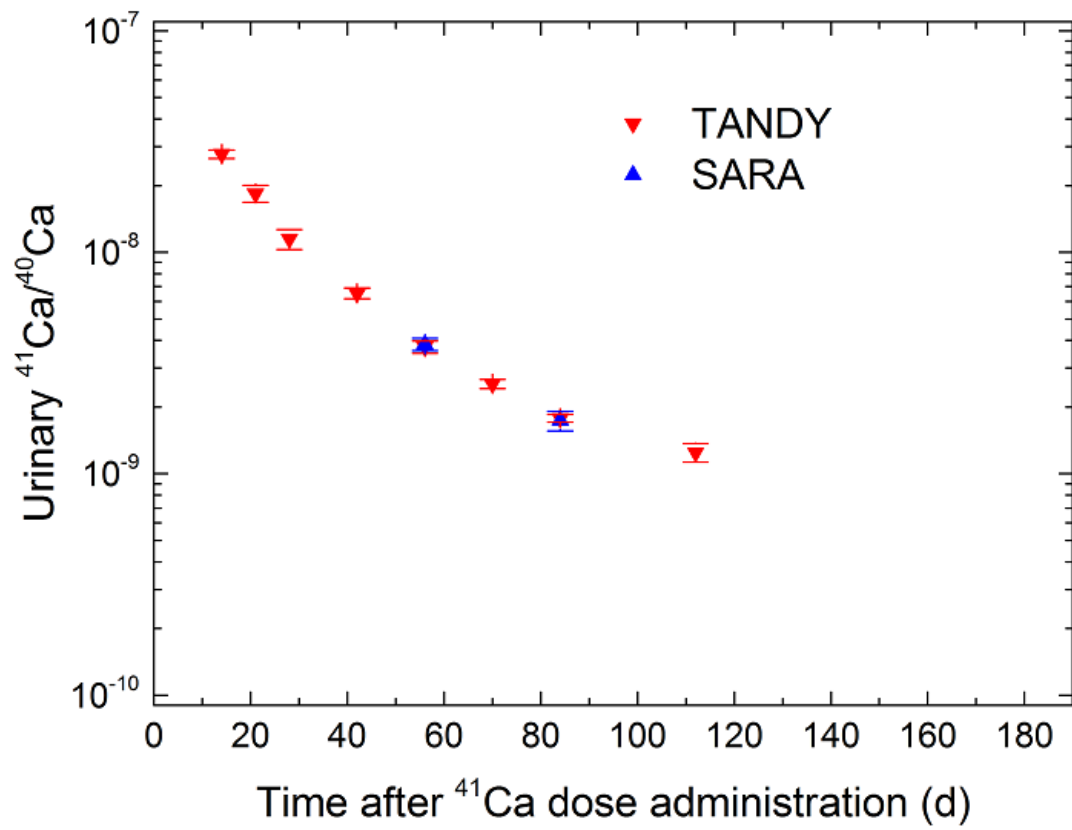


Figure 4.18: Temporal evolution of the urinary $^{41}\text{Ca}/^{40}\text{Ca}$ ratio in subject 9, including measurements at TANDY and SARA.

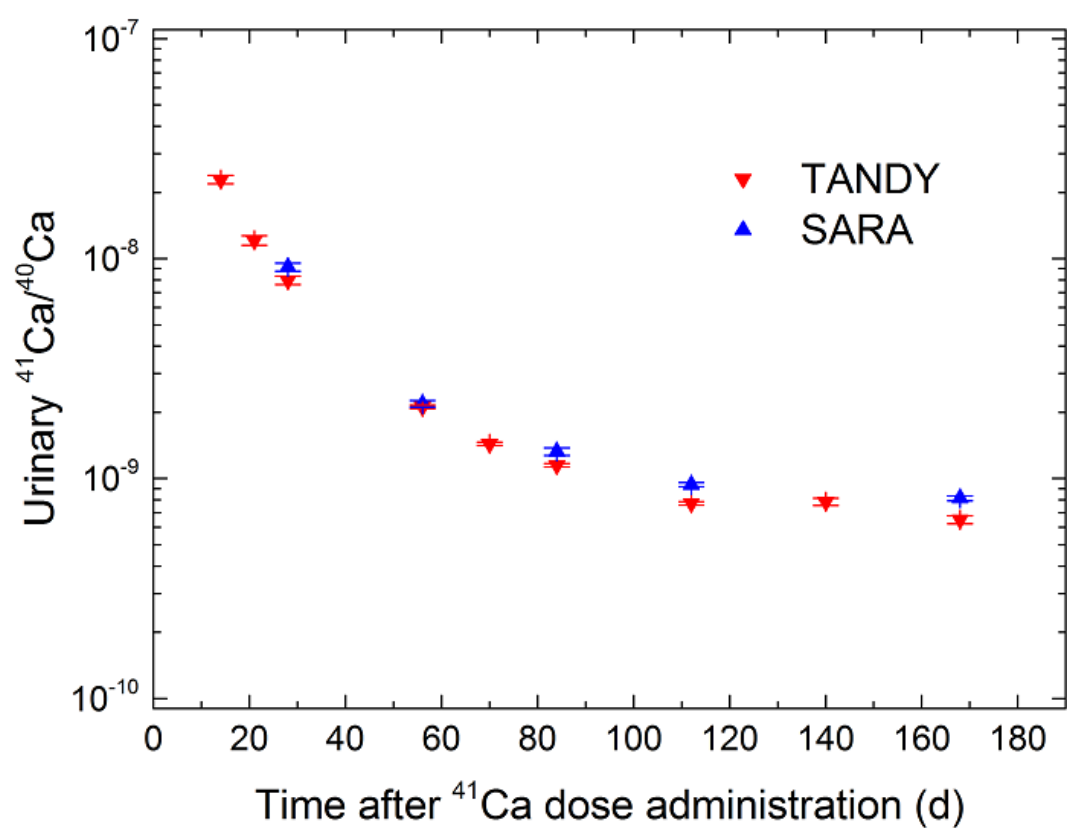


Figure 4.19: Temporal evolution of the urinary $^{41}\text{Ca}/^{40}\text{Ca}$ ratio in subject 10, including measurements at TANDY and SARA.

Chapter 5

^{41}Ca measurement in concrete samples from the bioshield of a nuclear power plant

Previous chapters are dedicated to the technical aspects of the ^{41}Ca AMS measurements. This last chapter is dedicated to the first application performed at CNA Seville of the ^{41}Ca measurements: the characterization of concrete samples from the bioshield of a NPP for the Spanish radioactive waste management agency, ENRESA.

The direct relationship between the $^{41}\text{Ca}/^{40}\text{Ca}$ ratio in the concrete bioshield and the thermal neutron fluence is explained in [section 5.1](#). Most of the information from this section is based on Chapter 3 of [Lewis \[2008\]](#).

The samples had to be chemically treated in order to have the CaF_2 to be measured by AMS. The chemical method developed for that, and applied to all the samples measured, is detailed in [section 5.2](#).

The final description of the samples and the results obtained are shown in [section 5.3](#).

5.1 Production of ^{41}Ca in the concrete bioshield of nuclear reactors

^{41}Ca is produced in the concrete bioshield of nuclear reactors by the neutron activation of its stable isotope, ^{40}Ca . The energy spectrum from these neutrons reaching the shield presents

two main groups:

- Fast neutrons (energies in the 1 MeV range) produced after the fission processes which escape the reactor vessel before being thermalized by the reactor moderator.
- Thermal neutrons (energies much lower than 1 eV) from the moderation of the neutrons produced in the fission which escape the reactor vessel before either producing a new fission reaction, or being absorbed by another material within the vessel (control rods, walls, etc.).

Nevertheless, the production of ^{41}Ca by fast neutron capture can be disregarded since, as it can be seen in Figure 5.1, the cross section of the $^{40}\text{Ca}(n,\gamma)$ reaction is around 2 orders of magnitude lower for these neutrons than for thermal energies. In fact, the main contribution of fast neutrons to the production of ^{41}Ca would come from its moderation in the concrete material itself, due to the elastic scattering processes with the hydrogen present on it. This way, it can be supposed that ^{41}Ca is entirely produced by the thermal neutron capture of ^{40}Ca , being these either original thermal neutrons reaching the shield, or fast neutrons which have been thermalized by the material. The elastic scattering not only thermalize the neutrons to room temperature, but also causes a diffusion of the thermal neutrons.

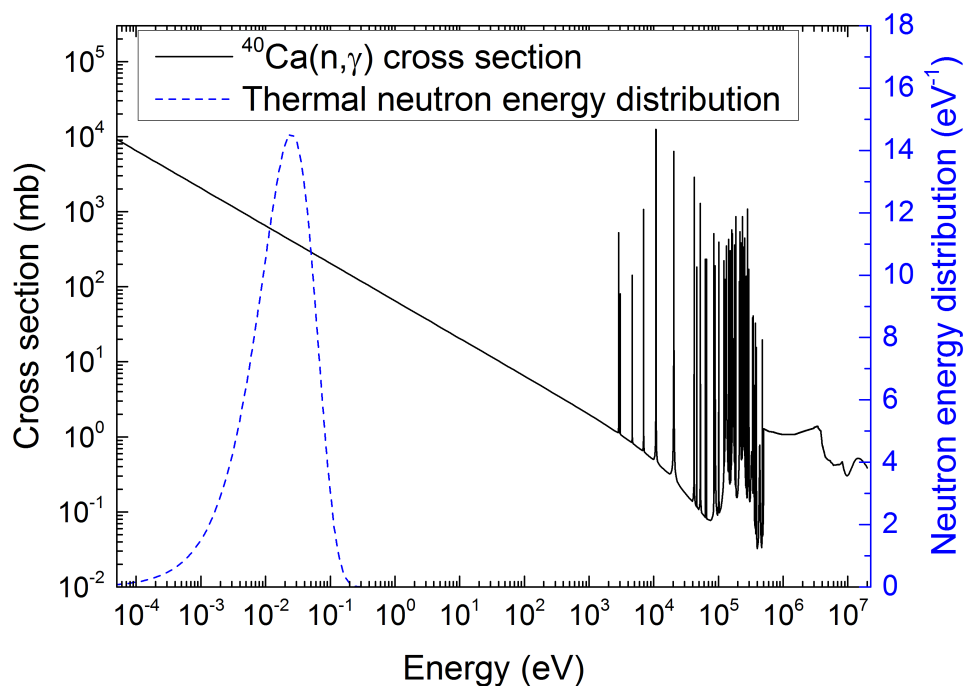


Figure 5.1: ^{40}Ca neutron capture cross section and thermal neutron energy distribution. Cross section data from IAEA [n.d.].

The $^{41}\text{Ca}/^{40}\text{Ca}$ ratio in any location of the shield, therefore, would be

$$^{41}\text{Ca}/^{40}\text{Ca} = \int_0^\infty \sigma(E) \frac{d\Phi(E)}{dE} dE, \quad (5.1)$$

where $\sigma(E)$ is the $^{40}\text{Ca}(n,\gamma)$ cross section as a function of the energy, and $\frac{d\Phi(E)}{dE}$ is the energy distribution of the neutron fluence. The energy distribution of thermal neutrons can be considered to be Maxwellian, this is,

$$\frac{d\Phi(E)}{dE} = \Phi_{\text{th}} \frac{E}{(kT)^2} e^{-\frac{E}{kT}}, \quad (5.2)$$

being Φ_{th} the total thermal neutron fluence, k the Boltzmann constant, and T the temperature of the medium where the neutrons have been thermalized. In pressurized water reactors (PWR), for instance, the water moderator is typically at a temperature around 600 K. However, these neutrons are easily thermalized again to room temperature (~ 300 K) when they reach the concrete shield, mainly because of the hydrogen content on it¹. Therefore, in this area it can be considered that $kT = 0.0253$ eV.

At thermal energies, neutron absorption cross sections are inversely proportional to the velocity of the neutrons. Typically, the cross section for neutrons with an energy $E_0 = 0.0253$ eV is reported in the bibliography, which is called "thermal neutron capture cross section"; for instance, [Cranston and White \[1971\]](#) report a thermal neutron capture cross section of 400 ± 40 mb for ^{40}Ca . Consequently, the neutron capture cross section for other energy in the thermal range is

$$\sigma(E) = \sigma(E_0) \sqrt{\frac{E_0}{E}}. \quad (5.3)$$

Therefore, the $^{41}\text{Ca}/^{40}\text{Ca}$ ratio produced by a thermal neutron fluence Φ_{th} would be

$$\begin{aligned} ^{41}\text{Ca}/^{40}\text{Ca} &= \Phi_{\text{th}} \cdot \sigma(E_0) \cdot \frac{1}{(kT)^2} \int_0^\infty \sqrt{\frac{E_0}{E}} E e^{-\frac{E}{kT}} dE = \\ &= \Phi_{\text{th}} \cdot \sigma(E_0) \cdot \sqrt{\frac{E_0}{kT}} \int_0^\infty \sqrt{t} e^{-t} dt = \frac{\sqrt{\pi}}{2} \sqrt{\frac{E_0}{kT}} \sigma(E_0) \Phi_{\text{th}}. \end{aligned} \quad (5.4)$$

Defining the thermal average cross section as

$$\bar{\sigma}(T) \equiv \frac{\sqrt{\pi}}{2} \sqrt{\frac{E_0}{kT}} \sigma(E_0), \quad (5.5)$$

¹Neutron energy loss is more important when the scattering process takes place with light nuclei.

the total thermal neutron fluence in a location is then directly related to the measured ⁴¹Ca/⁴⁰Ca there, being

$$\Phi_{\text{th}} = \frac{{}^{41}\text{Ca}/{}^{40}\text{Ca}}{\bar{\sigma}(T)}. \quad (5.6)$$

In concrete, where neutrons are thermalized to room temperature $kT = E_0$, the thermal average cross section would be $\bar{\sigma} = \frac{\sqrt{\pi}}{2}\sigma(E_0)$. For the ⁴⁰Ca(n,γ) reaction, this cross section would be, therefore, $354 \pm 35 \text{ mb} = (3.54 \pm 0.35) \times 10^{-25} \text{ cm}^2$.

Note that, since production of ⁴¹Ca is directly proportional to ⁴⁰Ca content, the ⁴¹Ca/⁴⁰Ca ratio is independent on the calcium concentration in the material. The only other important factor related to this ratio, besides the thermal neutron fluence, is the temperature to which these neutrons are thermalized.

The regions of maximum neutron flux in bioshields from commercial nuclear reactors can suffer thermal neutron fluences close to 10^{19} cm^{-2} . This would produce ⁴¹Ca/⁴⁰Ca ratios higher than 3.5×10^{-6} .

In order to calculate the ⁴¹Ca specific activity² from ⁴¹Ca/⁴⁰Ca measurements, it is necessary to know the calcium concentration in the concrete, which can strongly vary from one type of concrete to another.

The ⁴¹Ca/⁴⁰Ca ratio can be used, also, to calculate atom ratios from other radionuclides produced by neutron capture. For instance, the ³⁶Cl/³⁵Cl ratio in the same location would be

$${}^{36}\text{Cl}/{}^{35}\text{Cl} = \frac{\sigma[E_0, {}^{35}\text{Cl}(n, \gamma)]} {\sigma[E_0, {}^{40}\text{Ca}(n, \gamma)]} {}^{41}\text{Ca}/{}^{40}\text{Ca}, \quad (5.7)$$

independently of the temperature, in this case, since the same factor would correct both the thermal neutron capture cross sections of ³⁵Cl and ⁴⁰Ca.

5.2 Radiochemical treatment of concrete samples for ⁴¹Ca AMS measurements

Our chemical method to treat the concrete is, in some aspects, based on those methods used for ⁴¹Ca LSC or intercomparisons between this technique and AMS [Hampe et al., 2013; Hou, 2005; Warwick et al., 2009]. Nevertheless, many steps which are not necessary for ⁴¹Ca AMS

²The ⁴¹Ca specific activity in any material is defined as the ⁴¹Ca activity per material mass unit.

5.2. RADIOCHEMICAL TREATMENT OF CONCRETE SAMPLES FOR ^{41}Ca AMS MEASUREMENTS

have been eliminated, and some steps which improve the potassium suppression have been added. The method, as the one described for urine samples in [chapter 4](#), is divided in two parts: the calcium isolation as calcium carbonate, and the calcium fluoride precipitation. A simple scheme of the calcium isolation process is presented in [Figure 5.2](#).

Each sample is first digested in 20 ml of aqua regia during 2 hours. Typically, between 100 and 500 mg of each sample is used. The amount depends on the aspect of the sample:

- When most of it has a pale color and is easily ground, most of the sample comes from the binder, which is strongly dissolved by acid digestion, so less amount of concrete sample is needed.
- When the sample includes hard and dark aggregates, which are typically silicates which are not dissolved by aqua regia, a relatively large amount of sample, between 300 and 500 mg, is treated.

The $^{41}\text{Ca}/^{40}\text{Ca}$ ratio does not depend on the chemical form in which the calcium is found. Consequently, the fact that the acid digestion does not dissolve part of the calcium on the sample, like that calcium present in silicates, has no huge relevance. In [Figure 5.3](#) the difference between how the acid digestion attacks the sample depending on the aggregate/binder relationship can be observed. In one of the 2 samples, it can be observed how an aggregate is not affected by the acid digestion. This step eliminates most of the Si present in the sample.

The acid solution is centrifuged, discarding the precipitate. 20 ml of concentrated NH_3 is added to the supernatant in order to precipitate hydroxides from other elements present in concrete, like iron or magnesium. If necessary, more concentrated NH_3 is added until pH is between 9 and 11. The solution is centrifuged again, discarding the precipitate.

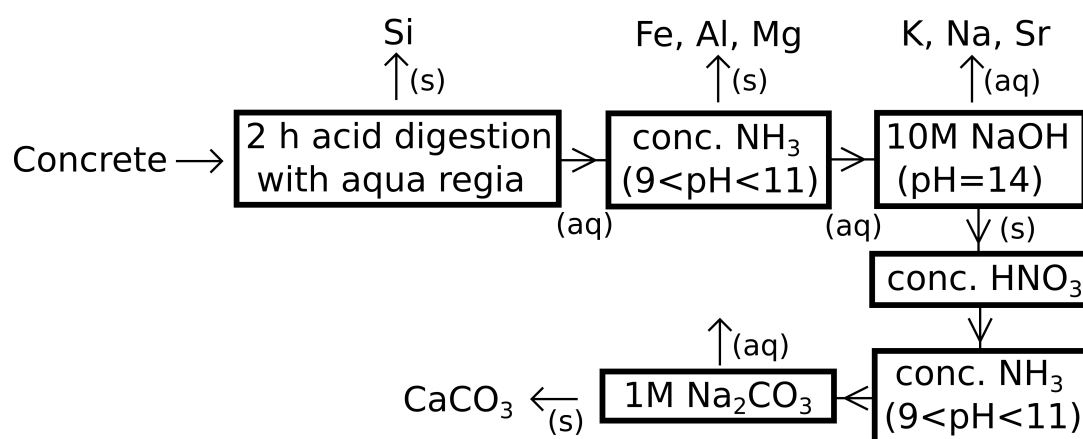


Figure 5.2: Scheme of the calcium isolation process for concrete samples.

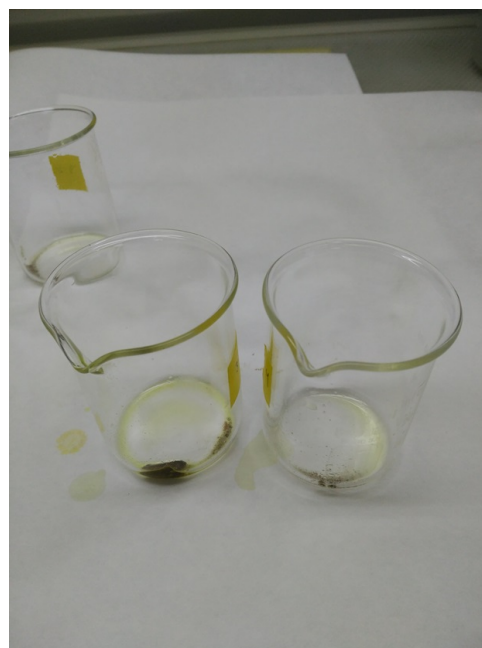
The addition of 10 M NaOH until pH=14 causes the precipitation of Ca(OH)₂ while hydroxides from strontium and alkali elements, like potassium, stay in the solution. This precipitation, therefore, adds another potassium reduction to those caused by the calcium carbonate and calcium fluoride precipitations that take place later. After centrifugation and discarding of the supernatant, the Ca(OH)₂ precipitate is dissolved with a few drops of concentrated HNO₃.

In order to precipitate the calcium carbonate, the pH is raised to 9-11 with concentrated NH₃, and a few drops of 1 M Na₂CO₃ are added. After centrifugation and discarding of the supernatant, the precipitate is washed with 10 ml of MilliQ water, and centrifuged, again, discarding the supernatant. This step is repeated again using acetone, instead of water. The final CaCO₃ precipitate is dried at 70 °C in order to get rid of the remaining acetone, and then, stored.

The calcium fluoride precipitation process depend on the expected ⁴¹Ca/⁴⁰Ca ratio. For many of the samples from NPP bioshields, ⁴¹Ca/⁴⁰Ca ratios are expected to be one or two orders of magnitude higher than 10⁻⁸. For these ratios, AMS measurements become problematic because of both: the cross talk in the ion source between these samples and those with lower ⁴¹Ca/⁴⁰Ca ratios, and the high ⁴¹Ca rates expected on the detector. Because of this, a dilution of that ratio with ⁴¹Ca-free calcium carrier is required.



(a) Before digestion



(b) After digestion

Figure 5.3: Effect of the acid digestion of concrete sample depending on the presence of aggregates.

In these cases, an aliquot of 10 mg from the carbonate precipitate is dissolved in 10 ml concentrated HNO₃, and 1 ml of the solution is taken to be measured by ICP-MS³. Commercial calcium carbonate is added to the rest of the solution until the expected ⁴¹Ca/⁴⁰Ca ratio is within the 10⁻¹⁰-10⁻⁸ range. For instance, if the expected ⁴¹Ca/⁴⁰Ca ratio is 10⁻⁷, around 1000 mg of ⁴¹Ca-free carbonate is added.

In the rest of the cases, an aliquot of 50 mg from the carbonate precipitate is dissolved with 5 ml HNO₃ diluted to 5%.

The storage of the calcium carbonate allows the change in ⁴¹Ca/⁴⁰Ca dilution factor in the event of measure very high or very low ⁴¹Ca/⁴⁰Ca ratios in the first measurement attempt.

In both cases, adding a few drops of concentrated HF initiates the precipitation of CaF₂. The sample is set overnight, and then centrifuged, discarding the supernatant. The precipitate is washed with MilliQ water, centrifugated discarding the supernatant, and dried at 105 °C during 24 h.

All the measurements shown in [section 5.3](#) have been performed with samples treated with this method. In all these measurements, ⁴⁰Ca currents and ³⁹K/⁴⁰Ca ratios from the samples were totally equivalent to those from standards and blanks, even when ICP-MS measurements from the carbonates show that the purity from these is typically in the 50-75% range.

5.3 Measurements of ⁴¹Ca in the bioshield of the José Cabrera Nuclear Power Plant

5.3.1 The José Cabrera Power Plant: description of the samples

José Cabrera Power Plant, located in Almonacid de Zorita, was the first [NPP](#) in Spain. It started its operation in 1969, and operated with a 150 MW [PWR](#), designed by Westinghouse®, until 2006 [[CSN, n.d.](#)]. According to the operating company, the maximum thermal neutron fluence on the bioshield is $7.4 \times 10^{18} \text{ cm}^{-2}$, which means a maximum ⁴¹Ca/⁴⁰Ca ratio of 2.6×10^{-6} .

The calcium content of some samples from the outer parts of the bioshield, together with the content of other elements, was measured by PIXE⁴. The results prove the high heterogeneity of the concrete material, since Ca concentrations reach levels from 20% to 40%. Nevertheless, most of the samples showed Ca concentrations between 25% and 35%. For the

³This measurements are performed by the radioisotope service at CITIUS.

⁴This measurements were performed by the Ion Beam Analysis and Modification of Materials Research Unit at [CNA](#).

calculations of the ⁴¹Ca specific activity, therefore, a Ca concentration of (30 ± 5)% is used. According to this, a sample with a ⁴¹Ca/⁴⁰Ca ratio is 10⁻⁹ would have a ⁴¹Ca specific activity of 1 Bq/g, and maximum ⁴¹Ca specific activities of 2500 Bq/g are expected.

The exemption limit established by the IAEA is 10⁵ Bq/g [IAEA, 2012], which is well above these maximum expected ⁴¹Ca specific activities. However, in some countries, other more restrictive limits are established, for instance, for the free release of residues from NPPs. Taking Germany as an example, this limit for ⁴¹Ca in solid or liquid waste is 20 Bq/g [BMJV, n.d.], which is below the maximum expected ⁴¹Ca specific activities. On the other hand, in Spain, these further limitations do not exist, and the same exemption limits established by the IAEA are used [CSN, 2003]. Nevertheless, ⁴¹Ca/⁴⁰Ca results, as direct measurements of the thermal neutron fluence, are extremely useful to the estimation of the inventories of other radionuclides. Furthermore, together with the test of the mechanical properties of the concrete blocks, these measurements contribute to the study of the relationship between the neutron fluence suffered by concrete and the deterioration of these mechanical properties.

The samples were extracted and sent to the CNA by ENRESA. The reactor vessel from José Cabrera was segmented and removed between 2014 and 2015 [ENRESA, n.d.]. Afterward, in 2016, the area of the bioshield closer to the vessel was segmented in 8 different blocks (see Figure 5.4) and removed.

4 drill cores were extracted from each of the blocks 1-6 (see Figure 5.5): one in the maximum

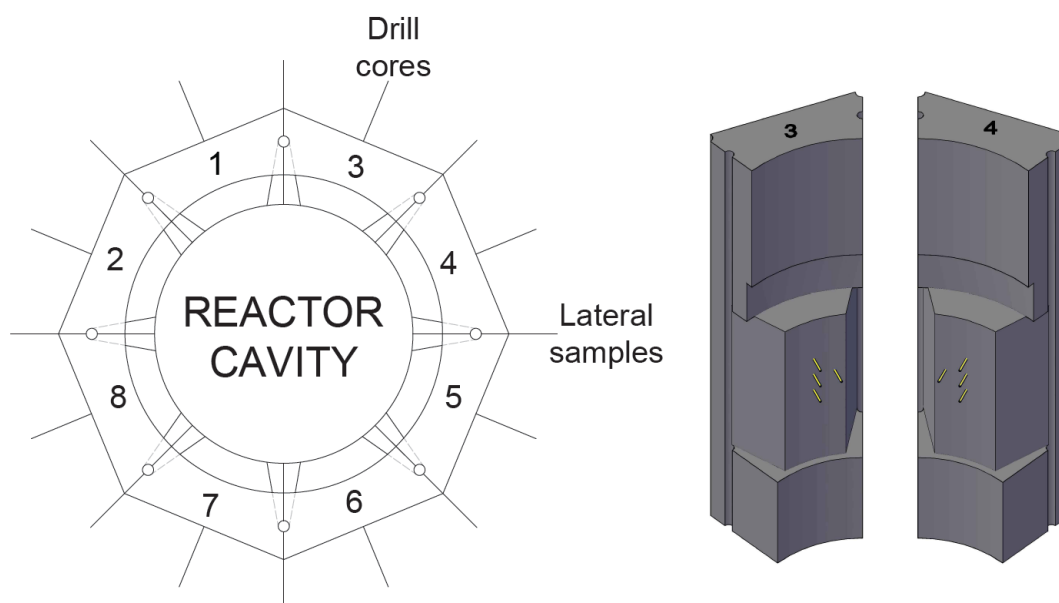


Figure 5.4: Scheme of the segmentation of the bioshield of José Cabrera and 3D picture of the shape from each block.

neutron fluence point (CDC), two at both sides at 30 cm in the vertical plane (C1 and D1), and one at 30 cm in the horizontal plane (CDL). 5 samples were taken from each of these 108 cm long drill cores, with a separation of 27 cm between each sample and the next.

After the drill core extraction, each block was segmented in 5 different sub-blocks. Different samples from the sides of the sub-blocks from regions of lower neutron fluence were obtained by scrapping the lateral surface (see Figure 5.6). Since this surface may have suffered cross contamination during the segmentation process, the first scrapping from each point was discarded.

The samples from the drill cores from blocks 3 and 4, and those from both sides of block 3 and the right side⁵ of block 4 were sent to CNA, where we performed the chemical treatment and the ^{41}Ca AMS measurements. The segmentation caused a ^{137}Cs contamination, so less than 1 g of each of the lateral samples were sent to the CNA in order to keep the whole package on exemption levels. Consequently, for most of the lateral samples the whole sample was used. Several grams of the samples from the drill cores were sent, so most of this material was sent back to José Cabrera.

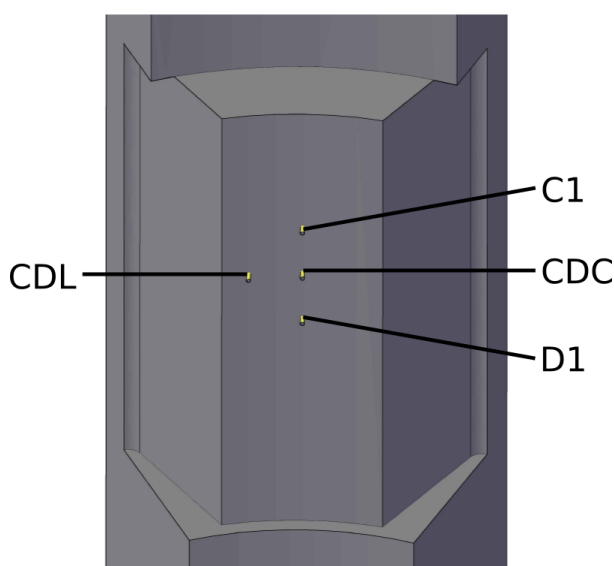


Figure 5.5: Schematic view of the position of the drill cores. The core CDC is at the same height at which the center of the reactor core was; the other cores are at a distance of 30 cm from this one.

⁵The relative location is chosen as seen from the reactor cavity.

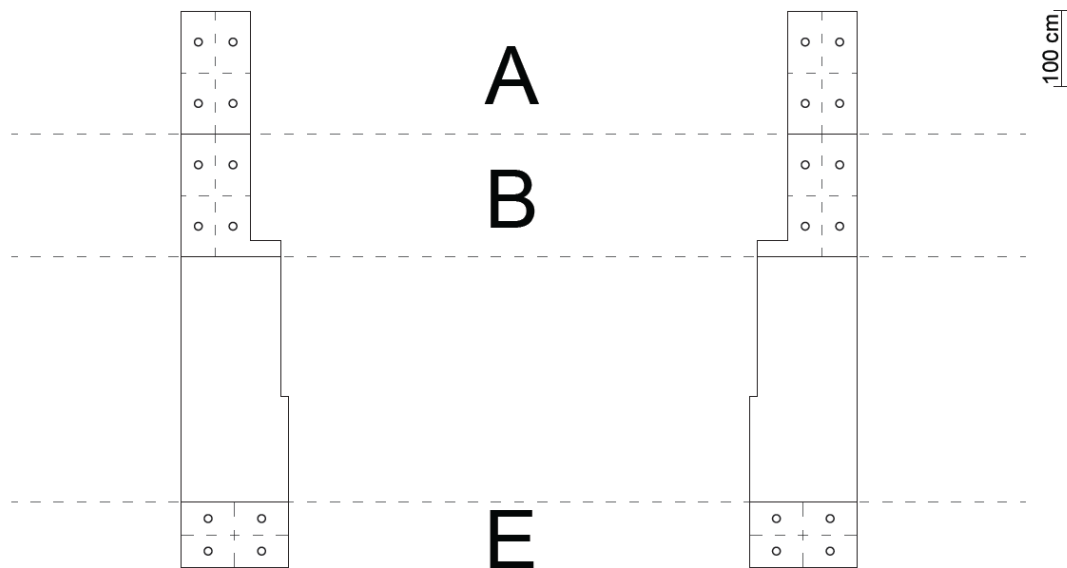


Figure 5.6: Position of the samples taken by scraping the lateral surface of the sub-blocks. The letter codes from the different sub-blocks are also shown.

5.3.2 Depth profiles

In the bibliography, ^{41}Ca measurements with LSC and AMS in drill cores from experimental reactors can be found [Hou, 2005; Warwick et al., 2009]. As expected, these studies, on the location of maximum neutron fluence, present similar $^{41}\text{Ca}/^{40}\text{Ca}$ attenuation profiles as the thermal neutron flux [Megahid et al., 1981]. Our measurements are the first measurement of this kind in a commercial NPP. Furthermore, not only radial cores at the height of maximum fluence have been measured.

Figure 5.7 shows the $^{41}\text{Ca}/^{40}\text{Ca}$ depth profiles from all these drill cores, extracted from blocks 3 and 4. Some results from the block 4 are estimations, since we have not received the results of the ICP-MS measurements necessary to know the $^{41}\text{Ca}/^{40}\text{Ca}$ dilution factor yet. An almost exponential attenuation can be observed in the profiles from the central drill cores (CDC) and those 30 cm above (C1). The attenuation coefficients from the exponential fits of these depth profiles are in the $0.06\text{-}0.08\text{ cm}^{-1}$ range. This agrees with the attenuation profile for thermal neutrons found by Megahid et al. [1981] and the $^{41}\text{Ca}/^{40}\text{Ca}$ profile found in research reactors by Hou [2005] and Warwick et al. [2009]. The depth profiles from the drill cores 30 cm under the central ones (D1) also exhibit, with the exemption of some points, this exponential behavior. Nevertheless, at some points, the thermal neutron fluence increase, instead of decrease. The reason could be the huge chemical heterogeneity from the concrete, specially in the water content, which may lead to a change in the diffusion of the neutrons through the

5.3. MEASUREMENTS OF ^{41}Ca IN THE BIOSHIELD OF THE JOSÉ CABRERA NUCLEAR POWER PLANT

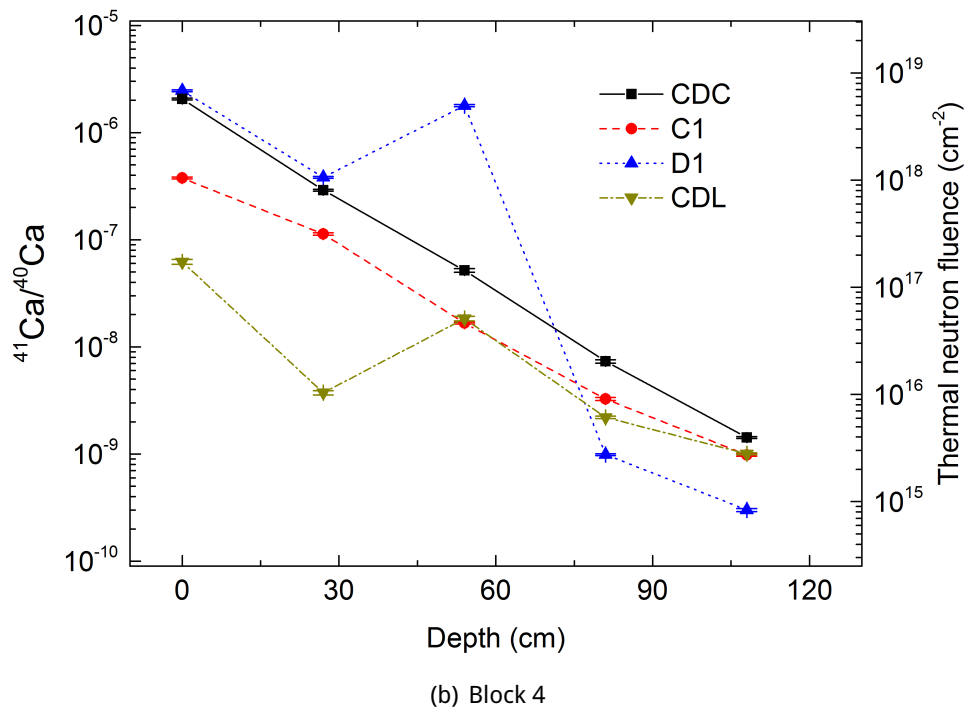
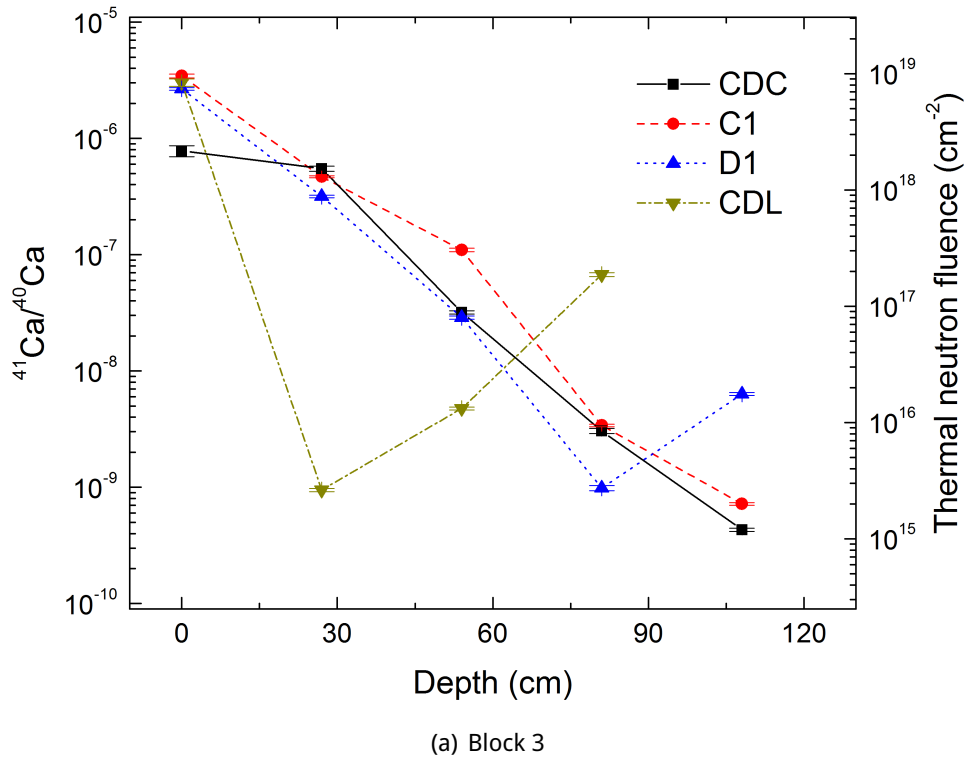


Figure 5.7: $^{41}\text{Ca}/^{40}\text{Ca}$ results from the drill core samples and correspondence with thermal neutron fluence.

concrete structure or even a higher moderation of the fast neutrons at some points.

The case of those drill cores at 30 cm from the central ones in the horizontal direction (CDL) is special, since they are extremely close to the apertures toward the instrumentation wells (see [Figure 5.8](#)). This apertures were filled with air, so they could be considered "transparent" to the neutrons, which reached the side walls of these aperture. The diffusion of the neutrons in the concrete would cause another "neutron front", perpendicular to this wall. For deeper locations of the CDL drill cores, the neutron fluence added by this front, relative to the one coming from the cavity surface, would be more important than for those locations closer to the reactor vessel. In any case, this apertures add complexity to the behavior of the neutrons fluence in these locations, so the non ideal behavior of the $^{41}\text{Ca}/^{40}\text{Ca}$ depth profiles in these drill cores is not unexpected.

The lack of symmetry between the results of both blocks, on the other hand, is quite unexpected, but could be also a consequence of the huge heterogeneity of the material.

Due to the 30% Ca content of the concrete, the samples closest to the vessel, with $^{41}\text{Ca}/^{40}\text{Ca}$ ratios around 3×10^{-6} , would present ^{41}Ca specific activities of 3000 Bq/g. On the other hand, the sample with the minimum $^{41}\text{Ca}/^{40}\text{Ca}$ ratio, 3×10^{-10} , would present ^{41}Ca specific activities of 0.3 Bq/g.

According to the results, maximum thermal neutron fluences on the bioshield surface are very close to 10^{19} cm^{-2} . This result has a great relevance, since it is known that concrete

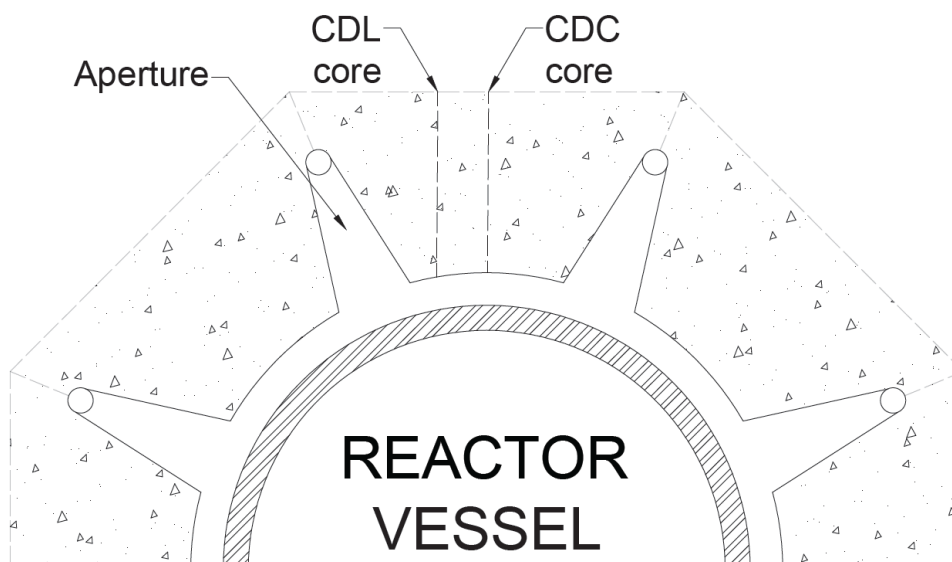


Figure 5.8: Cross section of the José Cabrera reactor vessel and bioshield when the plant was operative at the height of maximum neutron fluence. The positions where drill cores CDC and CDL were taken, for blocks 1, 4 and 6. For the rest of the blocks, CDL core was taken from the opposite side.

materials start losing some of the mechanical properties when they undergo total neutron fluences above 10^{19} cm^{-2} [Field et al., 2015]. Taking into account that our results only assess the thermal neutron fluence, it is almost sure that the total neutron fluence reached levels much higher than 10^{19} cm^{-2} at these points. These effects on the mechanical properties, nevertheless, may strongly depend on the type of concrete. Consequently, the study of the mechanical properties of this concrete, which ENRESA will perform, together with our results of the thermal neutron fluences and additional studies of the fast neutron fluence, could help to a better assessment of the effects of neutron radiation in these properties.

Another capability of these results is the estimation of the specific activities from other radionuclides which are produced in concrete mainly by thermal neutron activation. This is the case, for instance, of ^{36}Cl . Chlorine is only found in trace amounts in concrete, mainly caused by the Cl^- presence in water. Typical chloride concentrations in concrete are in the range of 100 ppm. The much lower presence of chlorine in concrete, nevertheless, is compensated by the relatively high thermal neutron capture cross section, of $41.8 \pm 1.2 \text{ b}$ [Sims and Juhnke, 1969], this is, 2 orders of magnitude higher than the one for ^{40}Ca . In any case, even assuming chloride concentrations near limits, ^{36}Cl specific activities would not exceed 35 Bq/g, which is well below the limit for exempt material, 10^4 Bq/g [CSN, 2003; IAEA, 2012].

5.3.3 Results from the lateral samples

Samples from the left side of the block 4 were not sent to be measured by AMS at CNA since these would be equivalent to those from the right side of the block 3. A scheme of the location of these samples was presented in Figure 5.6. The heights of these locations, relative to the center of the reactor core, were +360 cm, +280 cm, +200 cm, +120 cm, -260 cm and -300 cm. The depths were 22.5 cm and 67.5 cm for sub-blocks A and B, and 35 cm and 105 cm for sub-block E.

The $^{41}\text{Ca}/^{40}\text{Ca}$ results in these locations is presented in Figure 5.9. The main uncertainty for the interpretation of these results is the possibility of cross-contamination during the bioshield segmentation process. Nevertheless, in most of the cases, an expected indirect relationship between the vertical distance to the core and the $^{41}\text{Ca}/^{40}\text{Ca}$ ratio is found; so is between depth and $^{41}\text{Ca}/^{40}\text{Ca}$. Taking into account that these samples are relatively far from the areas of maximum neutron fluence, the exemptions to these indirect relationships are not unexpected. These exemptions may be caused by the thermal neutron diffusion processes or the presence of higher fast neutron fluences near these areas which are moderated by the concrete, as it happened in the case of the drill cores. It is, nevertheless, quite unexpected that the results from the 3 sides are not equivalent since, because of the geometry

of the reactor core, the neutron spatial distribution should have a 45° rotational symmetry. On the other hand, this rotational symmetry should only be expected on the neutron fluence for an homogeneous material. As it was previously stated, this is not the case of concrete walls. One of the elements where this heterogeneity is expected to be high is hydrogen, since additional water is typically incorporated during the hardening process, and in the different fuel changes during the operation of the NPP. Hydrogen presence is key for thermal neutron diffusion and fast neutron moderation.

The minimum ⁴¹Ca specific activity in this samples is found to be close to 0.15 Bq/g. For most of these lateral samples the maximum mass available was of several hundred of milligrams in order to keep the sample package below ¹³⁷Cs exemption limits. On the other hand, the most sensitive studies of ⁴¹Ca measurements by LSC report detection limits of 0.1 Bq. According to this, ⁴¹Ca characterization by LSC would have not been possible, and AMS becomes necessary. Besides, even in the case where samples could have been measured by LSC, as those from the drill cores, the sample mass which should be destroyed and statistical uncertainties would have been much higher.

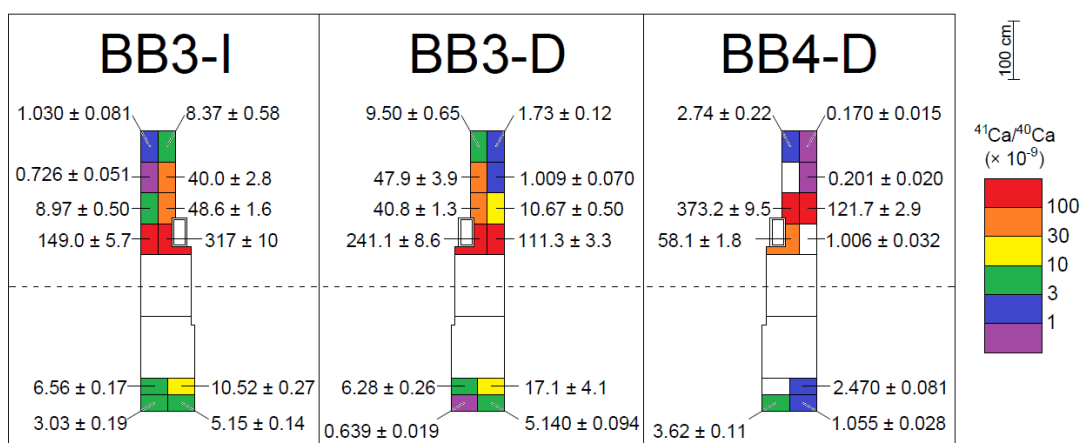


Figure 5.9: ⁴¹Ca/⁴⁰Ca results, in × 10⁻⁹ units, from the lateral samples. The -I and -D makes reference to which of both sides of the block the samples come from, as seen from the reactor cavity: I, for left side; D, for right side. The dashed line represents the height where the center of the reactor core was.

Chapter 6

Summary and conclusions

This thesis has fulfilled its main goal: the setting-up of the ^{41}Ca measurements with the 1 MV AMS system at CNA, SARA. Most of the results obtained with this system can also be applied to other 1 MV AMS systems from HVE. Besides, the data collected from the different measurements performed during this thesis on this system and the 600 kV AMS system at ETH Zurich, TANDY, have provided information useful to any ^{41}Ca AMS measurement, specially at low energy systems. Routine AMS measurements of ^{41}Ca with SARA have been implemented at CNA, applied to the characterization of low level nuclear residues.

In chapter 1, an initial idea about the different applications of ^{41}Ca measurements was presented, together with the basic ideas related to the AMS technique. The presentation of the SARA and TANDY systems in chapter 2 served also to describe the physical processes involved in the different elements of AMS systems. These descriptions focus on the recent changes on both systems and in those differences which are important to the ^{41}Ca AMS performance. Different studies related to the ^{41}K interference, which is the main challenge in ^{41}Ca AMS at low energies, are presented in chapter 3. The experiments in order to setting-up and optimize the performance of ^{41}Ca measurements at SARA are detailed in chapter 4. The first application of ^{41}Ca AMS at CNA, the study of the ^{41}Ca spatial distribution in the bioshield of a NPP, can be found in chapter 5.

^{41}Ca AMS at low energies

Even when the ^{41}K interference can be estimated by sequentially measuring the other stable isotope of potassium, ^{39}K (K-correction), it is important to assess the possible ways by which this interference can vary.

The existence of the $(^{41}\text{K}^{57}\text{Fe})^-$ ion and its relationship with the ^{41}K interference has been proven thanks to several experiments performed at TANDY during the stay at [ETH LIP](#). This is the cause of the relatively high ^{41}K ion rates when metallic elements are sputtered. The main consequences, which have been observed in both systems, SARA and TANDY, are:

- The dependence of the ^{41}K interference on the materials used in the cathode, like the target holder or the binder. For instance, higher $^{41}\text{K}/^{40}\text{Ca}$ has been observed when Al target holders are used, instead of Ti or Cu. Al materials typically present higher Fe trace content.
- The $^{41}\text{K}/^{40}\text{Ca}$ is not constant in time. Because of this, the K-correction must be applied sequentially during the data analysis. A detailed study of this evolution at SARA is presented, showing how the ^{41}K interference behavior differs even for different targets from the same sample.

Applying this K-correction manually can be time consuming. Therefore, two programs have been written in FORTRAN code for the ^{41}Ca measurements at SARA and TANDY. The use of these programs means a huge reduction of the time dedicated to this analysis, from around one hour to several minutes.

^{41}Ca measurements at SARA

A detailed study of the performance parameters of ^{41}Ca measurements at SARA has been performed throughout this thesis. The main parameters studied have been:

- **Ionization efficiency:** mixing the calcium fluoride samples with silver in a $\text{CaF}_2:\text{Ag}$ weight ratio of 1:4, the $(^{40}\text{CaF}_3)^-$ output current of the [HVE SO-110B](#) ion source is stable and between 50 and 150 nA. The ionization efficiency in this case is around 0.1%.
- **Stripper transmission:** the charge state with the highest transmission in the He stripper is the 2+ state. Using a He gas pressure of 0.03 mbar, this is, a He mass thickness of $\sim 0.075 \mu\text{g}\cdot\text{cm}^{-2}$, transmission for this charge state is 40%, and a full suppression of the molecular background is achieved. The possibilities of the charge state 3+, with a lower transmission of 20%, are being studied because of the possibility of reducing the final background.
- **GIC detection efficiency:** the compact [GIC](#) presents detection efficiencies higher than 90% for ^{41}Ca rates lower than 1000 s^{-1} . For higher rates, the efficiency decreases linearly.

-
- **$^{41}\text{Ca}/^{40}\text{Ca}$ background:** while the typical $^{41}\text{K}/^{40}\text{Ca}$ ratios are in the 10^{-11} range, the $^{41}\text{Ca}/^{40}\text{Ca}$ in blank samples, after applying the K-correction, is one order of magnitude lower.
 - **HE side optical transmission:** thanks to the independence of the object of the [HEM](#) on the charge state, due to the quadrupole triplet at the exit of the accelerator, the ^{41}Ca beam is optimally transported through the [HE](#) spectrometer. The measurements of ^{41}Ca standards show that the optical transmission in this sector is in the 90-100% range.

The comparison of the performance parameters at SARA with those at TANDY show that the capabilities of both systems for ^{41}Ca [AMS](#) are equivalent. SARA is perfectly fit to perform, for instance, ^{41}Ca measurements for biomedical applications and for characterization of low level nuclear residues.

^{41}Ca in the bioshield from a nuclear power plant

The first application of the ^{41}Ca measurements at SARA has been the study of the ^{41}Ca spatial distribution in the bioshield of the José Cabrera [NPP](#). The $^{41}\text{Ca}/^{40}\text{Ca}$ ratio in this structure is directly related to the thermal neutron fluence suffered by it. A radiochemical method to treat large number of concrete samples has been developed and applied to samples from a huge variety of depths and heights of José Cabrera's bioshield. Only 100-500 mg per sample are needed to be destroyed in this treatment, one order of magnitude lower than the sample mass needed for [LSC](#) measurements. Besides, [AMS](#) not only improves the limit of detection, but also improves the precision of this measurements.

The results from the ^{41}Ca measurements at SARA show that, because of the complexity of the geometry and the heterogeneity of the material, the behavior of the thermal neutron fluence becomes less ideal the farther the samples are from the position of maximum neutron fluence. Consequently, neutron transport simulations may be not enough to estimate the inventories of the radionuclides produced by the neutron radiation.

Relevant publications within this PhD thesis

Two articles have been published related to this thesis:

The studies of the relationship with the ^{41}K interference of the iron presence and the time evolution, and the specific features of the measurement analysis relates to the K-correction, detailed in [chapter 3](#), are presented in

C. VIVO-VILCHES, J.M. LÓPEZ-GUTIÉRREZ, M. GARCÍA-LEÓN, C. VOCKENHUBER

Factors related to ^{41}K interference on ^{41}Ca AMS measurements

Nuclear Instruments and Methods in Physics Research Section B: Beam Interactions with Materials and Atoms, in press

doi: [10.1016/j.nimb.2018.04.031](https://doi.org/10.1016/j.nimb.2018.04.031)

The main results and experiments presented on [chapter 4](#) about the optimization of the performance parameters of the ^{41}Ca measurements with SARA can be found in

C. VIVO-VILCHES, J.M. LÓPEZ-GUTIÉRREZ, M. GARCÍA-LEÓN, C. VOCKENHUBER, T. WALZCYK

^{41}Ca measurements on the 1 MV AMS facility at the Centro Nacional de Aceleradores (CNA, Spain)

Nuclear Instruments and Methods in Physics Research Section B: Beam Interactions with Materials and Atoms 413 (2017) 13-18

doi: [10.1016/j.nimb.2017.10.003](https://doi.org/10.1016/j.nimb.2017.10.003)

Appendix A

GICOSY files

Figures 2.18 and 2.20 show simulations of the ion optics in the HE spectrometers of SARA and TANDY, performed with GICOSY [Weick, n.d.]. The geometry data from both systems were obtained from Jacob [2001] and Chamizo [2009]. The meaning of the different codes can be found in the manual, which is in Dr. Helmut Weick's webpage. Simulation from Figure 2.15 has also been performed with GICOSY.

Below, the files written for the HE spectrometers of SARA and TANDY are presented.

A.1 SARA HE spectrometer

```
S N SARA-HEsector ;
R P 0.395 41 2 ;
P X 0.00 0.014 ;
P Y 0.00 0.014 ;
D P 0.005 0.0025 ;
;
VQ2=7.8;
VQ1=-VQ2;
;
S S ;
;
D L 0.24 ;
;
F F 0 ;
```

APPENDIX A. GICOSY FILES

A C 0.8 1.1375 0.0475;
F F 0 ;
;
D L 0.095 ;
;
F F 1;
;
E Q 0.059 VQ1 0.025;
;
F F 1;
;
D L 0.0405 ;
;
F F 1;
;
E Q 0.132 VQ2 0.025;
;
F F 1;
;
D L 0.0405 ;
;
F F 1;
;
E Q 0.059 VQ1 0.025;
;
F F 1;
;
D L 0.52 ;
;
F F 3 25.6 0.0 ;
;
M S 0.85 90 0.0215 0 0 0 0 0;
;
F F 3 31 0.0 ;
;
D L 1.094 ;
;

```
D H E (X,Y) 100000 0.003 0.003 1 10 ;
;
D L 0.375 ;
;
F F 1 0 0;
;
E S 0.65 120 0.0125 1 -1 1;
;
F F 1 0 0;
;
D L 0.375 ;
;
D H E (X,Y) 100000 0.003 0.003 1 10 ;
;
D L 0.375 ;
;
D S 0.025 10 100 1 3 1 3;;
D B 0.035 0.035 1 1 3 1 3 1 3 1;
END ;
;
```

A.2 TANDY HE spectrometer

```
S N TANDY-HEsector ;
R P 0.23 41 2 ;
P X 0.00 0.014 ;
P Y 0.00 0.014 ;
D P 0.025 0.0025 ;
;
S S ;
;
D L 0.38 ;
;
F F 0 ;
A C 0.24 2.083 0.0475;
F F 0 ;
```

APPENDIX A. GICOSY FILES

```
D L 1.391 ;
;
F F 3 27.5 0.0 ;
;
M S 0.75 90 0.0215 0 0 0 0 0;
;
F F 3 27.5 0.0 ;
;
D L 1.0 ;
;
D H E (X,Y) 100000 0.005 0.005 1 10 ;
;
D L 0.743 ;
;
F F 1 0 0;
;
E S 0.75 90 0.02 1 -1 1;
;
F F 1 0 0;
;
D L 0.77 ;
;
D H E (X,Y) 100000 0.005 0.005 1 10 ;
;
D L 0.6 ;
;
D S 0.025 10 100 1 3 1 3;
D B 0.035 0.035 1 1 3 1 3 1 3 1;
;
END ;
;
```

Appendix B

Unfeasibility of matrices different from CaH_2 for the production of $(\text{CaH}_3)^-$ ions

B.1 Alternatives to calcium hydride in the bibliography

It is widely proven that the extraction of the $(\text{CaH}_3)^-$ ion instead of the $(\text{CaF}_3)^-$ significantly reduces the ^{41}K interference. This, therefore, could be an indication of a theoretical advantage of using the calcium hydride (CaH_2) in ^{41}Ca AMS at low energies, since ^{41}K interference cannot be discriminated in the detector. Nevertheless, dealing with calcium hydride is problematic because it is a highly hygroscopic compound, so this chemical compound is not suitable for applications where a large number of samples is involved.

The use of more chemically stable matrices to produce the $(\text{CaH}_3)^-$ ions would solve this problem. The idea of producing these ions from different mixes of calcium compounds with titanium hydride (TiH_2), which is much more stable than other hydrides, had been studied during the 90's [Fink et al., 1990; Baba et al., 1997]. In fact, TiH_2 is the compound commonly used to produce H^- ions by Cs sputtering [Middleton, 1990].

Fink et al. [1990], which reported $(^{40}\text{CaF}_3)^-$ currents one order of magnitude higher than those at SARA, found $(^{40}\text{CaH}_3)^-$ current outputs from a $\text{CaO}+\text{TiH}_2$ mix in a weight ratio of 1:10 of 20-30 nA, so only currents of several nA would be expected in our system. Besides, the use of calcium oxide did not seem a great improvement on sample handling, since this compound reacts violently with water.

Baba et al. [1997] reported $(^{40}\text{CaH}_3)^-$ currents lower than 1 nA from a $\text{CaF}_2+\text{TiH}_2+\text{LiCl}$ mix in a weight ratio of 1:2:1. In this case, the low current could have been caused because of the presence of other compound, the LiCl, which was added to use the $(^7\text{Li}^{37}\text{Cl})^-$ beam as a *pilot* beam in order to tune the $(^{41}\text{CaH}_3)^-$ ions, with the same mass (44 u).

On the other hand, in a more recent study of the possibility of performing ^{14}C AMS using calcium carbonate (CaCO_3) instead of graphite, Longworth et al. [2013] showed a spectrum where there is an important peak of negative ions with mass 43 u, identified in this publication as $(^{40}\text{CaH}_3)^-$ ions. This was found in targets where a mix of calcium carbonate and metallic Ti was pressed in aluminum holders. Consequently, we thought that the idea of producing $(\text{CaH}_3)^-$ ions from mixes of calcium salts with TiH_2 should not be discarded. Nevertheless, there existed the possibility of a wrong interpretation of this peak observed by Longworth et al. [2013]: since their samples were pressed in aluminum holders, and oxygen is present in the calcium carbonate, these ions with a mass of 43 u could have been $(^{27}\text{Al}^{16}\text{O})^-$.

B.2 The experiment at SARA

Taking advantage of the equal mass of the $(^{27}\text{Al}^{16}\text{O})^-$ and the $(^{40}\text{CaH}_3)^-$ ions, we decided to use the aluminum oxide samples typically used for ^{26}Al AMS to tune this mass. Afterward, we tested different mixes of calcium salts with TiH_2 , with and without adding silver powder to those mixes.

Therefore, we prepared 5 types of targets, all of them pressed in copper holders:

- Aluminum oxide (Al_2O_3) mixed with copper in a $\text{Al}_2\text{O}_3:\text{Cu}$ weight ratio. This is the configuration which optimize the $^{27}\text{Al}^-$ current in the ion source at SARA and, so, the one used for ^{26}Al measurements at CNA [Padilla, 2015].
- Calcium carbonate mixed with titanium hydride in a $\text{CaCO}_3:\text{TiH}_2$ weight ratio of 1:2.
- The latter mixed with silver, in a $\text{CaCO}_3:\text{TiH}_2:\text{Ag}$ weight ratio of 1:2:8.
- Calcium fluoride mixed with titanium hydride in a $\text{CaF}_2:\text{TiH}_2$ weight ratio of 1:2.
- The latter mixed with silver, in a $\text{CaF}_2:\text{TiH}_2:\text{Ag}$ weight ratio of 1:2:8.

The weight ratio between calcium salt and titanium hydride was chosen so that the volumes of both compounds were similar. In the cases where silver was added, this was chosen so that the volume from the salt-hydride mix and that from the silver were also similar. 4 targets were pressed from each type.

The 43 u mass was soon successfully tuned with the aluminum oxide targets, which presented stable $(^{27}\text{Al}^{16}\text{O})^-$ current outputs of 500 nA. This is lower than the 1 μA output at the ETH Zurich 6 MV EN-TANDEM AMS system [Miltenberger et al., 2017]. Nevertheless, for the $^{27}\text{Al}^-$ ion, a lower current (~ 100 nA) is also observed at SARA, comparing with this system (~ 200 nA) [Christl et al., 2013; Chamizo et al., 2015c].

Afterward, all the targets pressed from the 4 different mixes were tested. For all of them, the maximum current from 43 u ions, this is, almost certainly $(^{40}\text{CaH}_3)^-$ ions, was 5 nA. More important was the instability of those currents in every target. Even increasing the Cs reservoir temperature, only unstable currents lower than 10 nA were observed. Besides, in most of the cases, the ion current decreased in few minutes to near 0 nA.

Due to the variety of mixes we tried, and since no stable $(^{40}\text{CaH}_3)^-$ ion current could be produced from any of them, the use of these matrices for the extraction of the $(\text{CaH}_3)^-$ ion does not seem feasible.

APPENDIX B. UNFEASIBILITY OF MATRICES DIFFERENT FROM CAH_2 FOR THE PRODUCTION OF $(CAH_3)^+$ IONS

Appendix C

FORTRAN programs for ^{41}Ca measurement analysis

In [chapter 3](#), it is stated that 2 programs had been written in order to perform the data analysis of ^{41}Ca measurements at SARA and TANDY. Since the differences between both are minimal, here only one example of the input file used by the program for measurements at SARA is presented. The information provided by the output files is also explained. The FORTRAN file is not shown in this thesis because of its length.

C.1 Input file

Below, an example of an input file of the program used for ^{41}Ca measurements at SARA is shown. The input file of the program for ^{41}Ca measurements at TANDY also asks information about the maximum transmission deviation from the average and which of the cathodes are not calcium fluoride samples (cathodes with only silver, for instance) to not taking those into account when calculating the average stripper transmission.

Number of samples

24

First run

49

Number of runs/sample:

7

Number of cycles (=seq)/run:

5

min. ⁴⁰Ca HE (nA):

20

max. ³⁹K/⁴⁰Ca in run:

1.25e-9

max rate (cts/s):

3000.0

Ignore first run? (yes/no=1/0)

0

Sample scatter (%):

1

Charge state:

2

Number of standards of interest:

3

Standard 1 nom. val, number of samples, positions:

1.0181e-8

2

3

15

Standard 2 nom. val, number of samples, positions:

1.0479e-9

2

4

16

Standard 3 nom. val, number of samples, positions:

1.0520e-10

2

5

17

Number of blanks:

4

Position:

2

7

14

19

Pulser (1/0=yes/no)

1

Pulser frequency (Hz)

100.131

C.2 Output files

C.2.1 out-K-correction

This file is written while performing the K-correction. The information provided is:

- $^{39}\text{K}/^{40}\text{Ca}$ and $^{41}\text{M}/^{40}\text{Ca}$ ratios from the different runs from all the blank samples, which are the (x,y) values for the linear regression.
- The K-correction factor α , this is, the slope from the linear regression.
- The relative uncertainty of α .
- The R^2 value of the linear regression.

C.2.2 out-runs

The file providing information about the different runs from all the samples is written between applying the K-correction and the other important corrections: blank and standard correction.

The information provided for each run is:

- The number of sequences which passed the discard criteria during that run.
- The total number of ^{41}M counts detected in that run.
- The average ^{40}Ca current.
- The average $^{39}\text{K}/^{40}\text{Ca}$ ratio.
- The K-corrected $^{41}\text{Ca}/^{40}\text{Ca}$ ratio.
- The relative uncertainty of this ratio.
- The relative standard deviation of this ratio.

In the case of measurements at TANDY, this file also provides information about the stripper transmission.

C.2.3 out-blank

This file is written while the background is being calculated. It just shows:

- The average $^{41}\text{Ca}/^{40}\text{Ca}$ from each blank sample after K-correction.
- The $^{41}\text{Ca}/^{40}\text{Ca}$ background, this is, the average from all the blank samples.
- The relative standard deviation from this background.

C.2.4 out-stds

This file is written while calculating the nominal/experimental factor from the standard samples. It shows, for each different standard material:

- The nominal $^{41}\text{Ca}/^{40}\text{Ca}$ ratio from that material.

- The average of the measured $^{41}\text{Ca}/^{40}\text{Ca}$ in all the cathodes from that material.
- The factor between this nominal and measured ratios.
- The relative standard deviation from this factor.

It also shows that average of the nominal/measured factor from different standard materials, and its final relative uncertainty.

C.2.5 out-final-ratios

In this file, the final results from each sample are presented.

The information provided for each sample is:

- The number of runs from that sample which passed the discard criteria.
- The average K-corrected $^{41}\text{Ca}/^{40}\text{Ca}$ ratio.
- The relative uncertainty from that ratio.
- The relative standard deviation from that ratio.
- The integral of the χ^2 distribution which is used to select the uncertainty of the blank-corrected ratio.
- The blank-corrected $^{41}\text{Ca}/^{40}\text{Ca}$ ratio.
- The relative uncertainty from that ratio.
- The final standard-corrected $^{41}\text{Ca}/^{40}\text{Ca}$ ratio.
- The relative uncertainty from that ratio.
- The total number of ^{41}M counts detected in all the runs from that sample.
- The average $^{39}\text{K}/^{40}\text{Ca}$ ratio.
- The average ^{40}Ca current.

In the case of measurements at TANDY, this file also provides information about the stripper transmission.

Bibliography

Akhmadaliev, S., Heller, R., Hanf, D., Rugel, G., Merchel, S., (2013). The new 6 MV AMS-facility DREAMS at Dresden. *Nuclear Instruments and Methods in Physics Research Section B: Beam Interactions with Materials and Atoms* 294, 5–10.

<http://linkinghub.elsevier.com/retrieve/pii/S0168583X12000961>

Alton, G., (1993). Ion sources for accelerators in materials research. *Nuclear Instruments and Methods in Physics Research Section B: Beam Interactions with Materials and Atoms* 73, 221–288.

<http://linkinghub.elsevier.com/retrieve/pii/0168583X9395738Q>

Arnold, M., Merchel, S., Bourlès, D. L., Braucher, R., Benedetti, L., Finkel, R. C., Aumaître, G., Gottdang, A., Klein, M., (2010). The French accelerator mass spectrometry facility ASTER: Improved performance and developments. *Nuclear Instruments and Methods in Physics Research Section B: Beam Interactions with Materials and Atoms* 268, 1954–1959.

<http://linkinghub.elsevier.com/retrieve/pii/S0168583X10002028>

Baba, T., Funaya, N., Miyazaki, N., Takahashi, T., Kaikura, T., Seki, R., Sueno, S., Jiang, S., Nagashima, Y., (1997). Detection of ^{41}Ca with a $^7\text{Li}^{37}\text{Cl}$ molecular pilot beam. *Nuclear Instruments and Methods in Physics Research Section B: Beam Interactions with Materials and Atoms* 123, 183–185.

<http://linkinghub.elsevier.com/retrieve/pii/S0168583X96007847>

Bennett, C. L., Beukens, R. P., Clover, M. R., Gove, H. E., Liebert, R. B., Litherland, A. E., Purser, K. H., Sondheim, W. E., (1977). Radiocarbon Dating Using Electrostatic Accelerators: Negative Ions Provide the Key. *Science* 198, 508–510.

<http://www.sciencemag.org/cgi/doi/10.1126/science.198.4316.508>

Bergqvist, I., Drake, D., McDaniels, D., (1974). Radiative capture of fast neutrons by ^{40}Ca . *Nuclear Physics A* 231, 29–44.

<http://linkinghub.elsevier.com/retrieve/pii/0375947474902917>

- BMJV, (n.d.)**. Verordnung über den Schutz vor Schäden durch ionisierende Strahlen.
https://www.gesetze-im-internet.de/strlSchv_2001/BJNR171410001.html
- Chamizo, E., Enamorado, S. M., García-León, M., Suter, M., Wacker, L., (2008)a**. Plutonium measurements on the 1 MV AMS system at the Centro Nacional de Aceleradores (CNA). *Nuclear Instruments and Methods in Physics Research Section B: Beam Interactions with Materials and Atoms* 266, 4948–4954.
<http://linkinghub.elsevier.com/retrieve/pii/S0168583X08009506>
- Chamizo, E., López-Gutiérrez, J. M., Ruiz-Gómez, A., Santos, F., García-León, M., Maden, C., Alfimov, V., (2008)b**. Status of the compact 1 MV AMS facility at the Centro Nacional de Aceleradores (Spain). *Nuclear Instruments and Methods in Physics Research Section B: Beam Interactions with Materials and Atoms* 266, 2217–2220.
<http://linkinghub.elsevier.com/retrieve/pii/S0168583X08002218>
- Chamizo, E., (2009)**. *Medida de isótopos de plutonio, ^{239}Pu y ^{240}Pu , mediante espectrometría de masas con aceleradores de baja energía*. Ph.D. thesis, Universidad de Sevilla.
- Chamizo, E., Christl, M., Fifield, L., (2015)a**. Measurement of ^{236}U on the 1 MV AMS system at the Centro Nacional de Aceleradores (CNA). *Nuclear Instruments and Methods in Physics Research Section B: Beam Interactions with Materials and Atoms* 358, 45–51.
<http://linkinghub.elsevier.com/retrieve/pii/S0168583X15004796>
- Chamizo, E., López-Lora, M., Villa, M., Casacuberta, N., López-Gutiérrez, J. M., Pham, M. K., (2015)b**. Analysis of ^{236}U and plutonium isotopes, $^{239,240}\text{Pu}$, on the 1 MV AMS system at the Centro Nacional de Aceleradores, as a potential tool in oceanography. *Nuclear Instruments and Methods in Physics Research Section B: Beam Interactions with Materials and Atoms* 361, 535–540.
<http://linkinghub.elsevier.com/retrieve/pii/S0168583X15001913>
- Chamizo, E., Santos, F. J., López-Gutiérrez, J. M., Padilla, S., García-León, M., Heine-meier, J., Schnabel, C., Scognamiglio, G., (2015)c**. Status report of the 1 MV AMS facility at the Centro Nacional de Aceleradores. *Nuclear Instruments and Methods in Physics Research Section B: Beam Interactions with Materials and Atoms* 361, 13–19.
<http://linkinghub.elsevier.com/retrieve/pii/S0168583X15001391>
- Chamizo, E., López-Lora, M., Bressac, M., Levy, I., Pham, M., (2016)**. Excess of ^{236}U in the northwest Mediterranean Sea. *Science of The Total Environment* 565, 767–776.
<http://linkinghub.elsevier.com/retrieve/pii/S0048969716308452>
- Chamizo, E., López-Lora, M., (in press)**. Accelerator mass spectrometry of ^{236}U with He stripping at the Centro Nacional de Aceleradores. *Nuclear Instruments and Methods in*

Physics Research Section B: Beam Interactions with Materials and Atoms.

<http://linkinghub.elsevier.com/retrieve/pii/S0168583X18302659>

Christl, M., Vockenhuber, C., Kubik, P. W., Wacker, L., Lachner, J., Alfimov, V., Synal, H.-A., (2013). The ETH Zurich AMS facilities: Performance parameters and reference materials. *Nuclear Instruments and Methods in Physics Research Section B: Beam Interactions with Materials and Atoms* 294, 29–38.

<http://linkinghub.elsevier.com/retrieve/pii/S0168583X12001577>

Cranston, F., White, D., (1971). Thermal neutron capture cross sections in calcium. *Nuclear Physics A* 169, 95–100.

<http://linkinghub.elsevier.com/retrieve/pii/0375947471905628>

CSN, (2003). INSTRUCCIÓN IS/05, de 26 de febrero de 2003, del Consejo de Seguridad Nuclear, por la que se definen los valores de exención para nucleidos según se establece en las tablas A y B del anexo I del Real Decreto 1836/1999. *Boletín Oficial del Estado* 86, 14221–14229.

<https://www.boe.es/buscar/doc.php?id=BOE-A-2003-7520>

CSN, (n.d.). General information - José Cabrera.

<https://www.csn.es/en/central-nuclear/jose-cabrera>

Denk, E., Hillegonds, D. J., Vogel, J., Synal, A., Geppert, C., Wendt, K., Fattinger, K., Hennesy, C., Berglund, M., Hurrell, R. F., Walczyk, T., (2006). Labeling the human skeleton with ⁴¹Ca to assess changes in bone calcium metabolism. *Analytical and Bioanalytical Chemistry* 386, 1587–1602.

<http://link.springer.com/10.1007/s00216-006-0795-5>

Denk, E., Hillegonds, D. J., Hurrell, R. F., Vogel, J., Fattinger, K., Häuselmann, H. J., Kraenzlin, M., Walczyk, T., (2007). Evaluation of ⁴¹Calcium as a New Approach to Assess Changes in Bone Metabolism: Effect of a Bisphosphonate Intervention in Postmenopausal Women With Low Bone Mass. *Journal of Bone and Mineral Research* 22, 1518–1525.

<http://doi.wiley.com/10.1359/jbmr.070617>

Dillmann, I., Domingo-Pardo, C., Heil, M., Käppeler, F., Wallner, A., Forstner, O., Golser, R., Kutschera, W., Priller, A., Steier, P., Mengoni, A., Gallino, R., Paul, M., Vockenhuber, C., (2009). Determination of the stellar (n,γ) cross section of ⁴⁰Ca with accelerator mass spectrometry. *Physical Review C* 79, 065805.

<https://link.aps.org/doi/10.1103/PhysRevC.79.065805>

Döbeli, M., Kottler, C., Stocker, M., Weinmann, S., Synal, H.-A., Grajcar, M., Suter, M., (2004). Gas ionization chambers with silicon nitride windows for the detection and identification of low energy ions. *Nuclear Instruments and Methods in Physics Research Section B: Beam Interactions with Materials and Atoms* 219-220, 415–419.

<http://linkinghub.elsevier.com/retrieve/pii/S0168583X04001211>

Dunai, T. J., (2010). Cosmogenic nuclides : principles, concepts and applications in the earth surface sciences. Cambridge University Press.

Elmore, D., Phillips, F. M., (1987). Accelerator Mass Spectrometry for Measurement of Long-Lived Radioisotopes. *Science* 236, 543–550.

<http://www.sciencemag.org/cgi/doi/10.1126/science.236.4801.543>

Elmore, D., Bhattacharyya, M. H., Sacco-Gibson, N., Peterson, D. P., (1990). Calcium-41 as a long-term biological tracer for bone resorption. *Nuclear Instruments and Methods in Physics Research Section B: Beam Interactions with Materials and Atoms* 52, 531–535.

<http://linkinghub.elsevier.com/retrieve/pii/0168583X90904716>

ENRESA, (n.d.). Dismantling of the Jose Cabrera Nuclear Power Plant.

<http://www.enresa.es/eng/index/activities-and-projects/dismantling-and-environmental-restoration/dismantling-of-the-jose-cabrera-nuclear-power-plant>

Field, K., Remec, I., Pape, Y. L., (2015). Radiation effects in concrete for nuclear power plants – Part I: Quantification of radiation exposure and radiation effects. *Nuclear Engineering and Design* 282, 126–143.

<http://linkinghub.elsevier.com/retrieve/pii/S0029549314005603>

Fifield, L. K., (2008). Accelerator mass spectrometry of the actinides. *Quaternary Geochronology* 3, 276–290.

<http://linkinghub.elsevier.com/retrieve/pii/S1871101407000581>

Fifield, L., Tims, S., Fujioka, T., Hoo, W., Everett, S., (2010). Accelerator mass spectrometry with the 14UD accelerator at the Australian National University. *Nuclear Instruments and Methods in Physics Research Section B: Beam Interactions with Materials and Atoms* 268, 858–862.

<http://linkinghub.elsevier.com/retrieve/pii/S0168583X09010982>

Fink, D., Paul, M., Hollos, G., Theis, S., Vogt, S., Stueck, R., Englert, P., Michel, R., (1987). Measurements of ^{41}Ca spallation cross sections and ^{41}Ca concentrations in the grant meteorite by accelerator mass spectrometry. *Nuclear Instruments and Methods in Physics*

Research Section B: Beam Interactions with Materials and Atoms 29, 275–280.

<http://linkinghub.elsevier.com/retrieve/pii/0168583X87902497>

Fink, D., Middleton, R., Klein, J., Sharma, P., (1990). ^{41}Ca : Measurement by accelerator mass spectrometry and applications. *Nuclear Instruments and Methods in Physics Research Section B: Beam Interactions with Materials and Atoms* 47, 79–96.

<http://linkinghub.elsevier.com/retrieve/pii/0168583X9090049Z>

Fink, D., Klein, J., Middleton, R., Vogt, S., Herzog, G. F., (1991). ^{41}Ca in iron falls, Grant and Estherville: production rates and related exposure age calculations. *Earth and Planetary Science Letters* 107, 115–128.

<http://linkinghub.elsevier.com/retrieve/pii/0012821X9190048M>

Freeman, S., Serfass, R., King, J., Southon, J., Fang, Y., Woodhouse, L., Bench, G., McAninch, J., (1995). Biological sample preparation and ^{41}Ca AMS measurement at LLNL. *Nuclear Instruments and Methods in Physics Research Section B: Beam Interactions with Materials and Atoms* 99, 557–561.

<http://linkinghub.elsevier.com/retrieve/pii/0168583X95003428>

Freeman, S. P., King, J. C., Vieira, N. E., Woodhouse, L. R., Yergey, A. L., (1997). Human calcium metabolism including bone resorption measured with ^{41}Ca tracer. *Nuclear Instruments and Methods in Physics Research Section B: Beam Interactions with Materials and Atoms* 123, 266–270.

<http://linkinghub.elsevier.com/retrieve/pii/S0168583X9600701X>

Gómez-Guzmán, J. M., (2010). *Medida de ^{129}I en el sistema de Espectrometría de Masas con Aceleradores de 1 MV del Centro Nacional de Aceleradores. Aplicación a problemas medioambientales.* Ph.D. thesis, Universidad de Sevilla.

Gómez-Guzmán, J. M., López-Gutiérrez, J. M., Pinto-Gómez, A., Holm, E., (2012). ^{129}I measurements on the 1 MV AMS facility at the Centro Nacional de Aceleradores (CNA, Spain). *Applied Radiation and Isotopes* 70, 263–268.

<http://linkinghub.elsevier.com/retrieve/pii/S0969804311004040>

Gómez-Guzmán, J. M., Bishop, S., Faestermann, T., Famulok, N., Fimiani, L., Hain, K., Jahn, S., Korschinek, G., Ludwig, P., Rodrigues, D., (2015). Accretion rate of extraterrestrial ^{41}Ca in Antarctic snow samples. *Nuclear Instruments and Methods in Physics Research Section B: Beam Interactions with Materials and Atoms* 361, 620–626.

<http://linkinghub.elsevier.com/retrieve/pii/S0168583X15004875>

Gove, H. E., Fulton, B. R., Elmore, D., Litherland, A. E., Beukens, R. P., Purser, K. H., Naylor, H., (1979). Radioisotope Detection with Tandem Electrostatic Accelerators. *IEEE*

Transactions on Nuclear Science 26, 1414–1419.

<http://ieeexplore.ieee.org/document/4330402/>

Hampe, D., Gleisberg, B., Akhmadaliev, S., Rugel, G., Merchel, S., (2013). Determination of ^{41}Ca with LSC and AMS: method development, modifications and applications. *Journal of Radioanalytical and Nuclear Chemistry* 296, 617–624.

<http://link.springer.com/10.1007/s10967-012-2145-8>

Heinemeier, J., Olsen, J., Klein, M., Mous, D., (2015). The new extended HVE 1 MV multi-element AMS system for low background installed at the Aarhus AMS Dating Centre. *Nuclear Instruments and Methods in Physics Research Section B: Beam Interactions with Materials and Atoms* 361, 143–148.

<http://linkinghub.elsevier.com/retrieve/pii/S0168583X15005340>

Hennessy, C., Berglund, M., Ostermann, M., Walczyk, T., Synal, H.-A., Geppert, C., Wendt, K., Taylor, P. D., (2005). Certification of a ^{41}Ca dose material for use in human studies (IRMM-3703) and a corresponding set of isotope reference materials for ^{41}Ca measurements (IRMM-3701). *Nuclear Instruments and Methods in Physics Research Section B: Beam Interactions with Materials and Atoms* 229, 281–292.

<http://linkinghub.elsevier.com/retrieve/pii/S0168583X04012510>

Herzog, G. F., Caffee, M. W., Faestermann, T., Hertenberger, R., Korschinek, G., Leya, I., Reedy, R. C., Sisterson, J. M., (2011). Cross sections from 5 to 35 MeV for the reactions $^{\text{nat}}\text{Mg}(^3\text{He},x)^{26}\text{Al}$, $^{27}\text{Al}(^3\text{He},x)^{26}\text{Al}$, $^{\text{nat}}\text{Ca}(^3\text{He},x)^{41}\text{Ca}$, and $^{\text{nat}}\text{Ca}(^3\text{He},x)^{36}\text{Cl}$: Implications for early irradiation in the solar system. *Meteoritics and Planetary Science* 46, 1427–1446.

<http://onlinelibrary.wiley.com/doi/10.1111/j.1945-5100.2011.01236.x/full>

Hosoya, S., Sasa, K., Matsunaka, T., Takahashi, T., Matsumura, M., Matsumura, H., Sundquist, M., Stodola, M., Sueki, K., (2017). Optimization of a ΔE -E detector for ^{41}Ca AMS. *Nuclear Instruments and Methods in Physics Research Section B: Beam Interactions with Materials and Atoms* 406, 268–271.

<http://linkinghub.elsevier.com/retrieve/pii/S0168583X17305554>

Hou, X., (2005). Radiochemical determination of ^{41}Ca in nuclear reactor concrete. *Radiochimica Acta* 93, 611–617.

<http://www.degruyter.com/view/j/ract.2005.93.issue-9-10/ract.2005.93.9-10.611/ract.2005.93.9-10.611.xml>

Hou, X., Roos, P., (2008). Critical comparison of radiometric and mass spectrometric methods for the determination of radionuclides in environmental, biological and nuclear waste

- samples. *Analytica Chimica Acta* 608, 105–139.
<http://linkinghub.elsevier.com/retrieve/pii/S0003267007019964>
- IAEA, (2012).** Regulations for the Safe Transport of Radioactive Material. *IAEA Safety Standards SSR-6*.
http://www-pub.iaea.org/MTCD/publications/PDF/Pub1570_web.pdf
- IAEA, (n.d.).** NGAtlas.
<http://www-nds.iaea.org/ngatlas2/>
- ICRP, (2012).** ICRP Publication 119: Compendium of Dose Coefficients Based on ICRP Publication 60. *Annals of the ICRP* 41.
<http://journals.sagepub.com/doi/10.1016/j.icrp.2013.05.003>
- Jackson, G. S., Hillegonds, D. J., Muzikar, P., Goehring, B., (2013).** Ultra-trace analysis of ^{41}Ca in urine by accelerator mass spectrometry: An inter-laboratory comparison. *Nuclear Instruments and Methods in Physics Research Section B: Beam Interactions with Materials and Atoms* 313, 14–20.
<http://linkinghub.elsevier.com/retrieve/pii/S0168583X13008082>
- Jacob, S., Suter, M., Synal, H.-A., (2000).** Ion beam interaction with stripper gas – Key for AMS at sub MeV. *Nuclear Instruments and Methods in Physics Research Section B: Beam Interactions with Materials and Atoms* 172, 235–241.
<http://linkinghub.elsevier.com/retrieve/pii/S0168583X00002056>
- Jacob, S. A. W., (2001).** *Beschleunigermassenspektrometrie (AMS) von ^{14}C bei tiefen Energien*. Ph.D. thesis, ETH Zurich.
- Jörg, G., Amelin, Y., Kossert, K., Lierse v. Gostomski, C., (2012).** Precise and direct determination of the half-life of ^{41}Ca . *Geochimica et Cosmochimica Acta* 88, 51–65.
<http://linkinghub.elsevier.com/retrieve/pii/S0016703712001883>
- Klein, M., Mous, D., Gottdang, A., (2006).** A compact 1 MV multi-element AMS system. *Nuclear Instruments and Methods in Physics Research Section B: Beam Interactions with Materials and Atoms* 249, 764–767.
<http://linkinghub.elsevier.com/retrieve/pii/S0168583X06003806>
- Klein, M., van Staveren, H., Mous, D., Gottdang, A., (2007).** Performance of the compact HVE 1 MV multi-element AMS system. *Nuclear Instruments and Methods in Physics Research Section B: Beam Interactions with Materials and Atoms* 259, 184–187.
<http://linkinghub.elsevier.com/retrieve/pii/S0168583X0700225X>

- Klein, M., Vaes, W., Fabriek, B., Sandman, H., Mous, D., Gottdang, A., (2013).** The 1 MV multi-element AMS system for biomedical applications at the Netherlands Organization for Applied Scientific Research (TNO). *Nuclear Instruments and Methods in Physics Research Section B: Beam Interactions with Materials and Atoms* 294, 14–17.
<http://linkinghub.elsevier.com/retrieve/pii/S0168583X12004168>
- Korschinek, G., Bergmaier, A., Faestermann, T., Gerstmann, U., Knie, K., Rugel, G., Wallner, A., Dillmann, I., Dollinger, G., von Gostomski, C. L., Kossert, K., Maiti, M., Poutivtsev, M., Remmert, A., (2010).** A new value for the half-life of ^{10}Be by Heavy-Ion Elastic Recoil Detection and liquid scintillation counting. *Nuclear Instruments and Methods in Physics Research Section B: Beam Interactions with Materials and Atoms* 268, 187–191.
<http://linkinghub.elsevier.com/retrieve/pii/S0168583X09009872>
- Kubik, P. W., Elmore, D., Conard, N. J., Nishiizumi, K., Arnold, J. R., (1986).** Determination of cosmogenic ^{41}Ca in a meteorite with tandem accelerator mass spectrometry. *Nature* 319, 568–570.
<http://www.nature.com/doi/10.1038/319568a0>
- Kubik, P. W., Elmore, D., (1989).** AMS of ^{41}Ca Using the CaF_3 Negative Ion. *Radiocarbon* 31, 324–326.
https://www.cambridge.org/core/product/identifier/S0033822200011863/type/journal_article
- Lachner, J., Christl, M., Alfimov, V., Hajdas, I., Kubik, P. W., Schulze-König, T., Wacker, L., Synal, H.-A., (2014).** ^{41}Ca , ^{14}C and ^{10}Be concentrations in coral sand from the Bikini atoll. *Journal of Environmental Radioactivity* 129, 68–72.
<http://linkinghub.elsevier.com/retrieve/pii/S0265931X13002889>
- Larson, J., (1974).** New developments in beam transport through tandem accelerators. *Nuclear Instruments and Methods* 122, 53–63.
<http://linkinghub.elsevier.com/retrieve/pii/0029554X74904716>
- Lee, H., Galindo-Uribarri, A., Chang, K., Kilius, L., Litherland, A., (1984).** The $^{12}\text{CH}_2^{2+}$ molecule and radiocarbon dating by accelerator mass spectrometry. *Nuclear Instruments and Methods in Physics Research Section B: Beam Interactions with Materials and Atoms* 5, 208–210.
<http://linkinghub.elsevier.com/retrieve/pii/0168583X84905111>
- Lewis, E. E., (2008).** Fundamentals of Nuclear Reactor Physics. Elsevier.
- Longworth, B. E., Robinson, L. F., Roberts, M. L., Beaupre, S. R., Burke, A., Jenkins, W. J., (2013).** Carbonate as sputter target material for rapid ^{14}C AMS. *Nuclear Instruments and*

Methods in Physics Research Section B: Beam Interactions with Materials and Atoms 294, 328–334.

<http://linkinghub.elsevier.com/retrieve/pii/S0168583X12002819>

López-Gutiérrez, J. M., Gómez-Guzmán, J. M., Chamizo, E., Peruchena, J., García-León, M., (2013). Long-lived radionuclides in residues from operation and decommissioning of nuclear power plants. *Nuclear Instruments and Methods in Physics Research Section B: Beam Interactions with Materials and Atoms* 294, 647–651.

<http://linkinghub.elsevier.com/retrieve/pii/S0168583X12005538>

López-Lora, M., Chamizo, E., Villa-Alfageme, M., Hurtado-Bermúdez, S., Casacuberta, N., García-León, M., (2018). Isolation of ^{236}U and $^{239,240}\text{Pu}$ from seawater samples and its determination by Accelerator Mass Spectrometry. *Talanta* 178, 202–210.

<http://linkinghub.elsevier.com/retrieve/pii/S0039914017309712>

Maxeiner, S., (2016). *Optimizing the designs of next-generation AMS systems*. Ph.D. thesis, ETH Zurich.

Megahid, R., Makarious, A., El-Kolaly, M., (1981). Attenuation of reactor thermal neutrons in a bulk shield of ordinary concrete. *Annals of Nuclear Energy* 8, 79–85.

<http://linkinghub.elsevier.com/retrieve/pii/0306454981900311>

Middleton, R., (1990). *A Negative-Ion Cookbook*. Department Of Physics, University of Pennsylvania.

Miller, J. J., Hui, S. K., Jackson, G. S., Clark, S. P., Einstein, J. A., Weaver, C. M., Bhat-tacharyya, M. H., (2013). Calcium isolation from large-volume human urine samples for ^{41}Ca analysis by accelerator mass spectrometry. *Applied Radiation and Isotopes* 78, 57–61.

<http://linkinghub.elsevier.com/retrieve/pii/S0969804313001978>

Miltenberger, K.-U., Müller, A. M., Suter, M., Synal, H.-A., Vockenhuber, C., (2017). Accelerator mass spectrometry of ^{26}Al at 6 MV using AlO^- ions and a gas-filled magnet. *Nuclear Instruments and Methods in Physics Research Section B: Beam Interactions with Materials and Atoms* 406, 272–277.

<http://linkinghub.elsevier.com/retrieve/pii/S0168583X17301246>

Müller, A. M., (2009). *Entwicklung von universellen AMS Anlagen bei tiefen Energien*. Ph.D. thesis, ETH Zurich.

Müller, A., Christl, M., Lachner, J., Suter, M., Synal, H.-A., (2010). Competitive ^{10}Be measurements below 1 MeV with the upgraded ETH–TANDY AMS facility. *Nuclear Instruments and Methods in Physics Research Section B: Beam Interactions with Materials and Atoms*

268, 2801–2807.

<http://linkinghub.elsevier.com/retrieve/pii/S0168583X10005732>

Müller, A., Döbeli, M., Suter, M., Synal, H.-A., (2012). Performance of the ETH gas ionization chamber at low energy. *Nuclear Instruments and Methods in Physics Research Section B: Beam Interactions with Materials and Atoms* 287, 94–102.

<http://linkinghub.elsevier.com/retrieve/pii/S0168583X12003795>

Müller, A. M., Christl, M., Lachner, J., Synal, H.-A., Vockenhuber, C., Zanella, C., (2015). ^{26}Al measurements below 500 kV in charge state 2+. *Nuclear Instruments and Methods in Physics Research Section B: Beam Interactions with Materials and Atoms* 361, 257–262.

<http://linkinghub.elsevier.com/retrieve/pii/S0168583X1500419X>

National Nuclear Data Center, (n.d.). NuDat 2.

<http://www.nndc.bnl.gov/nudat2/>

Nishiizumi, K., Fink, D., Klein, J., Middleton, R., Masarik, J., Reedy, R. C., Arnold, J., (1997). Depth profile of ^{41}Ca in an Apollo 15 drill core and the low-energy neutron flux in the Moon. *Earth and Planetary Science Letters* 148, 545–552.

<http://linkinghub.elsevier.com/retrieve/pii/S0012821X97000514>

Padilla, S., (2015). *Medidas de ^{10}Be y ^{26}Al en Espectrometría de Masas con Acelerador de Baja Energía en el Centro Nacional de Aceleradores.* Ph.D. thesis, Universidad de Sevilla.

Raisbeck, G. M., Yiou, F., (1979). Possible use of ^{41}Ca for radioactive dating. *Nature* 277, 42–44.

<http://www.nature.com/doi/10.1038/277042a0>

Rugel, G., Pavetich, S., Akhmadaliev, S., Enamorado Baez, S. M., Scharf, A., Ziegenrucker, R., Merchel, S., (2016). The first four years of the AMS-facility DREAMS: Status and developments for more accurate radionuclide data. *Nuclear Instruments and Methods in Physics Research Section B: Beam Interactions with Materials and Atoms* 370, 94–100.

<http://linkinghub.elsevier.com/retrieve/pii/S0168583X16000604>

Rühm, W., Kato, K., Korschinek, G., Morinaga, H., Nolte, E., (1992). ^{36}Cl and ^{41}Ca depth profiles in a Hiroshima granite stone and the Dosimetry System 1986. *Zeitschrift für Physik A Hadrons and Nuclei* 341, 235–238.

<http://link.springer.com/10.1007/BF01298486>

Ruiz-Gómez, A., Chamizo, E., López-Gutiérrez, J. M., García-León, M., Müller, A., Christl, M., (2010). On the measurement of ^{10}Be on the 1 MV compact AMS system at the Centro

Nacional de Aceleradores (Spain). *Nuclear Instruments and Methods in Physics Research Section B: Beam Interactions with Materials and Atoms* 268, 733–735.

<http://linkinghub.elsevier.com/retrieve/pii/S0168583X09010660>

Schiwietz, G., Grande, P., (2001). Improved charge-state formulas. *Nuclear Instruments and Methods in Physics Research Section B: Beam Interactions with Materials and Atoms* 175-177, 125–131.

<http://linkinghub.elsevier.com/retrieve/pii/S0168583X00005838>

Schulze-König, T., Maden, C., Denk, E., Freeman, S., Stocker, M., Suter, M., Synal, H.-A., Walczyk, T., (2010). Comparison of ^{41}Ca analysis on 0.5 MV and 5 MV AMS systems. *Nuclear Instruments and Methods in Physics Research Section B: Beam Interactions with Materials and Atoms* 268, 752–755.

<http://linkinghub.elsevier.com/retrieve/pii/S0168583X09010714>

Scognamiglio, G., Chamizo, E., López-Gutiérrez, J. M., Müller, A., Padilla, S., Santos, F., López-Lora, M., Vivo-Vilches, C., García-León, M., (2016). Recent developments of the 1 MV AMS facility at the Centro Nacional de Aceleradores. *Nuclear Instruments and Methods in Physics Research Section B: Beam Interactions with Materials and Atoms* 375, 17–25.

<http://linkinghub.elsevier.com/retrieve/pii/S0168583X16300088>

Scognamiglio, G., (2017). *Optimization of ^{10}Be and ^{26}Al detection with low-energy accelerator mass spectrometry.* Ph.D. thesis, Universidad de Sevilla.

Sharma, P., Middleton, R., (1987). Sample preparation and production of negative ions of calcium hydride for ^{41}Ca AMS. *Nuclear Instruments and Methods in Physics Research Section B: Beam Interactions with Materials and Atoms* 29, 63–66.

<http://linkinghub.elsevier.com/retrieve/pii/S0168583X87902059>

Sims, G., Juhnke, D., (1969). The thermal neutron capture cross section and resonance capture integral of ^{35}Cl for (n, γ) and (n,p) reactions. *Journal of Inorganic and Nuclear Chemistry* 31, 3721–3725.

<http://linkinghub.elsevier.com/retrieve/pii/0022190269802885>

SIS, (n.d.). SIMION®.

<http://simion.com/>

Srinivasan, G., Ulyanov, A. A., Goswami, J. N., (1994). Ca-41 in the early solar system. *The Astrophysical Journal* 431, L67.

<http://adsabs.harvard.edu/doi/10.1086/187474>

- Steinhof, A., Behr, K., Brünle, A., Roeckl, E., Boaretto, E., Paul, M., Fink, D., Hollos, G., Kutschera, W., (1989).** Electromagnetic isotope enrichment for accelerator mass spectrometry of ^{41}Ca . *Nuclear Instruments and Methods in Physics Research Section B: Beam Interactions with Materials and Atoms* 43, 73–81.
<http://linkinghub.elsevier.com/retrieve/pii/0168583X89900827>
- Stocker, M., Bertschinger, R., Döbeli, M., Grajcar, M., Jacob, S., Scheer, J., Suter, M., Synal, H.-A., (2004).** Status of the PSI/ETH compact AMS facility. *Nuclear Instruments and Methods in Physics Research Section B: Beam Interactions with Materials and Atoms* 223-224, 104–108.
<http://linkinghub.elsevier.com/retrieve/pii/S0168583X04005403>
- Stocker, M., Döbeli, M., Grajcar, M., Suter, M., Synal, H.-A., Wacker, L., (2005).** A universal and competitive compact AMS facility. *Nuclear Instruments and Methods in Physics Research Section B: Beam Interactions with Materials and Atoms* 240, 483–489.
<http://linkinghub.elsevier.com/retrieve/pii/S0168583X05011213>
- Stocker, M. G., (2006).** *AMS bei tiefen Energien*. Ph.D. thesis, ETH-Zurich.
- Sun, G., Döbeli, M., Müller, A., Stocker, M., Suter, M., Wacker, L., (2007).** Energy loss and straggling of heavy ions in silicon nitride in the low MeV energy range. *Nuclear Instruments and Methods in Physics Research Section B: Beam Interactions with Materials and Atoms* 256, 586–590.
<http://linkinghub.elsevier.com/retrieve/pii/S0168583X07001681>
- Suter, M., (1990).** Accelerator mass spectrometry: State of the art in 1990. *Nuclear Instruments and Methods in Physics Research Section B: Beam Interactions with Materials and Atoms* 52, 211–223.
<http://linkinghub.elsevier.com/retrieve/pii/0168583X9090409N>
- Suter, M., Jacob, S., Synal, H., (1997).** AMS of ^{14}C at low energies. *Nuclear Instruments and Methods in Physics Research Section B: Beam Interactions with Materials and Atoms* 123, 148–152.
<http://linkinghub.elsevier.com/retrieve/pii/S0168583X96006131>
- Suter, M., (1998).** A new generation of small facilities for accelerator mass spectrometry. *Nuclear Instruments and Methods in Physics Research Section B: Beam Interactions with Materials and Atoms* 139, 150–157.
<http://linkinghub.elsevier.com/retrieve/pii/S0168583X97009452>
- Synal, H.-A., Jacob, S., Suter, M., (2000).** The PSI/ETH small radiocarbon dating system. *Nuclear Instruments and Methods in Physics Research Section B: Beam Interactions with*

Materials and Atoms 172, 1–7.

<http://linkinghub.elsevier.com/retrieve/pii/S0168583X00003761>

Synal, H.-A., Stocker, M., Suter, M., (2007). MICADAS: A new compact radiocarbon AMS system. *Nuclear Instruments and Methods in Physics Research Section B: Beam Interactions with Materials and Atoms* 259, 7–13.

<http://linkinghub.elsevier.com/retrieve/pii/S0168583X07001942>

Vivo-Vilches, C., López-Gutiérrez, J. M., García-León, M., Vockenhuber, C., Walczyk, T., (2017). ^{41}Ca measurements on the 1 MV AMS facility at the Centro Nacional de Aceleradores (CNA, Spain). *Nuclear Instruments and Methods in Physics Research Section B: Beam Interactions with Materials and Atoms* 413, 13–18.

<http://linkinghub.elsevier.com/retrieve/pii/S0168583X17309047>

Vivo-Vilches, C., López-Gutiérrez, J. M., Perriñez, R., Marcinko, C., Le Moigne, F., McGinny, P., Peruchena, J. I., Villa-Alfageme, M., (2018). Recent evolution of ^{129}I levels in the Nordic Seas and the North Atlantic Ocean. *Science of The Total Environment* 621, 376–386.

<http://linkinghub.elsevier.com/retrieve/pii/S0048969717333260>

Vivo-Vilches, C., López-Gutiérrez, J. M., García-León, M., Vockenhuber, C., (in press). Factors related to ^{41}K interference on ^{41}Ca AMS measurements. *Nuclear Instruments and Methods in Physics Research Section B: Beam Interactions with Materials and Atoms*.

<http://linkinghub.elsevier.com/retrieve/pii/S0168583X18302763>

Vockenhuber, C., Golser, R., Kutschera, W., Priller, A., Steier, P., Vorderwinkler, K., Wallner, A., (2005). The ΔTOF detector for isobar separation at ion energies below 1 MeV/amu. *Nuclear Instruments and Methods in Physics Research Section B: Beam Interactions with Materials and Atoms* 240, 490–494.

<http://linkinghub.elsevier.com/retrieve/pii/S0168583X05011225>

Vockenhuber, C., Alfimov, V., Christl, M., Lachner, J., Schulze-König, T., Suter, M., Synal, H.-A., (2013). The potential of He stripping in heavy ion AMS. *Nuclear Instruments and Methods in Physics Research Section B: Beam Interactions with Materials and Atoms* 294, 382–386.

<http://linkinghub.elsevier.com/retrieve/pii/S0168583X12000298>

Vockenhuber, C., Schulze-König, T., Synal, H.-A., Aeberli, I., Zimmermann, M., (2015). Efficient ^{41}Ca measurements for biomedical applications. *Nuclear Instruments and Methods in Physics Research Section B: Beam Interactions with Materials and Atoms* 361, 273–276.

<http://linkinghub.elsevier.com/retrieve/pii/S0168583X15004851>

Wallner, A., Forstner, O., Golser, R., Korschinek, G., Kutschera, W., Priller, A., Steier, P., Vockenhuber, C., (2010). Fluorides or hydrides? ^{41}Ca performance at VERA's 3 MV AMS facility. *Nuclear Instruments and Methods in Physics Research Section B: Beam Interactions with Materials and Atoms* 268, 799–803.

<http://linkinghub.elsevier.com/retrieve/pii/S0168583X09010830>

Warwick, P. E., Croudace, I. W., Hillegonds, D. J., (2009). Effective Determination of the Long-lived Nuclide ^{41}Ca in Nuclear Reactor Bioshield Concretes: Comparison of Liquid Scintillation Counting and Accelerator Mass Spectrometry. *Analytical Chemistry* 81, 1901–1906.

<http://pubs.acs.org/doi/abs/10.1021/ac802225a>

Weaver, C. M., Martin, B. R., Jackson, G. S., McCabe, G. P., Nolan, J. R., McCabe, L. D., Barnes, S., Reinwald, S., Boris, M. E., Peacock, M., (2009). Antiresorptive Effects of Phytoestrogen Supplements Compared with Estradiol or Risedronate in Postmenopausal Women Using ^{41}Ca Methodology. *The Journal of Clinical Endocrinology & Metabolism* 94, 3798–3805.

<https://academic.oup.com/jcem/article-lookup/doi/10.1210/jc.2009-0332>

Weaver, C. M., Martin, B. R., Jackson, G. S., McCabe, G. P., Peacock, M., Wastney, M., (2017). Calcium-41: a technology for monitoring changes in bone mineral. *Osteoporosis International* 28, 1215–1223.

<http://link.springer.com/10.1007/s00198-016-3849-3>

Weick, H., (n.d.). GICOSY.

<https://web-docs.gsi.de/~weick/gicosy/>

Welten, K., Hillegonds, D., Masarik, J., Nishiizumi, K., (2007). Cosmogenic ^{41}Ca in diogenites: Production rates, pre-atmospheric size and terrestrial ages. *Nuclear Instruments and Methods in Physics Research Section B: Beam Interactions with Materials and Atoms* 259, 653–662.

<http://linkinghub.elsevier.com/retrieve/pii/S0168583X07003114>

Winkler, S. R., Steier, P., Buchriegler, J., Lachner, J., Pitters, J., Priller, A., Golser, R., (2015). He stripping for AMS of ^{236}U and other actinides using a 3 MV tandem accelerator. *Nuclear Instruments and Methods in Physics Research Section B: Beam Interactions with Materials and Atoms* 361, 458–464.

<http://linkinghub.elsevier.com/retrieve/pii/S0168583X15003754>

- Wittkower, A. B., Betz, H. D., (1973).** Equilibrium Charge-State Distributions of 2-15-MeV Tantalum and Uranium Ions Stripped in Gases and Solids. *Physical Review A* 7, 159–167.
<https://link.aps.org/doi/10.1103/PhysRevA.7.159>
- Wollnik, H., (1999).** Ion optics in mass spectrometers. *Journal of Mass Spectrometry* 34, 991–1006.
<http://doi.wiley.com/10.1002/%28SICI%291096-9888%28199910%2934%3A10%3C991%3A%3AAID-JMS870%3E3.0.CO%3B2-1>
- Zhao, X.-L., Eliades, J., Liu, Q., Kieser, W. E., Litherland, A. E., Ye, S., Cousins, L. M., (2010).** Studies of anions from sputtering III: The ^{41}K background in $^{41}\text{CaF}_3^-$ measurement by AMS. *Nuclear Instruments and Methods in Physics Research Section B: Beam Interactions with Materials and Atoms* 268, 816–819.
<http://linkinghub.elsevier.com/retrieve/pii/S0168583X09010878>
- Ziegler, J., (n.d.).** SRIM & TRIM.
<http://www.srim.org/>

BIBLIOGRAPHY

Curriculum Vitae

Name: Carlos Vivo-Vilches

Date of birth: 16th October 1989

Place of birth: Murcia, Spain

UNIVERSITY EDUCATION

since 2014 PhD on Physical Science and Technologies, Universidad de Sevilla. PhD thesis "⁴¹Ca measurement with Low Energy Accelerator Mass Spectrometry (LEAMS) at the Centro Nacional de Aceleradores" supervised by José María López-Gutiérrez (Universidad de Sevilla) and Christof Vockenhuber (ETH Zurich).

2013-2014 Master on Nuclear Physics, Universidad de Sevilla. Masther thesis "Estudio de una fuente de iones de superficie en el marco del proyecto TRAPSENSOR y primeros resultados de enfriamiento por láser (*laser cooling*) de iones de ⁴⁰Ca⁺" supervised by Daniel Rodríguez-Rubiales (Universidad de Granada).

2008-2013 Graduate on Physics (Spanish *Licenciatura*), Universidad de Granada

PROFESSIONAL EXPERIENCE

since September 2014 PhD Student, AMS group, Centro Nacional de Aceleradores

January 2014 - August 2014 Researcher, Departamento de Física Atómica, Molecular y Nuclear, Universidad de Granada

PUBLICATIONS AS FIRST AUTHOR

C. VIVO-VILCHES, J.M. LÓPEZ-GUTIÉRREZ, M. GARCÍA-LEÓN, C. VOCKENHUBER

Factors related to ^{41}K interference on ^{41}Ca AMS measurements

Nuclear Instruments and Methods in Physics Research Section B: Beam Interactions with Materials and Atoms, in press

doi: [10.1016/j.nimb.2018.04.031](https://doi.org/10.1016/j.nimb.2018.04.031)

C. VIVO-VILCHES, J.M. LÓPEZ-GUTIÉRREZ, R. PERIÁÑEZ, C. MARCINKO, F. LE MOIGNE E, P. MCGIN-
NITY, J.I. PERUCHENA, M. VILLA-ALFAGEME

Recent evolution of ^{129}I levels in the Nordic Seas and the North Atlantic Ocean

Science of the Total Environment 621 (2018) 376-386

doi: [10.1016/j.scitotenv.2017.11.268](https://doi.org/10.1016/j.scitotenv.2017.11.268)

C. VIVO-VILCHES, J.M. LÓPEZ-GUTIÉRREZ, M. GARCÍA-LEÓN, C. VOCKENHUBER, T. WALZCYK

^{41}Ca measurements on the 1 MV AMS facility at the Centro Nacional de Aceleradores (CNA, Spain)

Nuclear Instruments and Methods in Physics Research Section B: Beam Interactions with Materials and Atoms 413 (2017) 13-18

doi: [10.1016/j.nimb.2017.10.003](https://doi.org/10.1016/j.nimb.2017.10.003)

OTHER PUBLICATIONS

G. SCOGNAMIGLIO, E. CHAMIZO, J.M. LÓPEZ-GUTIÉRREZ, A.M. MÜLLER, S. PADILLA, F.J. SANTOS, M.
LÓPEZ-LORA, C. VIVO-VILCHES, M. GARCÍA-LEÓN

Recent developments of the 1 MV AMS facility at the Centro Nacional de Aceleradores

Nuclear Instruments and Methods in Physics Research Section B: Beam Interactions with Materials and Atoms 375 (2016) 17-25

doi: [10.1016/j.nimb.2016.03.033](https://doi.org/10.1016/j.nimb.2016.03.033)